Università degli Studi di Milano - Bicocca

SCUOLA DI SCIENZE MATEMATICHE, FISICHE E NATURALI
Physics and Astrophysics

Ph.D Thesis
XXXV Cycle

Design and optimisation of a variable momentum secondary beamline for the NP06/ENUBET project

Candidata:
Elisabetta Giulia **Parozzi**

matricola: **790149**

University Supervisor:
Prof. Francesco **Terranova**
CERN Supervisor:
Dr. Nikolaos **Charitonidis**

Coordinator:
Prof. Stefano **Ragazzi**

Sessione di Difesa Dottorato: 01/2023
Anno Accademico: 2021/2022

Abstract

The precision of the measurement of the cross-section of the electronic and muon neutrino is mainly limited by the knowledge of the initial flux. The current precision is on the order of $5-10\%$. The ENUBET (Enhanced NeUtrino Beam from kaon Tagging) project proposes a new facility capable of monitoring the neutrino beam produced by a secondary meson beam by tagging the corresponding lepton emitted in the same production decay. This type of study places several restrictions on the secondary beam, that essentially defines the energy spectrum of the neutrinos reaching the far detector. In this Ph.D. thesis work, we present the studies carried out for the design and optimization of a modular momentum beamline (Multi-Momentum Beamline) at the BE-EA-LE section of CERN. The proposed layout is optimized for the transport of K^+ and π^+ mesons with momentum centered around 8.5, 6 and 4 GeV/c. Using this beamline, it is possible to monitor the neutrino energy in the area of interest of experiments such as HyperK, T2K, and DUNE through the same configuration of magnets. In addition to modularity, the developed multi-momentum beamline presents remarkable properties such as a very satisfactory neutrino yield, control of the background, and satisfactory beam properties and performance that are all discussed in detail. A special target optimization procedure for maximizing the hadron yield has also been devised. Furthermore, the design is made up of only elements already in use at CERN. The use of pre-existing magnets allows a quantitative as well as qualitative analysis of the performance of the beamline as well as a low cost in the implementation. Finally, a comparison between Monte-Carlo and data for the ENUBINO prototype, tested at CERN's EAST area is presented.

Sommario

La precisione sulla misura della sezione d'urto del neutrino elettronico e muonico è limitata principalmente dalla conoscenza del flusso iniziale. La precisione attuale è dell'ordine del $5-10\%$. Il progetto ENUBET (Enhanced NeUtrino Beam from kaon Tagging) propone una nuova facility in grado di monitorare il fascio di neutrini prodotto da un fascio secondario di mesoni taggando il leptone corrispondente emesso nello stesso decadimento di produzione. Questo tipo di studio pone diverse restrizioni sul fascio secondario, dal quale dipende soprattutto la distribuzione in energia dei neutrini che raggiungono il detector. In questo lavoro di tesi di dottorato si presentano gli studi effettuati per il design e l'ottimizzazione di una beamline a energia modulare (Multi-Momentum Beamline) presso la sezione BE-EA-LE del CERN. Il layout proposto è ottimizzato per il trasporto di mesoni K^+ e π^+ con momento centrato in 8.5, 6 e 4 GeV/c. Attraverso questa tecnica è possibile monitorare l'energia di neutrini nell'area di interesse di esperimenti quali HyperK, T2K e DUNE tramite la stessa configurazione di magneti. Oltre alla modularità, la Multi-Momentum Beamline è caratterizzata da un angolo di produzione che permette un primo filtro dal fondo che raggiungerebbe il tunnel di decadimento. Inoltre, il design è composto da soli elementi già attualmente in uso al CERN. L'impiego di magneti pre-esistenti permette un'analisi quantitativa, oltre che qualitativa delle performance della beamline oltre a un costo contenuto nell'implementazione.

List of Figures

List of Tables

Contents

Motivation and Outline

The precision of the measurements of neutrino cross-sections at the GeV scale is mainly limited by the knowledge of the initial flux, which in turn is affected by the uncertainties on hadro-production and particle propagation along the beamline. This limitation leads to a precision of $\mathcal{O}(5-10\%)$. The ENUBET (Enhanced NeUtrino Beam from kaon Tagging) project aims to develop a facility that produces a beam of electron neutrinos originating from the decays of kaon mesons. The rate of the K_{e3} decay is tagged and monitored in the decay tunnel so to improve the precision of the flux and, hence, of cross-section measurements by an order of magnitude. Further information can be drawn from monitoring muons created by the two-body kaon decay. The electron neutrino flux is monitored by observing the large-angle positrons produced by the decays with a longitudinally segmented calorimeter instrumenting the decay tunnel (ENUBET technique) and a moderate-size (500 t) liquid argon detector located at a short distance from the source.

To obtain these results, the neutrino facility must transport kaons and pions to the decay tunnel with high efficiency and moderate contamination from halo and off-momentum particles.

The current beamline designed by ENUBET[1] is focused on a secondary beam of 8.5 GeV/c. Several optimization studies have been carried out to obtain a satisfactory secondary meson rate (K^+ and π^+) that reaches the decay tunnel. In the present Ph.D. thesis, an alternative beamline design that expands the meson momentum range (K, π) to include particles with momenta of 4, 6, and 8.5 GeV/c[2] is presented. To study topics such as CP violation in the lepton channel, the neutrino mass hierarchy problem, and more exotic topics, it is essential to have high precision in the measurement of the cross-section of electronic and muon neutrinos. Experiments focusing on these studies, however, operate at different energy ranges. While the baseline design would serve the DUNE region of interest[3], the multi-momentum beamline would expand its applications to experiments such as HyperK and T2K that operate at lower energies as well.

This work is organized as follows. The first introductory chapter provides

the reader with the physics context that motivates the ENUBET proposal. The concept of "monitored neutrino beam" – the class of experiments ENUBET belongs to – is introduced in chapter3, together with an overview of their experimental and technical challenges. To properly understand the parameters and quantities discussed later in this thesis, a chapter devoted to the theory of magnets and beamlines in general is provided to the reader. The core of the thesis - the proposal of the Multi Momentum Beamline - is detailed in chapters4,5, and 6. Chapter 4, discusses the production of secondary particles and the optimization of the target. Subsequently, the design of the optics and the implementation of the beamline is presented using Monte-Carlo techniques that are mandatory to optimize the beamline component and performance. This Ph.D. study also presents contributions to the development of the instrumentation of the decay tunnel and the identification of the technology that allows for lepton identification. Chapter6, in particular, summarizes the results of the ENUBINO prototype which was instrumental in the construction and validation of the ENUBET Demonstrator.

Chapter 1

Introduction

The neutrino is one of the most mysterious particles described by the Standard Model. It is a lepton without electric charge and a particularly small mass. Since neutrinos only interact by weak and gravitational forces, they represent a fundamental tool to investigate weak interactions.

1.1 Neutrinos in the Standard Model

The first step toward neutrino physics dates back to 1896 when A. H. Becquerel discovered the radioactivity of Uranium. This breakthrough led later to the study of α, β, and γ decays. In 1914, J. Chadwick demonstrated that the β-decay energy spectrum is continuous, unlike the α and γ decay spectra. Energy conservation considerations imply that this spectrum could not be originated by a two-body decay. It was later demonstrated that the missing energy could not be ascribed to neutral γ-rays, hence it could lead to the existence of a new particle.

Fermi developed an early neutrino theory where weak interactions were described by vector current as in QED. Despite Fermi's theory successfully explaining the β decay process, the neutrino had never been observed until the first fission reactors became available in the early 1950s. In 1947, B. Pontecorvo proposed the detection of neutrinos through the inverse β-decay:

$$\overline{\nu}_e + p \rightarrow e^+ + n \tag{1.1}$$

The detection principle was a measurement of the 511 keV photons associated with positron annihilation before a neutron capture reaction occurs a few μs later. Pontecorvo's idea urged F. Reines and C.L. Cowan to look for a way to observe the process. Eventually, they developed an experiment in which anti-neutrinos produced by the Savannah River nuclear reactor was detected

employing 10 ton of equipment consisting of a water tank enriched with a ^{108}Cd solution surrounded by two tanks of liquid scintillators [4]. This was the first neutrino-reactor experiment and resulted in the first experimental evidence of the neutrino's existence [5].
Once parity violation was discovered, weak interactions were interpreted in the framework of the V-A theory formulated by R. Marshak, G. Sudarshan, R. Feynman, and M. Gell-Mann. Then, L. Landau, T.D. Lee and C.N. Yang, and A. Salam proposed a two-component massless neutrino model to explain the weak couplings. In this theory, neutrinos are left-handed and anti-neutrinos are right-handed. Soon after, the helicity of the neutrino was measured by Goldhaber in the electron capture:

$$e^- + ^{152}Eu \rightarrow {}^{152}Sm* + \nu_e \quad \Rightarrow \quad {}^{152}Sm* \rightarrow {}^{152}Sm + \gamma \tag{1.2}$$

The measurement of the photon's polarization constrains the neutrino's polarization, in agreement with Landau, Lee, Yang, and Salam's theory. The dependence of neutrino interactions by helicity was the core assumption to incorporate neutrinos in the Standard Model (SM). At that time, neutrinos were considered massless particles, and, hence, left-handed helicity neutrinos were considered identical to left-handed chirality neutrinos.

In 1962, the Brookhaven neutrino experiment [6] – the first experiment which involved neutrinos produced at an accelerator – established that neutrinos taking part in charged-current interactions with electrons are different from neutrinos that interact with muons. This discovery provided a flavor number to neutrinos: another key information for the Standard Model description of electroweak forces[7].

In 1968, J. Bachall and R. Davis presented the pioneer experiment that provided the first evidence of flavor mixing. The Homestake experiment was the first experiment to measure the flux of neutrinos produced by nuclear fusion in the sun. The results showed a rate of ν_e of about one-third of what was predicted. The deficit was then referred to as the solar neutrino problem. It was the first hint of the neutrino oscillation phenomenon. A theory that explained the neutrino flavor oscillation had already been proposed by Maki, Nakagawa, and Sakata beforehand, however, it required the neutrino to be massive, as opposed to the description of neutrino particles in the Standard Model.

After Davis' experiment, other experiments provided similar results by measuring atmospheric neutrinos. The Kamiokande underground Cherenkov detector observed a deficit of ν_μ compared to the ν_e flux produced by the cosmic rays interacting in the Earth's atmosphere. In 1998, the SuperKamiokande (SK) Collaboration published a seminal result: muon neutrinos originating

from the upper atmosphere and traveling just a handful of km before reaching the detector were recorded with the expected flux. Conversely, neutrinos originating from the opposite side of the Earth, thus traveling thousands of km before reaching the detector, showed a major flux reduction. Later on, SK showed that the flux pattern was sinusoidal, as expected by the oscillation of muon neutrinos toward other flavors. This result, soon confirmed by accelerator neutrinos (K2K, MINOS, OPERA), demonstrated that neutrino oscillates according to the theory described in Sec. 1.4 and are massive particles.

The solar neutrino problem was finally solved in 2012 by the SNO experiment which measured the total solar neutrino flux and found it in agreement with the Standard Solar Model[8]. Moreover, the KamLAND experiment, at the Kamioka Observatory, observed the oscillatory pattern in the electron antineutrino energy distribution unambiguously establishing the neutrino oscillation phenomenon. The SM had to be modified to account for this discovery. The "minimally extended Standard Model" (which is nowadays simply called the Standard Model) describes neutrinos as massive particles. Helicity is thus different from chirality and only left-handed (right-handed) (anti)neutrinos can couple with the W-bosons and interact through charged currents. Neutral currents (i.e. coupling with the Z bosons) are also forbidden for right-handed neutrinos and left-handed antineutrinos, which are thus "sterile particles". In the minimally extended SM, sterile particles can exist because neutrinos and antineutrinos are different particles. Therefore a left-handed neutrino may exist but can couple to matter only through gravitational interactions. A different realization of the SM predicts neutrinos to be massive Majorana particles. In this case, neutrinos and antineutrinos are the same particles and the left-handed neutrino is identified with the right-handed antineutrino. To date, there is no evidence that neutrinos are Majorana particles and the search for Majorana neutrinos through e.g. neutrinoless double beta decay is an active field of research.

1.2 Neutrino interactions

Neutrino interactions are described by the Standard Model electro-weak theory and can occur via leptonic charged (CC) and neutral (NC) current:

$$CC: \quad j^{\rho}_{W,L} = \sum_{\alpha=e,\mu,\tau} \overline{\nu_\alpha}\gamma^{\rho}(1-\gamma^5)l_\alpha \tag{1.3}$$

$$NC: \quad j^{\rho}_{Z,\nu} = \frac{1}{2}\sum_{\alpha=e,\mu,\tau} \overline{\nu_\alpha}\gamma^{\rho}(1-\gamma^5)\nu_\alpha \tag{1.4}$$

Neutral current (NC) interactions can only be detected when the nucleus taking part in the interaction breaks apart, resulting in a final state different from the initial state, or if the nucleus scatters away when momentum is transferred from the neutrino to the nucleus. Moreover, NC interactions are flavor-independent.

$$\nu_l + N \rightarrow \nu_l + X \tag{1.5}$$

On the contrary, charged current (CC) interactions are easier to detect and the flavor of the emitted lepton provides knowledge about the flavor of the incoming neutrino. The simplest neutrino interaction is the electron-neutrino elastic scattering process. In first order, it only involves free leptons, whose interaction amplitude can be calculated exactly by using the Feynman rules.

$$\nu_\alpha + e^- \rightarrow \nu_\alpha + e^- \tag{1.6}$$

This process can be used in water Cherenkov solar neutrino detectors. While the elastic scattering process does not require any energy threshold, going up on the energy scale can initiate different interactions such as the quasi-elastic scattering process. As an example, muon neutrinos with energy above the μ production threshold interacting with electrons through charged current produce the *inverse muon decay*:

$$\nu_\mu + e^- \rightarrow \nu_e + \mu^- \tag{1.7}$$

At energies above $\sim$ 2 GeV, due to the high momentum transferred, neutrinos might serve as a probe to investigate the structure of composite particles. This kind of process is called *Deep Inelastic Scattering* (DIS)[9] and results in a final state composed by a hadronic shower and the corresponding charged lepton. As already mentioned, neutrinos mainly interact through weak forces, therefore the cross sections for all the aforementioned processes are very small (of the order of 10^{-38} cm^2 at the GeV scale) and are measured with large uncertainties. As shown in Figure 1.1, the cross-section of all the interaction processes depends in different ways on nuclear form factors or parton distribution functions. Nuclear physics in the non-perturbative QCD regime is a major obstacle to decoupling the weak interactions of neutrino from strong interactions of the scattering final state. The theoretical description of neutrino cross-section is thus plagued by large uncertainties due to electroweak nuclear physics. It is of utmost importance to increase the precision of the measurements to have a better understanding of neutrino interactions with matter and constrain the large uncertainties of cross-section models.

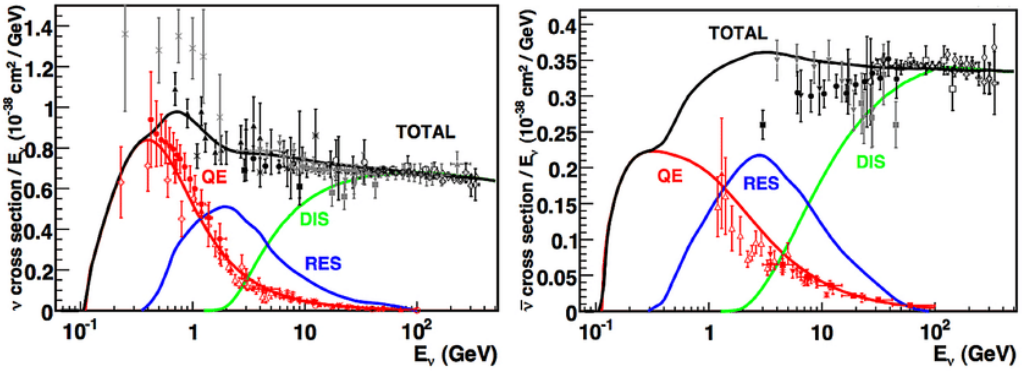

Figure 1.1: The neutrino-nucleon (left panel) and antineutrino-nucleon (right panel) cross sections divided by energy and plotted as a function of (anti)neutrino energy. The processes that contribute to the total cross section (shown by the black lines) are quasi-elastic (QE, red lines) scattering; resonance production (RES, blue lines); and deep inelastic scattering (DIS, green lines). The uncertainties in the energy range of interest are typically 10-40%. The data are shown from experiments and compared to theoretical predictions.[10]

1.3 Neutrino Masses in the Standard Model

As mentioned above, it is now known that the neutrino is massive due to the existence of the oscillation phenomenon. The neutrino masses are constrained by the following three physical quantities:

Cosmology: $$\sum = m_1 + m_2 + m_3 <\sim 1\,eV \tag{1.8}$$

Beta Decay: $$m_{\nu e} = \sqrt{\sum |U_{ei}|^2 m_i^2} < 0.23\,eV \tag{1.9}$$

Double Beta Decay: $$|m_{ee}| = \left|\sum U_{ei}^2 m_i\right| < 0.2 - 0.8\,eV \tag{1.10}$$

Mass measurements can be done by studying either the kinematics of weak decays using energy and momentum conservation or time of flight measurements assuming $E^2 = p^2c^2 + m_\nu^2 c^4$ and hypothesis on emission time distribution. Massive neutrinos are now discussed as interpreted by the minimally extended SM (Dirac neutrinos). The readers are referred to [11] for a detailed description of the SM Majorana realization. Since neutrinos are the only neutral fermions, a massive neutrino can be described by either Dirac's or Majorana's theory, as well as by the most general Dirac-Majorana case [11]. A massless fermion can be described by a chiral field, for example, by

Landau, Lee, and Yang's two-component theory of a massless neutrino. The generic Dirac equation is:

$$(i\gamma^{\mu}\partial_{\mu} - m)\psi = 0 \tag{1.11}$$

for a fermion field

$$\psi = \psi_L + \psi_R \tag{1.12}$$

which is equivalent to the equation:

$$i\gamma^{\mu}\partial_{\mu}\psi_L = m\psi_R \tag{1.13}$$
$$i\gamma^{\mu}\partial_{\mu}\psi_R = m\psi_L \tag{1.14}$$

the space-time evolution of the chiral field is coupled by the mass m. Therefore, if a fermion is supposed to be massless, the two equations are decoupled. Hence, a massless fermion can be described by a single chiral field. Since particles participate in weak interactions through the left-handed chiral component, it was first proposed that a massless neutrino could be simply described by a left-handed Weyl spinor ν_L.

However, neutrinos were found to be massive since 1998. A Dirac neutrino mass can be generated with the same Higgs mechanism that gives masses to quarks and charged leptons in the Standard Model. It is then necessary to extend the SM introducing a right-handed component $\nu_{\alpha R}$ per neutrino fields ($\alpha = e, \mu, \tau$). Right-handed neutrino fields are invariant under the symmetries of the SM: they are singlets of $\mathrm{SU}(3)_C \times \mathrm{SU}(2)_L$ and have hypercharge $\mathrm{Y} = 0$. These same neutrino fields are often called *sterile* because they only participate in gravitational interactions. In general, in the Standard Model (SM), the mass of fermions is the strength of their Yukawa coupling to the Higgs field, expressed by the SM Higgs-lepton Yukawa Lagrangian:

$$L_{Yukawa} = \sum_{\alpha,\beta=1}^{3} \overline{u}_L^{\alpha} m_{\alpha\beta} u_R^{\beta} + \overline{d}_L^{\alpha} m_{\alpha\beta} d_R^{\beta} + \overline{l}_L^{\alpha} m_{\alpha\beta} l_R^{\beta} \tag{1.15}$$

Here, α and β label the three generations, and l, u, and d denote the charged lepton and the two types of quark fields respectively. The L and R subscripts denote the left and right chirality of the fields. However, since the neutrino is massive and needs coupling to the Higgs field, it's necessary to extend the theory including the right-hand neutrino fields so that the neutrino can acquire its mass like the other fermions. This way, the Yukawa Lagrangian picks up an extra term:

$$L_{mass} = \overline{\nu}_L^{\alpha} m_{\alpha\beta} \nu_R^{\beta} + h.c. \tag{1.16}$$

ν denotes the neutrino field and α β are the lepton flavours. In order to obtain 3 physical masses of the neutrinos and link the flavour eigenstates to the mass eigenstates, the mass matrix, $m_{\alpha\beta}$, needs to be diagonal. This is done by choosing two unitary matrices $U_{R,L}$ such that:

$$m' = U_L^\dagger m U_R \tag{1.17}$$

or:

$$\nu_R'^i = U_R^{\beta i}\nu_R^\beta \tag{1.18}$$
$$\nu_L'^i = U_L^{\beta i}\nu_L^\beta \tag{1.19}$$

The primed fields are called mass eigenstates. Therefore, the mass eigenstates can be defined as flavor eigenstates super-impositions and are the ones that propagate through space and time, while the flavor ones undergo gauge interactions. The U matrix is also called the PMNS matrix (Pontecorvo-Maki-Nakagawa-Sakata).

1.4 Neutrino Oscillations

As previously mentioned, neutrino mass eigenstates ($k = 1, 2, 3$) are different from flavour eigenstates ($\alpha = e, \mu, \tau$) and are related by a unitary matrix U:

$$|\nu_\alpha\rangle = \sum_k U_{\alpha,k} * |\nu_k\rangle \tag{1.20}$$

The unitary matrix U is called the PMNS matrix (Pontecorvo, Maki, Nakagawa, and Sakata)[12]. Moreover, since mass eigenvalues are non-degenerate, neutrinos undergo a flavor oscillation phenomenon during propagation. The PMNS matrix for antineutrinos is identical to the matrix for neutrinos under CPT symmetry. In analogy to the Cabibbo-Kobayashi-Maskawa matrix (CKM) which describes the mixing of quark flavors, the PMNS matrix describes the mixing of lepton flavors. The complex matrix U has $2n^2$ independent parameters but the unitarity constraint reduces their number to n^2; $n(n-1)/2$ of which are angles and $n(n+1)/2$ are complex phases.

Supposing the neutrino is not a Majorana particle, $2n-1$ phases can be absorbed by rephasing the neutrino and charged lepton fields. This means that the actual number of physical phases is $(n-1)(n-2)/2$, i.e. one complex phase for $n = 3$. Otherwise, if the neutrinos are Majorana particles, there needs to be $n-1$ additional complex phases. However, the Majorana phases are irrelevant for oscillation physics, and therefore the PMNS matrix can

be described by just 4 parameters: three mixing angles $\theta_{12}, \theta_{13}, \theta_{23}$ and one complex phase δ:

$$U = \begin{pmatrix} 1 & 0 & 0 \\ 0 & c_{23} & s_{23} \\ 0 & -s_{23} & c_{23} \end{pmatrix} \begin{pmatrix} c_{13} & 0 & s_{13}e^{-i\delta} \\ 0 & 1 & 0 \\ s_{13}e^{i\delta} & 0 & c_{13} \end{pmatrix} \begin{pmatrix} c_{12} & s_{12} & 0 \\ -s_{12} & c_{12} & 0 \\ 0 & 0 & 1 \end{pmatrix} \tag{1.21}$$

$$= \begin{pmatrix} c_{12}c_{13} & s_{12}c_{13} & s_{13}e^{-\delta} \\ -s_{12}c_{23} - c_{12}s_{23}s_{13}e^{i\delta} & c_{12}c_{23} - s_{12}s_{23}s_{13}e^{i\delta} & s_{23}c_{13} \\ s_{12}s_{23} - c_{12}c_{23}s_{13}e^{i\delta} & -c_{12}s_{23} - s_{12}c_{23}s_{13}e^{i\delta} & c_{13}c_{23} \end{pmatrix} \tag{1.22}$$

where s_{ij} and c_{ij} is a shortening for sine and cosine of the θ_{ij} angles respectively.

1.4.1 Neutrino oscillation formalism

Flavor oscillation can be described in the Standard Model using the formalism of quantum field theory but a simplified description is provided by non-relativistic quantum mechanics assuming neutrino flavor wavepackets to be coherent superpositions of mass eigenstate wavepackets. The quantum mechanical derivation provides the following oscillation formula:

$$P(\nu_\alpha(t) \to \nu_\beta) = |\langle \nu_\beta | \nu_\alpha(t) \rangle|^2 \tag{1.23}$$

Once the squared mass difference $\Delta m^2_{kj} \equiv m^2_k - m^2_j$ is defined, it's possible to define the oscillation probability as a function of the distance (L) traveled by the neutrino wavepacket and its energy (E) as these are the physical observables useful for an experiment:

$$P(\nu_\alpha \to \nu_\beta)(L, E) = \sum_{k,j} U^*_{\alpha k} U_{\beta k} U_{\alpha j} U^*_{\beta j} exp\left(-i\frac{\Delta m^2_{jk} L}{2E}\right) \tag{1.24}$$

The transition for which $\alpha \neq \beta$ is called "appearance probability", while the transition for $\alpha = \beta$ is called "disappearance probability. Equation 1.24 shows that oscillations depend on the distance L between the source and the detector, the E energy of the neutrino, and the squared mass difference, whereas the amplitude of the oscillation depends on the mixing matrix U. Therefore, it is virtually impossible to observe charged lepton oscillations given the large mass-squared difference between leptons as compared to the ν masses. Equation 1.24 is equivalent to the SM oscillation formula for any process of interest in this thesis. If CP invariance holds:

$$P(\nu_\alpha \to \nu_\beta) = P(\bar{\nu}_\alpha \to \bar{\nu}_\beta) \tag{1.25}$$

but the occurrence of CP conservation in neutrinos is not established by experiment and the search for CP violation remains a prominent open issue. In general, by measuring CP asymmetries it could be possible to probe CP violation in neutrino oscillations and the mixing matrix. Such violation would vanish in the limit $\delta = 0$ or π. Like quarks, CP-violation in neutrinos is a three-family interference effect. Hence, if any of the mixing angles are either 0 or 90 degrees, CP cannot be observed irrespective of the value of δ.

Matter is made of electrons and no muons or tau leptons are present in ordinary atoms. As a consequence, all flavor-depended cross-sections change if neutrinos propagate in matter instead of vacuum. The treatment of propagation of neutrinos in the matter was pioneered by Wolfenstein in the 1960s and the Mikheyev–Smirnov–Wolfenstein (MSW) effect was instrumental to understand solar neutrinos in the sun. The experiments of interest in this thesis are experiments where L is relatively short ("short baseline experiments") and matter effects can be safely neglected. However, accelerator neutrino experiments where $L > 100$ km ("long-baseline") can detect matter effects. Assuming just two neutrino flavors, the corresponding formula is the same as in a vacuum provided that the squared-mass formula is replaced by an effective parameter:

$$\Delta\tilde{m}^2 = \Delta m^2 \sqrt{sin^2 2\theta + \left(cos2\theta \mp \frac{A}{\Delta m^2}\right)^2} \tag{1.26}$$

Where $A = 2\sqrt{2}G_F N_e E_\nu$, G_F is the Fermi constant and N_e is the electron density in matter (the earth's crust for long-baseline experiments). Similarly, the effective mixing angle is:

$$\tan 2\theta_M = \frac{\sin 2\theta}{\cos 2\theta \mp \frac{A}{\Delta m^2}} \tag{1.27}$$

where the $-$ $(+)$ sign holds for neutrinos (antineutrinos). Remarkably, neutrino oscillation in matter can be exploited to measure the sign of Δm^2 in the two-flavor approximation. This important result holds for three flavor oscillations, too, and will be discussed below.

1.5 Mass Hierarchy

Measurements of flavor transitions of neutrinos via the oscillations' mechanism have proved that at least two out of the three neutrinos described by the Standard Model must have non-zero masses. Throughout the previous

discussions, the ordering of the neutrino masses has never been questioned. As a matter of fact, there are two non-equivalent orderings for the neutrino masses, namely "Normal Ordering" (NO) and "Inverted Ordering" (IO) respectively with $m_1 < m_2 < m_3$ and $m_3 < m_1 < m_2$. The observation of the MSW effect in the Sun at the beginning of this century has shown that $\Delta m^2_{21} > 0$ and $\Delta m^2_{21} \ll |\Delta m^2_{31}| \simeq |\Delta m^2_{32}|$. Hence, the normal and inverted orders are defined by the sign of either Δm^2_{3l}, with $l = 1, 2$.

$$\Delta m^2_{31} > 0 \qquad \text{for NO} \tag{1.28}$$
$$\Delta m^2_{32} < 0 \qquad \text{for IO} \tag{1.29}$$

Long baseline experiments are the ideal tool to establish the mass neutrino

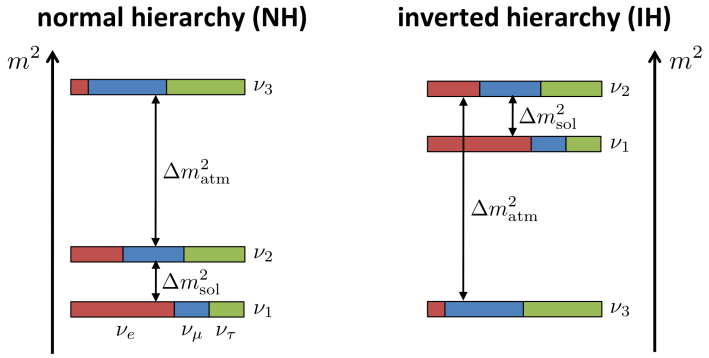

Figure 1.2: Scheme for Normal and Inverted Hierarchy with Δm^2_{atm} is Δm^2_{23} and Δm^2_{sol} is Δm^2_{12} [13]

ordering even if the sign of Δm^2_{31} can be measured also with high-precision reactor neutrino experiments or with atmospheric neutrinos.

Current data favors NO but the combination is plagued by tensions among different dataset. The current best fit under the assumption of NO is[14]:

$$\Delta m^2_{12} = 7.39^{+0.21}_{-0.20} \cdot 10^{-5}\,\text{eV}^2$$
$$\Delta m^2_{23} = 2.525^{+0.033}_{-0.032} \cdot 10^{-3}\,\text{eV}^2$$

1.6 Current status of neutrino oscillation measurements

Neutrino oscillations can be observed in solar, atmospheric, reactor, and accelerator neutrinos. Each neutrino oscillation experiment can be classified by

the ν flavor, energy E, and baseline length L (i.e. the distance between the neutrino source and the neutrino detector). Solar and atmospheric neutrinos form the main flux of neutrinos that crosses the Earth. The first ones consist of electron neutrinos that have mean energy of ~ 0.6 MeV, while atmospheric neutrinos are mainly muon neutrinos in the GeV range produced by hadronic showers due to collisions of cosmic rays with Earth's atmosphere. While the first ones travel a distance of $L \simeq 1.5 \times 10^8$ km, the latter ones reach the detectors after $L \simeq 10^4$ km. Apart from these natural sources, there also exist two sources of "artificial" neutrinos produced by nuclear power plant's reactors and by accelerators. Reactor neutrinos are electron antineutrinos obtained from β-decay and have an energy of a few MeV. Accelerator neutrinos – the core of this thesis – form specifically designed neutrino beams that can be tuned by changing the primary proton energy and secondary hadron momentum selection. An accelerator neutrino is usually of the order of a few GeV.

Source	**ν-type**	**E_ν[MeV]**	**L[km]**	**min(Δm^2)[eV^2]**
Reactor	$\overline{\nu_e}$	~ 1	1	$\sim 10^{-3}$
Reactor	$\overline{\nu_e}$	~ 1	100	$\sim 10^{-5}$
Accelerator	ν_μ, $\overline{\nu_\mu}$	$\sim 10^3$	1	~ 1
Accelerator	ν_μ, $\overline{\nu_\mu}$	$\sim 10^3$	100-1000	$\sim 10^{-3}$
Atmospheric	$\nu_{\mu,e}$, $\overline{\nu_{\mu,e}}$	$\sim 10^3$	10^4	$\sim 10^{-4}$
Solar	ν_e	~ 1	1.5×10^8	$\sim 10^{-11}$

Table 1.1: Summary of the main parameters for the different classes of neutrino experiments [14]

It's important to study different oscillation channels to get a full understanding of the general mixing parameters (the PMNS matrix). Neutrino experiments are hence classified based on the source of neutrinos employed and the oscillation effects observed, i.e. disappearance or appearance effects. The main focus is to study PMNS's parameters such as the mixing angles and the δ phase and the mass squared splittings. So far, solar neutrinos have been observed by chlorine (Homestake) and gallium (SAGE and GALLEX) radiochemical detectors, recording a 50% deficit of ν_e at 8σ, as well as by water Cherenkov detector using both light and heavy water (Kamiokande, Super-Kamiokande, and SNO), and at last by liquid scintillator detectors (Borexino and KamLAND). Almost all underground detectors can observe atmospheric neutrinos. The first experiments measuring ν_μ atmospheric neu-

Oscillation parameter	**Central value**	3σ **range**
Normal Ordering (best fit)		
$\Delta m^2_{21}/10^{-5}\text{eV}^2$	$7.39^{+0.21}_{-0.20}$	$6.79 \to 8.01$
$\Delta m^2_{31}/10^{-3}\text{eV}^2$	$+2.525^{+0.033}_{-0.031}$	$2.431 \to 2.622$
Solar mixing angle	$\sin^2\theta_{12} = 0.310^{+0.013}_{-0.012}$	$31.61° < \theta_{12} < 36.27°$
Atmospheric mixing angle	$\sin^2\theta_{23} = 0.582^{+0.015}_{-0.019}$	$40.9° < \theta_{23} < 52.2°$
CHOOZ mixing angle	$\sin^2\theta_{13} = 0.02240^{+0.00065}_{-0.00066}$	$8.22° < \theta_{13} < 8.98°$
Inverted Ordering ($\Delta\chi^2 = 9.3$)		
$\Delta m^2_{21}/10^{-5}\text{eV}^2$	$7.39^{+0.21}_{-0.20}$	$6.79 \to 8.01$
$\Delta m^2_{31}/10^{-3}\text{eV}^2$	$-2.512^{+0.034}_{-0.031}$	$-2.606 \to 2.413$
Solar mixing angle	$\sin^2\theta_{12} = 0.310^{+0.013}_{-0.012}$	$31.61° < \theta_{12} < 36.27°$
Atmospheric mixing angle	$\sin^2\theta_{23} = 0.582^{+0.015}_{-0.018}$	$41.2° < \theta_{23} < 52.1°$
CHOOZ mixing angle	$\sin^2\theta_{13} = 0.02263^{+0.00065}_{-0.00066}$	$8.27° < \theta_{13} < 9.03°$

Table 1.2: Neutrino oscillation parameters for both normal and inverted hierarchy.[15][16]

trinos transitions were the water Cherenkov for Kamiokande and IMB and iron tracking calorimeters for the Frejus experiment in France and the Soudan 2 experiment in the US. These experiment focused on the ν_μ/ν_e ratio, observing the $\nu_\mu \to \nu_\tau$ transition. Atmospheric neutrino oscillations have also been observed by the neutrino telescopes for high-energy neutrino astronomy by ANTARES and IceCube-DeepCore based on the ν_μ charged current events. The world leader in the field of atmospheric neutrinos is SuperKamiokande, which also observed the oscillation pattern as a function of the baseline and provides useful hints to determine the mass ordering.

The resulting fit for the PMNS parameters is shown in Tab 1.2 and the leading experiments are briefly described in the next section.

1.6.1 Oscillation experiments

Oscillation experiments have different sensitivity depending on their L/E (L = distance between production and detection, $E = \nu$ energy), detection and production modes. The L/E can be varied by selecting the baseline of the experiment depending on the parameters that it aims to be sensitive to. The most stringent constraint comes for the neutrino source, its energy, and its intensity. For example, KamLAND has an average baseline of 180 km and employs reactor neutrinos $E = \mathcal{O}(1)$ MeV, therefore it is more sensible to neutrino oscillations at the solar scale. On the other hand, experiments such

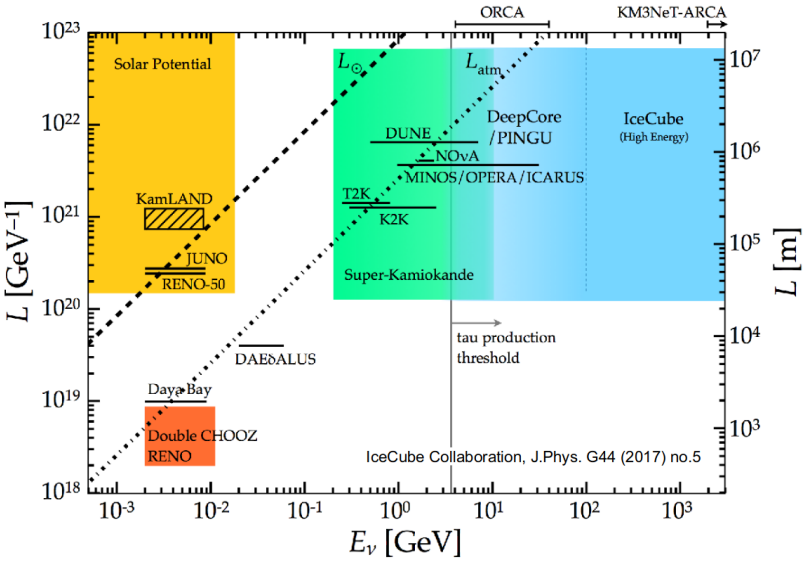

Figure 1.3: Present and proposed neutrino experiments as a function of L and E. [17]

as Double-Chooz, Daya Bay, and RENO employ the same type of neutrinos but with a baseline of a few hundred meters. They are thus bound to measure atmospheric oscillations parameters such as θ_{13} and Δm^2_{13}.

At the time of writing, θ_{13} is mostly driven by short baseline reactor experiments (Daya-Bay), while long-baseline accelerator neutrino beams determine Δm^2_{31} with high precision. θ_{23} is measured by the accelerator and atmospheric neutrinos. θ_{12} and Δm^2_{21} are determined by solar (SNO, SuperKamiokande) and reactor neutrino experiments (the aforementioned KamLAND experiment). No experiments but accelerator long-baseline experiments can measure δ, which is still under-constrained. Current experiments studying the oscillations phenomena and searching for a measurement of the δ phase include the Noνa experiment in the US and T2K in Japan. The next generation long-baseline experiments like Hyper-Kamiokande and DUNE [3] are aimed at discovering CP violation in neutrinos and improving significantly the measurement of the PMNS parameters. Due to the very long baseline (1300 km) DUNE will produce an unprecedented measurement of the sign of Δm^2_{13}, thus solving the mass ordering conundrum.

1.7 Neutrino cross-section measurements

The main goal of this thesis is to devise a novel facility for high-precision cross-section experiments. This requirement naturally follows from the consideration above. Long baseline experiments are the ideal tool to perform precision measurements of the PMNS matrix and discover the missing oscillation parameters. Their main observables of long-baseline experiments like DUNE or HyperKamiokande are the $\nu_\mu \to \nu_e$ transition probability and its CP conjugate $\bar{\nu}_\mu \to \bar{\nu}_e$. The ν_μ and $\bar{\nu}_\mu$ disappearance probabilities also play a pivotal role within this physics program. As a consequence, an exquisite knowledge of the ν_μ and ν_e cross section is key to the success of these experiments. At the time of writing, such knowledge is too poor and far from the needs of oscillation physics.

Neutrino interactions are described by the Standard Model and no deviations from it have been found in experimental data. Different experiments have focused their studies on different types of neutrino scatterings to fully understand neutrino cross-sections. Theoretically, the total cross-section is $\sigma \sim \frac{|M|^2}{s}$, where M is the scattering amplitude and s is the center of mass energy. M varies depending on the nature of the phenomenon. Therefore, it is important to study the different types of neutrino scattering results.

1.7.1 Neutrino-electron scattering

Neutrino-electron interactions are the simplest interactions of neutrinos with matter. At the lowest order in the weak interaction perturbation theory, the interactions involve free leptons, thus the amplitude can be calculated by using the Feynman rules. In general, for neutrino-electron scattering $M \sim G_F E_\nu m_e$, and if $E_\nu \ll m_e$, $s \sim m_e^2$ and $\sigma \sim G_F^2 E_\nu^2$.

Elastic scattering

At low energies, neutrinos with flavor $\alpha = e, \mu, \tau$ interact via elastic scattering with electrons:

$$\nu_\alpha + e^- \to \nu_\alpha + e^- \tag{1.30}$$

This process is widely used in water Cherenkov experiments like the aforementioned SuperKamiokande detector to record solar neutrinos. Since the final state is the same as the initial state, this process is thresholdless. What is observed is the redistribution of energy and momentum between the interacting particles, therefore the change in momentum of the electron. In the case of electron neutrinos, the contributions are both from the exchange of a W-boson and a Z-boson. Otherwise, in the case of either a muon or

a tau neutrino, there only are interactions due to neutral currents. Total cross-sections are proportional to the Fermi constant G_F^2, however since a cross-section has dimension (length)$^2 \sim$ (energy)$^{-2}$ and G_F^2 has dimension (energy)$^{-4}$, a factor with dimension (energy)^2 is needed. In the center of mass frame, the only factor with such dimension is the total squared energy $s = (E_{\nu i} + E_{ei})^2$, which is a relativistic invariant Mandelstam variable. Hence, it's necessary to determine s. The maximum recoil T_e of the electron depends on the neutrino energy E_ν:

$$T_e^{max} = \frac{2E_\nu^2}{m_e + 2E_\nu} \tag{1.31}$$

It follows that a minimum E_ν is required to produce a recoil T_e:

$$E_\nu^{min} \simeq \begin{cases} \sqrt{m_e T_e/2} & T_e \ll m_e \\ T_e + m_e/2 & T_e \gg m_e \end{cases} \tag{1.32}$$

Moreover, a detection threshold is mandatory to identify the scattering from the detector background and competing processes.

For example, Super-Kamiokande has a threshold of $T_e^{th} \simeq 4.5$ MeV. Thus, the total neutrino cross sections can be measured as a function of the neutrino energy E_ν. Measurements of the total cross section for the elastic-scattering process and different flavoured neutrinos are listed in the following table (1.3):

Process	**Total cross section (10^{-46} cm^2)**
$\nu_e + e^- \to \nu_e + e^-$	$\sigma \simeq 93\, s/\mathrm{MeV}^2$
$\overline{\nu_e} + e^- \to \overline{\nu_e} + e^-$	$\sigma \simeq 39\, s/\mathrm{MeV}^2$
$\nu_{\mu,\tau} + e^- \to \nu_{\mu,\tau} + e^-$	$\sigma \simeq 15\, s/\mathrm{MeV}^2$
$\overline{\nu_{\mu,\tau}} + e^- \to \overline{\nu_{\mu,\tau}} + e^-$	$\sigma \simeq 13\, s/\mathrm{MeV}^2$

Table 1.3: Total neutrino-electron cross-section for $\sqrt{s} \gg m_e$ [11]

1.7.2 Inclusive Scattering

The inclusive scattering consists of the interactions of neutrinos and antineutrinos with nucleons covering a broad range of energies.

$$\text{CC: } \nu_l + n \to l^- + p \qquad \overline{\nu_l} + p \to l^+ + n \tag{1.33}$$

$$\text{NC: } \nu_l + N \to \nu_l + N \qquad \overline{\nu_l} + N \to \overline{\nu_l} + N \tag{1.34}$$

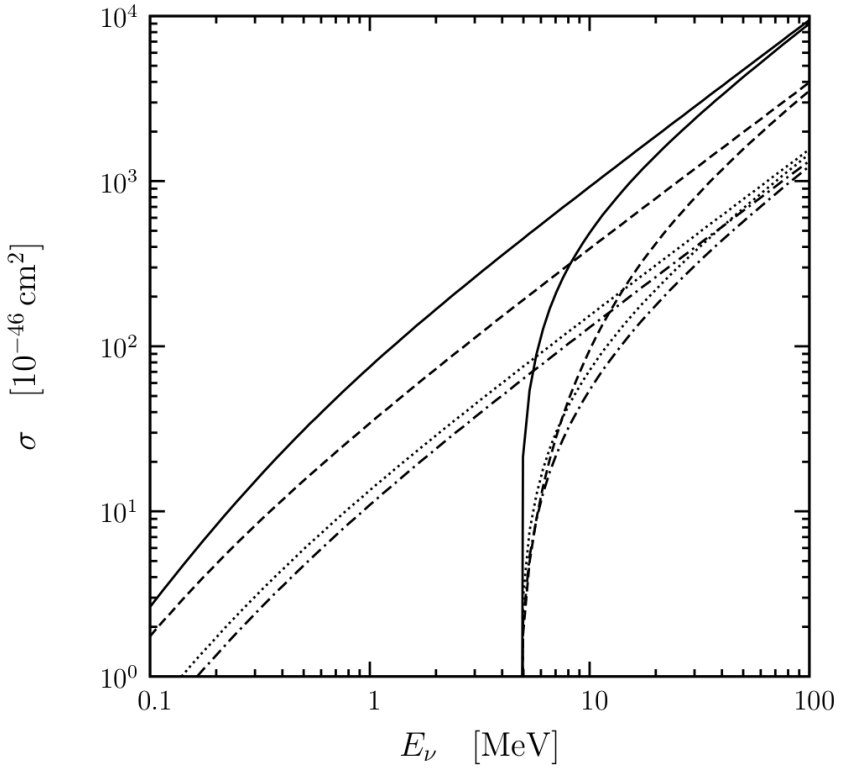

Figure 1.4: Neutrino cross section as a function of E_ν. Solid line: $\nu_e + e^- \to \nu_e + e^-$. Dotted line: $\nu_{\mu,\tau} + e^- \to \nu_{\mu,\tau} + e^-$. Dashed line: $\overline{\nu_e} + e^- \to \overline{\nu_e} + e^-$. Dash-dotted line: $\overline{\nu_{\mu,\tau}} + e^- \to \overline{\nu_{\mu,\tau}} + e^-$. [11]

The process for $l = e$ in Eq. 1.34 is sometimes called *inverse neutron decay* and it has been used in the historical experiment by Reines and Cowan in which neutrinos have been observed for the first time. The amplitude M for neutrino-nucleon scattering is $M \sim G_F E_\nu m_p$. The NC process has been used mainly for the measurement of the weak mixing angle, which links the nucleon weak and electromagnetic form factors in the cross-section expressions. For $E_\nu \sim$ GeV, in the case of a baryonic resonance excitation, the production of pions is possible. This process is called resonant scattering:

$$\begin{aligned} \text{CC:} \quad & \nu_l + N \to l^- + N' + \pi \\ \text{NC:} \quad & \nu_l + n/p \to \nu_l + n/p + \pi \end{aligned}$$

Once the energy of the neutrino rises ($E_\nu \gg$GeV), the scattering processes are dominated by deep inelastic scattering (DIS) processes, thus parton model corrections are necessary to predict the cross-section. DIS results in a lepton

and a hadronic shower:

$$\begin{array}{lll} \text{CC:} & \nu_l + n/p \to l^- + X & \overline{\nu_l} + n/p \to l^+ + X \\ \text{NC:} & \nu_l + n/p \to \nu_l + X & \overline{\nu_l} + n/p \to \overline{\nu_l} + X \end{array}$$

experiment	**beam**	**target**
ArgoNeuT	ν_μ, $\overline{\nu_\mu}$	Ar
MINERνA	ν_μ, $\overline{\nu_\mu}$	CH, C/CH, Fe/ch, Pb/CH
MINOS	ν_μ, $\overline{\nu_\mu}$	Fe
NOMAD	ν_μ	C
SciBooNE	ν_μ	CH
T2K	ν_μ, ν_e	CH, H_2O, Fe

Table 1.4: Summary of published measurements of neutrino CC inclusive cross sections from accelerator-based neutrino experiments [18]

Neutrinos can either interact via neutral and charged current but the latter is easier to detect given the outgoing lepton.

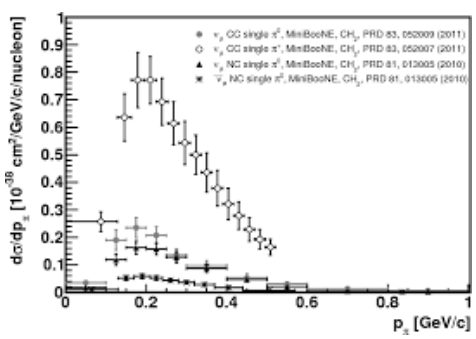

Figure 1.5: Differential cross section for CC and NC pion production from MINIBOONE experiment at a mean neutrino energy of 0.8 GeV, as a function of the momentum of the outgoing pion in the interaction.

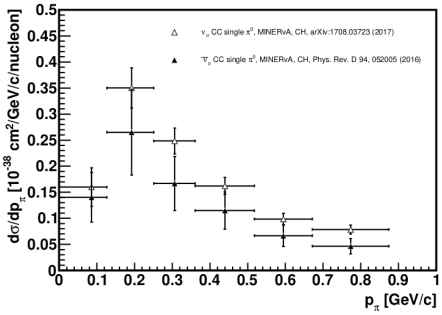

Figure 1.6: Differential cross section for neutrino and antineutrino CC π^0 production from MINERνA at a mean neutrino energy of 3.3 GeV. Shown here are the measurements as a function of the momentum of the outgoing pion in the interaction.

The knowledge of inclusive, exclusive, and multi-differential cross sections is thus plagued by:

- intranuclear corrections that account for the bounding of the quark inside a nucleon. This is mostly handled using the parton model

- internuclear corrections that account for the bounding of the nucleon inside the nucleus. This is currently the main source of theoretical uncertainty in model development since it cannot be dealt with by non-perturbative QCD and relies on nuclear and semi-empirical models

In the region of interest for long-baseline oscillation physics, theory predictions strongly depend on the target nucleus, low-Z experimental data are scarce, and discrepancies among models exceed 50% in most critical observables. As seen below, the predictive power is still at 100% level and large discrepancies with experiments have been reported by many analysis[19].

1.7.3 Neutrino cross-section experiments

The precision of the measurements of neutrino cross sections is mainly limited by the knowledge of the initial flux, which is affected by the uncertainties on hadro-production and particle propagation along the beam line. This limitation leads to a precision of $O(5-10\%)$ [20][21]. Here is a list of the most important neutrino cross-section experiments. All of them benefit from a detector located close to the neutrino source to maximize the flux and employ different target materials to study nuclei at different Z.

- The **MINERνA** experiment studies the neutrino and antineutrino cross-sections produced at the Fermilab Main Injector neutrino beam (NuMI) [22]. A fine-grained scintillator detector is employed to measure ν interactions on different targets: He, C, H_2O, Fe, Pb exploiting high statistics samples. The error on the cross-section is dominated by the flux systematics and the limited knowledge of the neutrino energy, which is inferred by the kinematics of final state particles. The NuMU flux is controlled at a 5% level. In 2022, **MINERνA** achieved the world record precision on ν_μ and $\bar{\nu}_\mu$ fluxes (3.3 and 4.7%, respectively).

- The **T2K** experiment, is a long-baseline neutrino experiment in Japan [23]. T2K searched oscillations from muon neutrinos to electron neutrinos and announced the first experimental indications for them in June 2011. The T2K experiment sends an intense beam of muon neutrinos from Tokai (JAERI) to Kamioka and, therefore, exploits the SuperKamiokande detector as a far detector. The neutrino beam is made in collisions between a proton beam and a graphite target; these

collisions produce pions, which quickly decay into muons and muon neutrinos. The muons and any remaining protons and pions are stopped by the second layer of graphite (beam dump) located after the drift region where pions decay. The T2K neutrino beam has a range of energies centered at 600 MeV since muon neutrinos with this energy are most likely to oscillate after traveling the JAERI-to-Kamioka distance (295 km). Due to the off-axis location of SuperKamiokande to the neutrino beam axis, the neutrino beam visible at the detector is somehow narrower compared with an on-axis detector. Flux predictions rely on a detailed simulation of the beamline. Hadron production constraint comes from a dedicated hadro-production experiment carried out at CERN (NA61/SHINE). The error on the flux is dominated by hadron interaction modeling but alignment/focusing uncertainties are also important. Cross sections are measured by the T2K near the detector, located 280 m from the target (ND280). The detector does not employ the same detector technology as Superkamiokande but cross-sections are measured on low-Z nuclei and water. T2K has measured the electron neutrino cross-section with a precision of about 20% and the flux uncertainty contributes to $> 10\%$ of the systematic budget. The inclusive ν_μ cross sections are measured at 10% level. Thanks to the power of the T2K beam, many results are available on differential ν_μ cross sections and exclusive processes. No measurements are available for $\bar{\nu}_e$.

- The **NOνA** experiment is a long-baseline experiment with a longer L than T2K. It thus studies neutrino oscillation in a region where matter effects are sizable. as T2K, it is composed of a near and far detector. The neutrino beam is produced by the aforementioned NuMI facility [24]. T. The near detector is located approximately 14.6 mrad off the axis of the beam, with a ν_e flux covering a broad range of energies. Both near and far detectors employ liquid scintillators as a target. Flux predictions were drawn by the full simulation of NuMI and a dedicated campaign of hadroproduction measurement with a graphite target identical to the target employed by NuMI. The near detector thus performs cross-section measurements with similar precision as ND280 at T2K. The energy range and target nuclei are, however, quite different.

- **MicroBooNE** is a liquid Argon TCP (LArTPC) located at the Fermilab Booster Beam. Due to the outstanding granularity of the liquid Argon detector, it has lower particle thresholds and excellent particle identification [25]. The main physics goals are to investigate the MiniBooNE low-energy excess and neutrino-argon cross-sections. Mi-

croboone is not equipped with a near detector yet. In the framework of the SBN program, the Microboone beam will serve as a near detector (SBND) of moderate mass and, since 2021, a large mass detector (ICARUS, 600 ton) located at a larger distance.

At the time of writing, new results are expected from the Run II of T2K, SBND, and ICARUS. Here, improvements are expected mostly on exclusive processes, model tuning, and nuclear effects in liquid argon. An important step forward will be accomplished with the near detectors of DUNE and HyperK starting in 2028. In a few years of data taking, most cross-section measurements accessible in these near detectors - including ν_e - will be systematically limited at the 10% level.

Present and future long-baseline experiments rely on the appearance of the ν_e for the study of CP violation and the determination of the mass ordering. Hence, a direct measurement of the ν_e cross-section that does not rely on lepton universality and, therefore, is not affected by nuclear and phase-space systematics is of great practical value. The first measurement at the GeV scale of the inclusive ν_e cross section was performed by the Gargamelle experiment, a bubble chamber that operated in the 1970s. This experiment collected thousands of events, 200 of which were selected and gave the first result of a neutrino cross-section [26]. As mentioned above, the best measurement at about 1 GeV was performed by the T2K experiments and reached a 20% level precision [27]. Data at higher energies are available from MINERνA and NuMIh in the 1-10 GeV range[28]. The current status of the ν_e cross-section measurements and the expected precision of the facility proposed in this thesis (ENUBET) is depicted in Fig.2.1.

Chapter 2

Monitored Neutrino Beams

The aim of neutrino physics for the next decades is to measure the small perturbations of the leading oscillation probabilities that encode effects due to CP violation, mass hierarchy, and the sterile neutrino. These challenges cannot be tackled without detailed knowledge of neutrino interaction cross-sections. The main limiting factor for a precise measurement of neutrino cross-sections is due to systematic uncertainties in the assessment of the initial flux, which is not performed in a direct manner but through a complete simulation of the production beam-line, leading to a precision on the flux prediction of the order of $5\% - 10\%$. Novel experimental approaches have been proposed to produce pure, intense, and well-controlled sources of electron neutrinos to address the problems posed by the limited knowledge of the electron neutrino cross-section. Neutrino Factories and Beta Beams facilities are under study to achieve a $\mathcal{O}(1\%)$ precision on absolute cross-sections. The precision of the measurements of the neutrino accelerator experiments is currently constrained by knowledge of the initial fluxes which are affected by significant uncertainties mainly due to uncertainties on the energy and angular distributions of the hadrons produced in proton-nucleus interactions in the neutrino beam target.

The ENUBET (Enhanced NeUtrino BEam from kaon Tagging) project aims to develop a facility that produces a monitored beam of electron and muon neutrinos originating from the decays of kaons and pions. The electron neutrino production rate through the K_{e3} ($K^+ \to \pi^0 e^+ \nu_e$) decay is tagged and monitored in the decay tunnel so to improve the knowledge of the initial electron neutrino flux and hence the precision of cross-section measurements by an order of magnitude.

The precision with which the decay of K_{e3} is known allows a precise estimate of the production rate of kaons at a percent level. It is also possible to monitor the production of $\pi^{\pm}$ inside the tunnel to improve this estimate.

This monitoring depends on the main decay modes of the K meson, $K^+ \to \mu^+ \nu_\mu$ with a branching ratio of 63% and $K^+ \to \pi^0 \pi^+$ with a branching ratio of 21%. By adding the study of these decay channels to the ENUBET scope, it is possible to evaluate the flux of ν_μ from kaons. Furthermore, the muon rate can be directly measured at the single event level from the decay of pions after the hadron dump, providing a flux precision of ν_μ comparable to that of ν_e. This is particularly relevant because, in any accelerator neutrino beam, ν_μ's from pion decays represent the dominant component of the beam.

The designed neutrino beam is a conventional narrow-band beam with a short ($\sim$ 20 m) transfer line followed by a 40 m long decay tunnel. Particles produced by the interaction of protons on the target are focused, momentum selected, and transported at the entrance of the decay tunnel. Such a facility requires the three-body semi-leptonic decay of kaons (K_{e3}) to be the only source of electron neutrinos. This requirement is fulfilled by optimizing the decay tunnel's length and the mean energy of the selected hadrons. The electron neutrino flux is monitored by observing the large-angle positrons produced by the decays with a longitudinally segmented calorimeter instrumenting the decay tunnel. Muons from kaon and pion decays are identified either by the aforementioned instrumentation or - when produced in the forward region - by an instrumented hadron dump.
This technique requires first of all the design and construction of a detector capable of identifying positrons originating from K_{e3} decays at a single particle level. The ENUBET project has been approved by the European Research Council (ERC Consolidator, PI A. Longhin, Host Institution INFN, Grant Agreement 681647) for a five-year duration and a 2.0 M€ budget to assess the performance with K_{e3}. In 2019, this project has been extended to investigate monitoring of ν_μ in the region of interest of DUNE and HyperK, and framed within the CERN Neutrino Platform (NP06/ENUBET). The project started on 1 June 2016 and the ENUBET Collaboration and the NP06/ENUBET experiment gather today 65 physicists from institutions in Italy, France, Russia Croatia, Greece, and Switzerland.

2.1 Conventional Neutrino beams

Conventional neutrino beams such as the one in Fig.2.2 are produced by the decay of secondary beams from charged mesons (π, K) produced by protons impinging on a light target, such as Be, graphite, or Al. A system of magnets allows the sign selection and focus of the meson beam with the energy spectrum of interest before entering the decay tunnel. Once the selected π

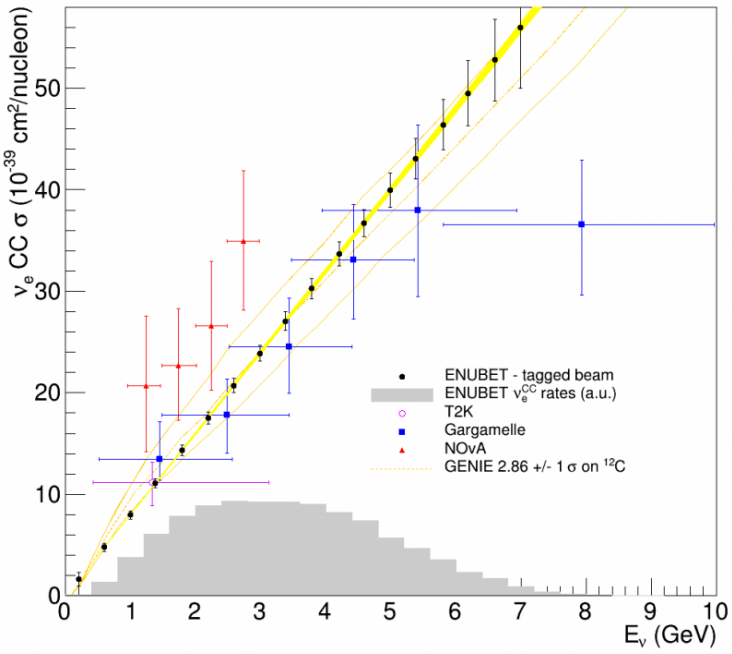

Figure 2.1: Current status of the electron neutrino cross section measurements (Gargamelle, NOνA, T2K), theory expectations (GENIE) and projected measurements from ENUBET in one year of data taking with PROTODUNE-SP [29]

and K particles traverse the decay tunnel, they decay-producing neutrinos.

$$M^+ \to \mu^+ + \nu_\mu \qquad (M \equiv \pi, K)$$

$$BR(\pi^+ \to \mu^+ + \nu_\mu) \simeq 1 \qquad BR(K^+ \to \mu^+ + \nu_\mu) = 0.635$$

It follows that the main sources of hadron contamination are given by both the K-meson and muon decays.

$$K^+ \to \pi^0 + e^+ + \nu_e \qquad\qquad \mu^+ \to e^+ + \nu_e$$

In order to reduce the yield of these decays in the decay tunnel, it is mandatory to optimize the length of the tunnel and work with shielding to stop the muons before decaying. The length of the decay tunnel varies with the meson momentum. The probability of an unstable particle decaying before

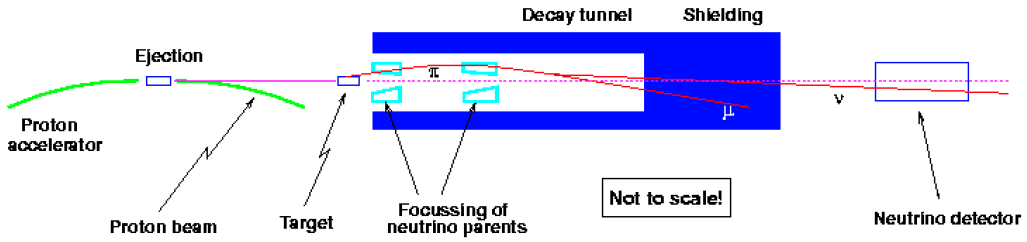

Figure 2.2: Schematic neutrino beam line

reaching the end of the tunnel is $P = 1 - e^{-L_{tunnel}/L_0}$, where:

$$L_0 = \beta c \gamma \tau_M = \frac{p_M}{m_M} \tau_M = \begin{cases} 55.9\text{m}\frac{p_\pi}{\text{GeV}} \\ 7.51\text{m}\frac{p_K}{\text{GeV}} \end{cases} \tag{2.1}$$

Therefore, only a fraction of the produced mesons decays in a tunnel with length L_{tunnel}. Based on equation 2.1, for 8 GeV pions and kaons there is a 1/e reduction of the initial yield after 450 m (π) and 60 m (K), respectively.

The focusing mechanism affects the neutrino beam intensity and energy distribution. There exist different types of conventional neutrino beams[30]:

- **Wide Band Beams**. Charge and momentum selection is performed mainly by horns. It results in an intense beam with a widespread of energies. This solution leads to high contamination caused by the mesons decaying before charge and energy selection.

- **Narrow Band Beams**. Unlike wide-band beams, where the momentum selection is performed only by the horn, this technique requires charge and energy selection after focusing. This approach results in a lower-intensity neutrino beam but with less momentum spread and a less polluted beam.

- **Off-axis Beams** These are wide-band beams operated with a detector located off the beam axis. Due to the two-body kinematics, the resulting neutrino beam has a narrow energy spread even if the beam intensity is reduced compared with an on-axis beam.

Most conventional beams operates based on pions and kaon decays to produce neutrinos. Non-conventional approaches have also been proposed,

based on the decay of beta unstable ions (Beta Beams)[31] or stored muons (Neutrino Factories) but these technologies are not mature yet.

2.2 The ENUBET baseline beamline

Conventional neutrino beams are sources of muon neutrinos originating from pion decays, mixed with a small fraction of electron neutrinos produced by kaon and muon decays. The ENUBET beam is a monitored narrow band beam where the ν_e is enhanced instead of being suppressed. The goal is to monitor lepton production at single particle level with an instrumented decay tunnel [32]. The proton beam is directed towards the target and secondary

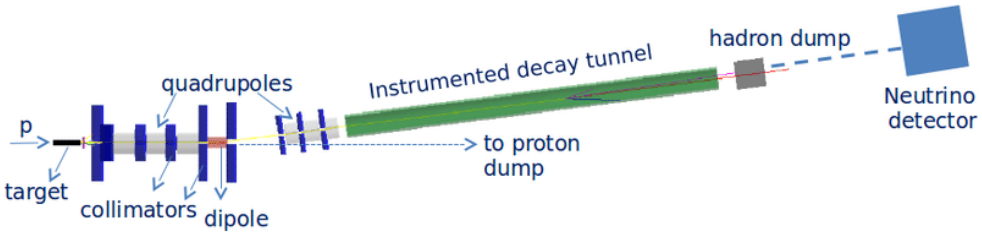

Figure 2.3: G4BL visualisation of the "Baseline" ENUBET line. The length of the transfer line is about 30 m, followed by a 50 m length instrumented decay tunnel. The secondary hadrons are stopped in the hadron dump while the primary protons to an external proton dump.

hadrons produced in the interactions with the target are momentum and sign selected. The secondary beam is composed by π^+ and K^+ and is designed to have an average momentum of 8.5 GeV and - in its original design proposed in 2015 - a $\pm 20\%$ momentum bite [33]. The positrons are identified in the decay tunnel by calorimetric techniques. The secondary beam momentum and momentum bite are optimized in order to have only K producing ν_e and a good identification capability for positrons. The ratio between ν_e and ν_μ produced by K and π decays is given by:

$$R_{K/\pi} \cdot BR(Ke3) \cdot \frac{[1 - e^{L/\gamma_K c\tau_K}]}{[1 - e^{L/\gamma_\pi c\tau_\pi}]} \tag{2.2}$$

where $R_{K/\pi}$ is the ratio between K and π mesons produced at the target and L is the length of the decay tunnel. The $Ke3$ branching ratio, $BR(Ke3)$ is 5.07 $\pm$ 0.04 %[18]. Assuming, $R_{K/\pi} = 10\%$, the graph (2.4) depicts the

scaling of equation 2.2, ν_e/ν_μ ratio as a function of the parent momentum both for mesons and for daughter muons.

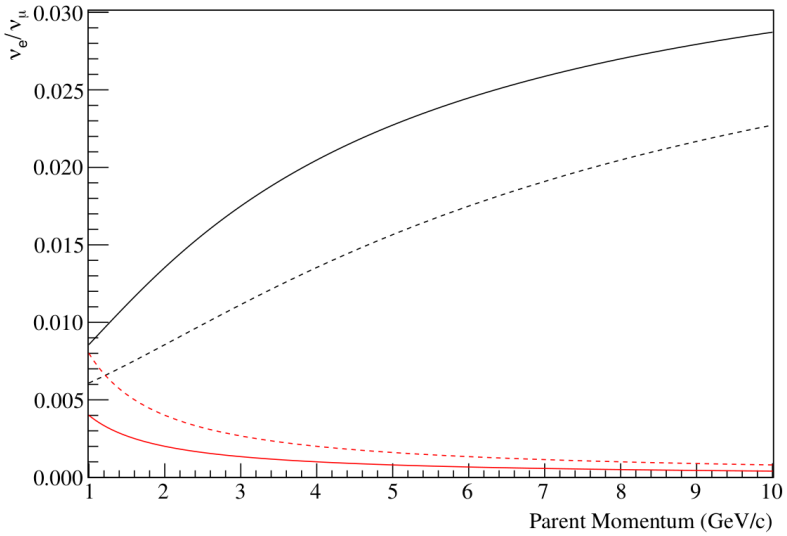

Figure 2.4: Approximate scaling of the ν_e/ν_μ fluxes ratios as a function of the momentum of secondaries (black lines) and from muon decay in flight (red lines). The continuous (dashed) line corresponds to a 50 m (100 m) decay tunnel. [32]

Two-body decays ($\pi^+ \to e^+ + \nu_e$ and $K^+ \to e^+ + \nu_e$) can be neglected as they are chirality-suppressed. Since K_{e3} is a three-body decay, positrons are distributed at angles much larger ($\sim$ 22 times larger) than the muons from the π decay $\pi^+ \to \mu^+\nu_\mu$ and the beam divergence [32]. It follows that the instrumentation of the decay tunnel as a hollow cylindrical calorimeter allows the separation between the positrons from K_{e3} and this contamination.

Based on a Monte-Carlo simulation, the fluxes at the designed average momentum of 8.5 GeV are estimated to be [32]:

$$\frac{\Phi_{\nu_e}}{\Phi_{\nu_\mu}} = 1.8\% \text{ for } K_{e3}$$

$$\frac{\Phi_{\nu_e}}{\Phi_{\nu_\mu}} = 0.06\% \text{ for } \mu \text{ decay in flight.}$$

All other particles that do not decay are dumped at the end of the tunnel and do not cross the instrumented areas. Neutral and non-interacting particles are separated at the first bending dipole and dumped in the proximity of the target area.

Focusing	π^+**/PoT** (10^{-3})	K^+**/PoT** (10^{-3})	**Extraction length**	π**/cycle** (10^{10})	K**/cycle** (10^{10})
Horn-based	77	7.9	2 ms	347	36
Static	19	1.4	2 s	86	6.3

Table 2.1: Expected rates of π^+ and K^+ in [6.5÷10.5 GeV] range at the decay tunnel entrance for the two possible focusing schemes. [34]

2.2.1 Production and transport of secondaries

The focusing of secondaries produced in the proton-target interactions can be obtained with either conventional magnetic horns or with a static focusing system. In the static focusing system, quadrupoles are placed directly downstream the target while the horn-based design needs a focusing magnetic horn downstream of the target. The theory and technical challenges of these configurations will be further discussed in Chapter5.

Baseline beamline design

In the ENUBET baseline design, both horn-based and static focusing options have been studied. The latter offers numerous advantages in terms of cost, ease of technical implementation, as well as the performance of particle identification. In the static focusing system, quadrupoles and a set of dipoles are placed downstream of the primary target. The length of the transfer line is minimized to reduce early kaon decay, before the entrance of the tunnel. To prevent undecaying particles to hit the instrumented decay tunnel, the beam envelope of the transported beam is small. In the baseline version of the line, the optics are optimized to transport at 8.5 GeV and 10% momentum bite. Following several iterations and optimization studies, the best configuration achieved consists of a quadrupole triplet followed by a bending dipole followed by another quadrupole triplet. The dipole and all the quadrupoles have an aperture radius of 15 cm. The dipole field is 1.8 T providing a bending angle of 7.4°. Proton extraction needs to be slower than current long-baseline neutrino beams ($\mathcal{O}(10\,\mu s)$) to keep the particle rate in the decay tunnel at a sustainable level. Moreover, a static focusing system can be operated in DC mode and there is no intrinsic time limit for proton extractions, up to several seconds, and particle rate could be reduced to suppress pile up. In Table 2.1 are summarized the results obtained with both focusing systems. Figures 2.5 and 2.6 show the expected π^+ and K^+ spectra respectively in the static focusing system, while figure 2.7 represents

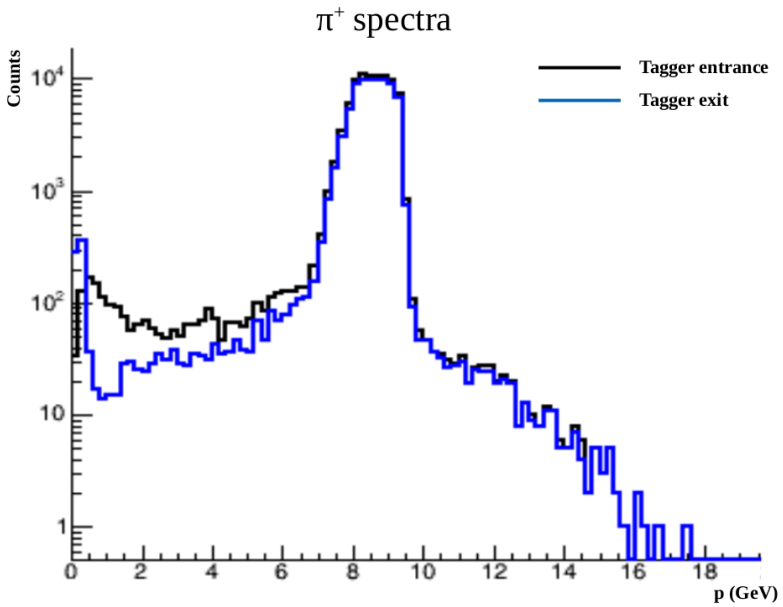

Figure 2.5: π^+ spectra at tagger entrance (black) /exit (blue) for the static baseline focusing system.

the rates of primary and secondary particles along the decay tunnel. For the current baseline beamline design, the signal-to-noise ratio of positrons is S/N $\simeq$2 with an efficiency of about 20%[36]. The background is dominated by halo pions, i.e. off-momentum undecayed pions transported down to the entrance of the decay tunnel that hits the tunnel wall. This S/N ratio is sufficient for flux monitoring at the percent level.

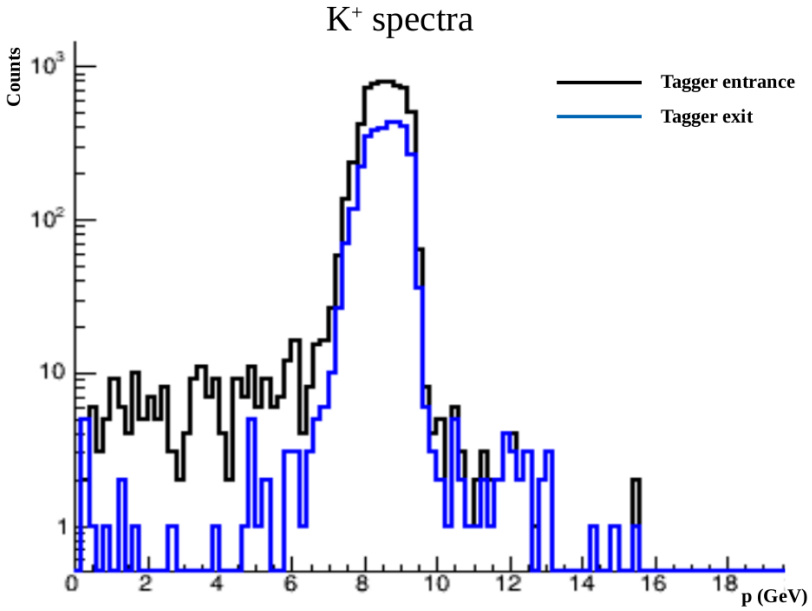

Figure 2.6: K^+ spectra at tagger entrance (black) /exit (blue) for the static focusing system.[35]

2.3 Instrumentation

The electromagnetic detector that will instrument the decay tunnel for the reconstruction of the leptons produced by K (e^+, μ^+) has been fully implemented in Geant4, together with the station that will monitor the muons produced from the decay of the π after the hadron dump. The structure of the decay tunnel from a detector point of view will be explained more in depth in the Chapter7.

2.3.1 The Tagger

The ENUBET decay tunnel consists of a 50 m long evacuated beam-pipe (40 cm radius) surrounded by the positron tagger. In the original ENUBET proposal, it had an inner radius of 40 cm and an outer radius of 57 cm but the inner radius has been extended to about 1 m in the baseline beamline to fully contain the envelope of secondary particles (pion, kaons, and the proton contamination). The tagging detector, that is, the instrumentation monitoring the large-angle positrons, is a hollow cylinder surrounding the 40 m long decay tunnel. Since the decay products are forward boosted, the calorimeter placed in the walls of the tunnel is thick enough to provide containment

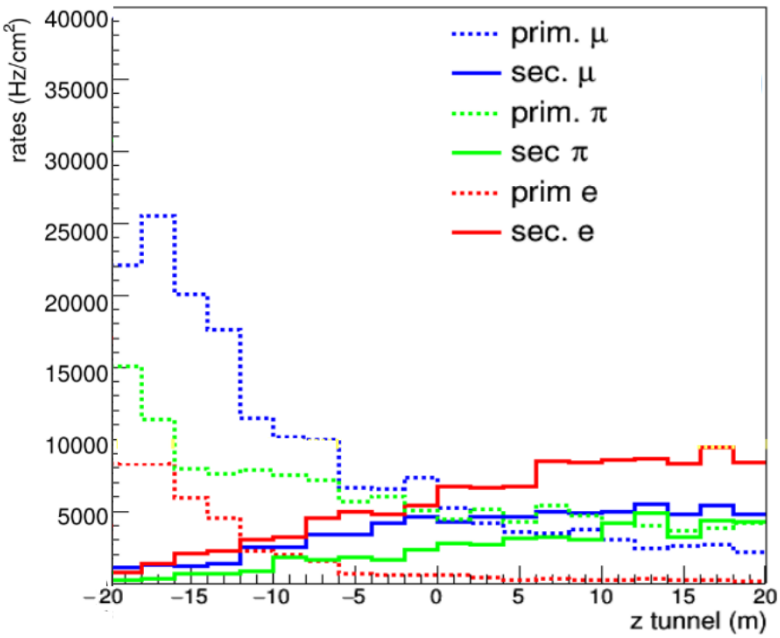

Figure 2.7: Particle rates along the decay tunnel for static focusing system solution and 4.5×10^{13} pot in 2 s (400 GeV).

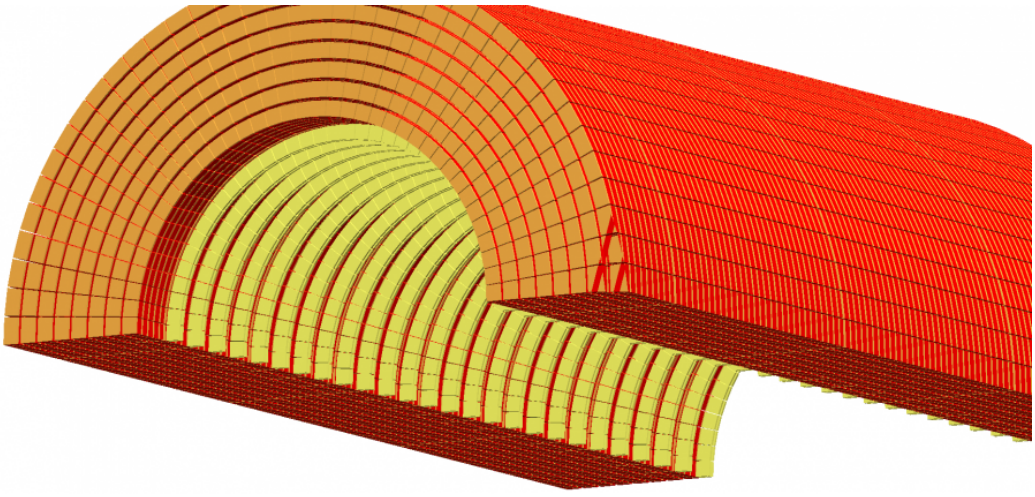

Figure 2.8: View of a section of the ENUBET instrumented decay tunnel

for nearly all particles originating from kaon decays. The energy and angle distribution of the positrons from K_{e3} decays is shown in Fig.2.9 and Fig.2.10 (red continuous line). Positrons in the decay tunnel are identified

by calorimetric techniques, exploiting the longitudinal shower development for particle identification. Photon rejection is achieved by a "t_0 layer", a pre-shower detector that provides the absolute time of arrival of the charged particle and is used to veto neutral particles in the calorimeter.

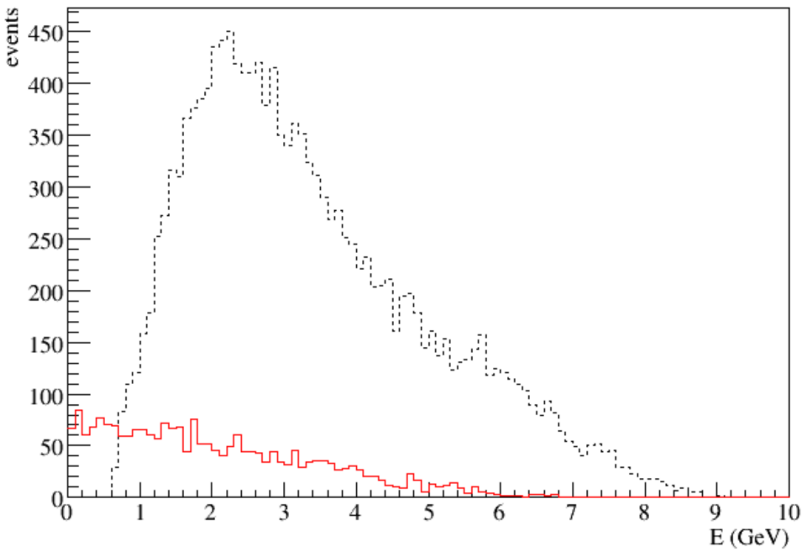

Figure 2.9: Energy distribution of positron (red continuous line) and pion (black dashed) from kaon decays hitting the calorimeter for $10^5\,K^+$ at the entrance of the decay tunnel in the 2015 ENUBET proposal [32].

The particle decays in the tunnel, the crossing of the t_0 layer, and the calorimeter response to charged and neutral particles have been simulated through GEANT4. Over the year, the ENUBET collaboration has developed an end-to-end simulation that includes the event trigger, event builder, particle selection, and particle identification. In particular, it demonstrated that moderate calorimetric performance is needed to achieve the monitoring efficiency requested by ENUBET. They correspond to:

$$\frac{\sigma_E}{E} < \frac{95\%}{\sqrt{E(GeV)}} \oplus 7\% \qquad \text{for hadrons} \tag{2.3}$$

$$\frac{\sigma_E}{E} < \frac{25\%}{\sqrt{E(GeV)}} \oplus 3\% \qquad \text{for } e^-, e^+, \gamma \tag{2.4}$$

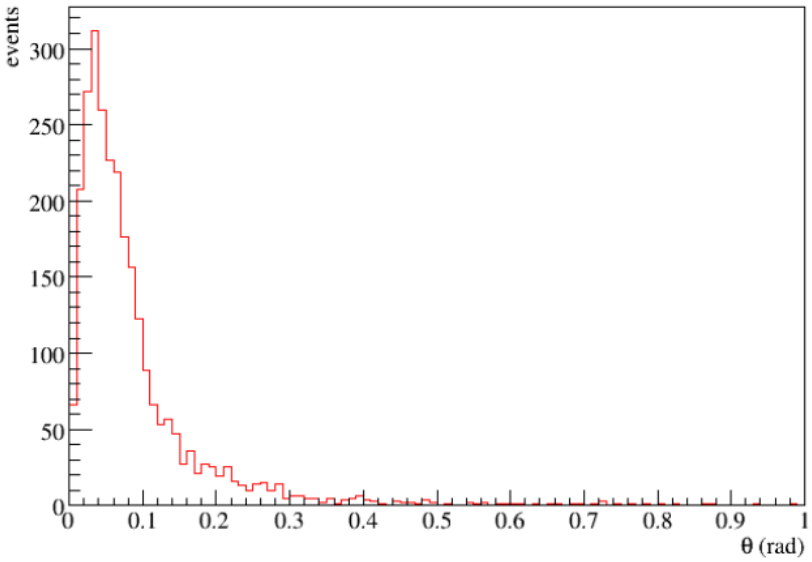

Figure 2.10: Polar angle distribution of positrons for 10^5 K^+ at the entrance of the decay tunnel.[32]

2.3.2 Muon Monitoring

As far as muon monitoring is concerned, a dedicated event builder with high purity and efficiency reconstruction has been developed. As already done for positron reconstruction, the event is reconstructed by triggering a seed. In this case, the muons are easily reconstructed by associating them with the release of a mip within a single lateral calorimeter unit in the innermost layer. This way, any tracks detected within the t-0 layer or the calorimeter will be considered in the reconstruction cluster with a time resolution of ± 1 ns.

Since the muons produced by the decay of π^+ are almost collinear with the emitted neutrinos, they escape the acceptance area of the calorimeter. Consequently, the monitoring of muon neutrinos emitted by pions involves the placement of muon detectors positioned after the hadron dump. The hadronic components emitted by the tunnel pass through and are absorbed by a first iron slab about 2 meters long. The muon detector station is composed of other iron layers alternating with muon chambers. A first preliminary version implemented in Geant4 is shown below in Fig2.11.

2.4 Positron and muon background

The main sources of muon background particles at the instrumented decay tunnel are halo muons. They are generated by secondary decay along the

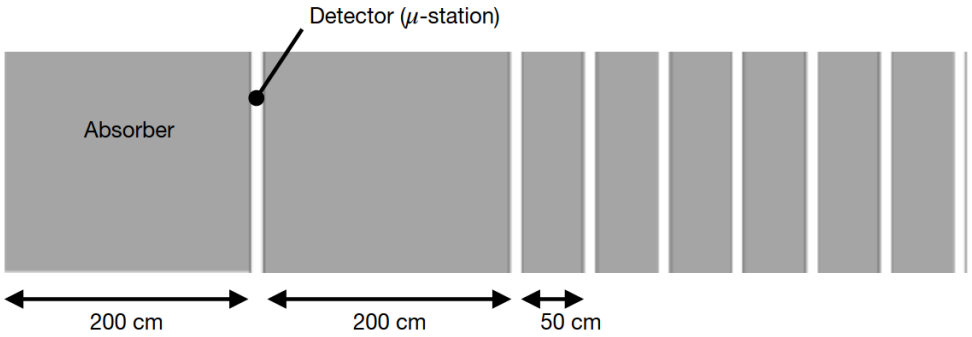

Figure 2.11: Arrangement diagram for the muon stations and absorbers that will be installed at the tagger calorimeter's end. The muon detector planes are the eight white slices, while the eight grey slabs stand in for the absorbers (made of iron or rock).

beamline and reach the decay tunnel crossing the collimators. Halo muons are off-momentum compared with muons from pion decays and can be subtracted employing the measured range in the instrumented hadron dump and their angular distribution. Since muon monitoring at the hadron dump has been introduced very recently in ENUBET, its evaluation is in progress and carried out in the framework of the ANR PIMENT (Picosecond Neutrinos for ENUBET) project. Conversely, positron background is very well studied and mostly originates from pions and high energy photons. This source of background is identified using calorimetric techniques. The signal can be recognized by studying the topology of the particles interacting at the calorimeter: hadronic showers deposit energy in many more modules than electromagnetic showers The positron identification, described in Sec.2.5, thus relied on the energy deposition pattern in all modules associated with the event. Muons from kaon decays can also be identified in the walls of the decay tunnel. Muons are virtually minimum ionizing particles (mip) and, therefore, once they interact with the calorimeter, they release constant energy along all modules. Unlike muons from pion decays, muons from $K^+ \to \mu^+\nu$ decays cross the walls of the decay tunnel and can be identified with good efficiency since halo muons are a minor background at those angles (see Sec.2.5).

Discrimination of photons from π^0 decay ($\pi^0 \to \gamma\gamma$ and $\pi^0 \to e^+e^-\gamma$) can be reached by employing an integrated photon veto: a thin plastic scintillator installed before the calorimeter (t0-layer). The t0-layer also acts as a preshower detector timing the arrival of charged particles. A basic t0-layer unit is a doublet of plastic scintillator tiles of 3×3 cm^2 surface and 0.5

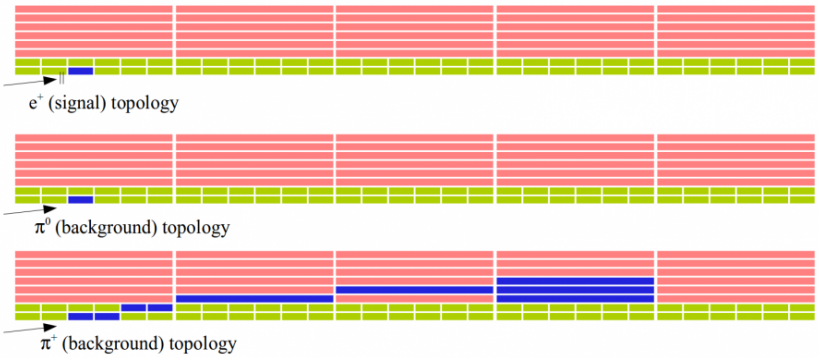

Figure 2.12: Different topologies from background and signal events[34]

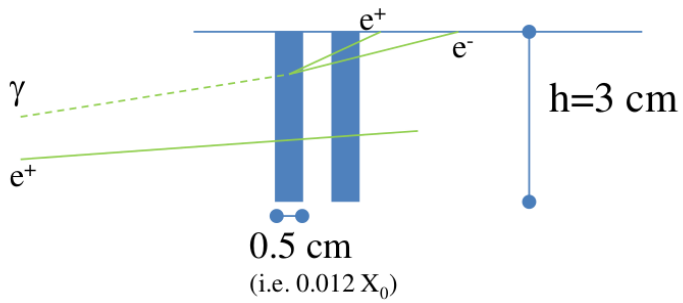

Figure 2.13: Schematic working principle of the t0-layer.[34]

cm thickness, readout by a Wavelength shifter (WLS) fiber optically linked to a silicon Photo-Multiplier (SiPM). The doublets are orthogonal to the tagger axis and mounted below the inner radius of the calorimeter. The longitudinal segmentation of the calorimeter easily allows for discriminating muons against positrons. The following table 2.2 summarizes the branching ratios of different kaon decays modes and possible decay occurring inside the decay tunnel.

2.5 Particle identification

In 2017-2018, the entire beam decay tunnel was simulated using a detailed description of the tagging calorimeters and employing as input all particles transported to the entrance of the tunnel by the transfer line. In the most updated simulation of the ENUBET beamline, particle identification in the instrumented tunnel starts from an event seed associated with a large energy deposit. The first step needed for particle identification (PID) is the definition of the event by the ENUBET Event Builder (EB). Moreover, ex-

Table 2.2: Summary of main decays occurring inside the decay tunnel

Decay	**BR**(%)
$K^+ \to e^+\pi^0\nu_e$	5.1
$\pi^+ \to \mu^+\nu_\mu$	∼100
$\mu^+ \to e^+\overline{\nu_\mu}\nu_\mu$	DIF
$K^+ \to \mu^+\nu_\mu$	63.5
$K^+ \to \pi^+\pi^0$	20.7
$K^+ \to \pi^+\pi^+\pi^-$	5.6
$K^+ \to \pi^0\mu^+\nu_\mu$	3.3
$K^+ \to \pi^+\pi^0\pi^0$	1.7

tensive work on the GEANT4 simulation of the calorimeter is needed to mitigate the effect caused by pile-up effects. The particle identification algorithm merges the events collected by different modules, called "UCMs" (ultra-compact module) if the occurrence of the energy deposit is within 1 ns. To be able to perform proper particle identification, the event needs to be first defined. In the standard positron identification analysis, the *seed* of the event is identified as the first (in time) energy deposit in a UCM. Only deposits larger than 20 MeV are considered. Charged particles will deposit energy in different UCMs and the geometrical pattern of the energy deposition can be exploited to perform particle identification (PID). Since particle showers are topologically different based on the type of the particle causing it, the collaboration used a Neural Network (NN) based on TMVA multivariate analysis to extract all calorimeter information. The NN employs the pattern of energy deposit in the UCM through a set of discriminating variables. Since 2021, the NN employs also the information of the photon veto ($t0$ layer) and was succesfully applied to identify positrons from K_{e3} and muons from kaon decays. The results are the following:

- positron from K_{e3} ($K^+ \to e^+\pi^0\nu_e$) are identified with a S/N ratio of 2 and an efficiency of 22%
- muons from $K_{\mu 2}$ ($K^+ \to \mu^+\nu_\mu$) are identified with a S/N ration of 6 and an efficiency of 34%

in the baseline beamline of ENUBET.

Chapter 3

Design of particle beams

If an experiment needs to calibrate a calorimeter or part of its instrumentation, it turns to an accelerator facility in which a beam of known energy is extracted and transported to the object of study. Beamlines can also be objects of more active roles within the accelerator chain to refine the beam or on diagnostic roles. Regarding ENUBET, it is necessary to design a secondary beamline that is able to select, focus and transport the secondary particle beam emitted by a target towards the decay tunnel. The experiment requires a beam of K^+ and π^+ mesons with nominal energy in the range of interest of DUNE,HyperK, and T2K.

Before going into the merits of the ENUBET beamline, it is necessary to introduce the necessary elements that make up a generic beamline and the physics behind particle motion.

3.1 Transverse Beam Dynamics

The particle beam properties can be controlled by magnetic elements, or combinations of those, that may affect the direction or the transverse properties of the particles ensemble. The main properties of these elements, as well as the way that they affect the particle beams are described in the following subsections.

3.1.1 Weak and Strong Focusing

It is important to define stability criteria for the particles inside the accelerator. These depend on the intensity of the focusing forces that are applied.

Weak Focusing

The first accelerators used a "weak" type of focusing: this involves the use of a magnetic field independent of the azimuth angle Θ. Therefore, the orbit at the equilibrium of the particles lies on the plane y = 0 with radius $\rho = \frac{mv}{eB}$. The motion of a particle is stable only if for small deviations around the orbit, contrasting forces arise which cause small oscillations called **oscillations of betatron**.

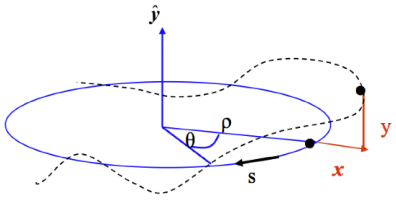

Figure 3.1: Example of a circular orbit

The stability criteria require that the Lorentz force be less than the centrifugal force for $r < \rho$ and greater for $r > \rho$.

$$evB_z(r) \quad \begin{cases} < \frac{mv^2}{r} & \text{for } r < \rho. \\ > \frac{mv^2}{r} & \text{for } r > \rho. \end{cases} \tag{3.1}$$

For small oscillations from the equilibrium:

$$r = \rho + x = \rho\left(1 + \frac{x}{\rho}\right) \tag{3.2}$$

$$\frac{mv^2}{r} \approx \frac{mv^2}{\rho}\left(1 - \frac{x}{\rho}\right) \tag{3.3}$$

Considering the formula of the contrasting force:

$$F_x = \frac{\gamma mv^2}{r} - evB_y \tag{3.4}$$

If the particle is moving in a uniform magnetic field, the contrasting force would be zero for any orbit. For focusing to occur, it is necessary to assume that for small deviations x from the main orbit, the field has a gradient such that:

$$B_y = B_{0y} + \frac{\partial B_y}{\partial x}x = B_{0y}\left(1 + \frac{\rho}{B_{0y}}\frac{\partial B_y}{\partial x}\frac{x}{\rho}\right) \tag{3.5}$$

if a **field index** $\mathrm{n} = -\frac{\rho}{B_{0y}}\frac{\partial B_y}{\partial x}$ is defined, the strength becomes:

$$F_x = \frac{\gamma m v^2}{r} - evB_{0y}\left(1 - n\frac{x}{\rho}\right) \tag{3.6}$$

This function is also valid when n = 0, i.e. in a homogeneous magnetic field. This means that for homogeneous fields, the orbits remain circular and all the diverging particles will meet again after 180° of revolution.
Finally, the equation of motion becomes:

$$\ddot{x} + \omega_x^2 x = 0 \tag{3.7}$$

It is nothing more than a harmonic oscillator with oscillation frequency (or betatron) $\omega_x = \omega_0\sqrt{1-n}$. The oscillation imposes a restriction on the values that n can take, in particular $\mathbf{n<1}$.

All the considerations made so far only dealt with motion in the horizontal plane. If, in the presence of a homogeneous magnetic field, the particle received a kick on the vertical plane it would drift out of orbit. It is therefore necessary to introduce a contribution along the vertical axis of the orbit (y according to the considerations made so far).

$$F_y = -C \cdot y, \qquad C = const. \qquad \gamma m\ddot{y} = evB_x \tag{3.8}$$

This results in a finite horizontal component of the magnetic field. From Maxwell's equations it results that $\frac{\partial B_x}{\partial y} - \frac{\partial B_y}{\partial x} = 0$, so:

$$B_x = -n\frac{B_{0y}}{\rho}y \tag{3.9}$$

Therefore, in addition to the equation of motion on the horizontal plane, the equation of motion on the vertical plane is equal to:

$$\ddot{y} + \omega_y^2 y = 0 \qquad \omega_y = \omega_0\sqrt{n} \tag{3.10}$$

This last equation places a further restriction on the sign of n, leading us to conclude that weak focusing requires that:

$$\mathbf{0 < n < 1} \tag{3.11}$$

From these equations of motion it can be deduced that a particle performs less than one oscillation per revolution since the frequency of betatron is lower than that of revolution.

Strong Focusing

The weak focusing principle presents problems when considering large circles for accelerators. Since the wavelength of the betatron oscillations is larger than the circumference of the machine, the deviation of the particle from the main orbit increases with the radius. This effect would result in the need for magnets with very large apertures.
This problem can be avoided if the "strong focusing" (n $\gg$1/n$\ll$-1) method is applied. These conditions are applicable only in case of failure of the primary condition that has been imposed on the weak focusing calculations, that is, that the field is independent of the azimuth angle. Therefore, it was chosen a magnetic field that drastically increases with increasing radius (n $\ll$ -1) alternating with one that instead decreases as the radius increases (n$\gg$1).

3.1.2 Particle Motion and Transportation Matrix

Hill equations

$$\begin{aligned} &x'' - \left(k - \frac{1}{\rho^2}\right)x = \frac{1}{\rho}\frac{\Delta p}{p_0} \\ &z'' + kz = 0 \end{aligned} \tag{3.12}$$

These equations are the equations of the motion of a particle inside a circular accelerator and are called **Hill's equations**.
The most general form is the homogeneous one, namely: $y'' + K(s)y = 0$ with $K(s+L) = K(s)$ and $K(s) = -\frac{eg}{p_0} + \frac{1}{\rho^2}$.
In the specific case for which K(s)= const. > 0, the equation represents a simple harmonic oscillator with independent solutions:

$$\cos\sqrt{K}s \quad \& \quad \sin\sqrt{K}s \tag{3.13}$$

In the more general case K = K(s) and the solution can be expressed as:

$$y(s) = y_0 C(s) + y_0' S(s) \tag{3.14}$$

where C(s) and S(s) are sinusoidal periodic functions representing the trajectories and y_0 and y_0' are the initial conditions of the homogeneous equation a $s = s_0$.
y and y' are obtainable through a matrix transformation from y_0 e y_0':

$$\begin{pmatrix} y \\ y' \end{pmatrix}_s = M(s/s_0) \begin{pmatrix} y_0 \\ y_0' \end{pmatrix}_{s_0} \tag{3.15}$$

with:

$$M(s/s_0) = \begin{pmatrix} C(s) & S(s) \\ C'(s) & S'(s) \end{pmatrix} \tag{3.16}$$

and:

$$\begin{pmatrix} C(s_0) & S(s_0) \\ C'(s_0) & S'(s_0) \end{pmatrix} = \begin{pmatrix} 1 & 0 \\ 0 & 1 \end{pmatrix} \tag{3.17}$$

Later the consequences deriving from the matrix M(s/s_0) will be discussed. Thus, the more general expression of Hill's equation (K(s) $\neq$ const.) Has two independent solutions:

$$y_1(s) = e^{i\mu s/L} p_1(s), \qquad y_2(s) = e^{-i\mu s/L} p_2(s) \tag{3.18}$$

where μ is the characteristic coefficient of the differential equation and is given by the condition $\cos\mu = \frac{1}{2}\mathrm{tr}M(s)$, while p_1 and p_2 are two periodic functions. The solutions are no longer independent if μ is real.
The matrix notation of the solutions of the equations of motion is particularly useful when approximating the solution K(s) described above by the Hill equations to a constant. This way, the matrix elements can be expressed analytically and the solution of the entire lattice of the optical elements of the magnets is expressed through the product of characteristic transfer matrices for each element.

These equations also apply to machines with separate function magnets. A dipole will have equations for k = 0 considering only the weak focusing curvature effects, while a quadrupole has the k term prevailing and has no curvature as the trajectory inside the magnet is linear. Consequently, the term $\frac{1}{\rho^2}x$ is defined as the **weak focusing term**, while the k term, preponderant of the quadrupoles, as the **term of strong focusing**.

3.1.3 Magnets

Bending Magnet

The field generated for $\mu_r \gg 1$ is:

$$B_0 = \frac{\mu_0 n I}{h} \qquad h = \text{gap's height;} \tag{3.19}$$

The radius of curvature for a particle with momentum p and charge e is given by:

$$\frac{1}{\rho} = \frac{eB}{p} = 0.2998 \frac{B_0[T]}{p[GeV/c]} \tag{3.20}$$

The magnetic field is assumed to abruptly stops outside the magnet. The

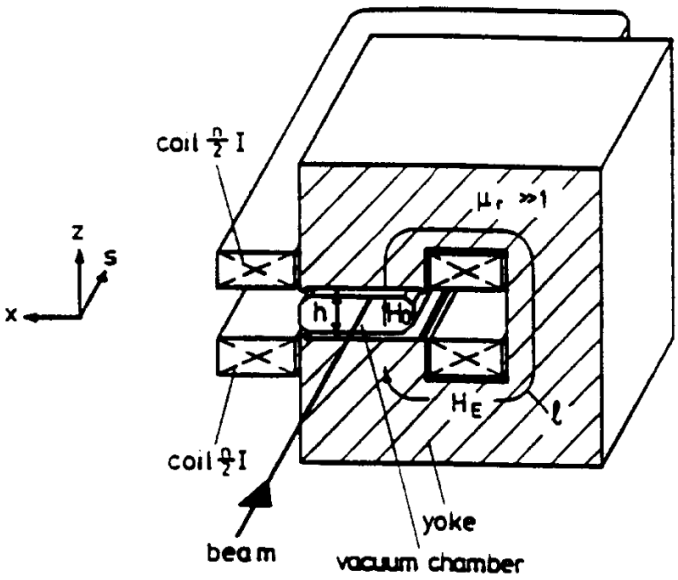

Figure 3.2: Schematic example of a dipole.[37]

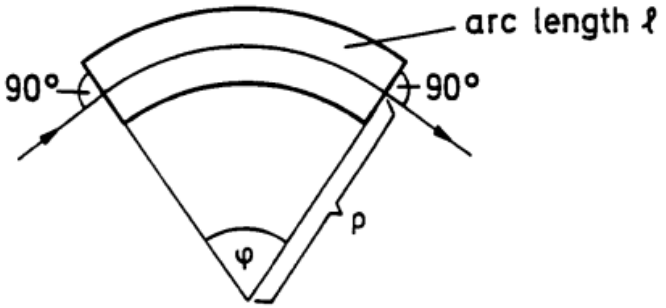

sides of the magnet are considered perpendicular to the curvature. Transfer matrices with $\phi = \frac{l}{\rho}$ are:

$$M_x = \begin{pmatrix} \cos\phi & \rho\sin\phi & \rho(1-\cos\phi) \\ -\frac{1}{\rho}\sin\phi & \cos\phi & \sin\phi \\ 0 & 0 & 1 \end{pmatrix} \quad M_z = \begin{pmatrix} 1 & l & 0 \\ 0 & 1 & 0 \\ 0 & 0 & 1 \end{pmatrix} \tag{3.21}$$

Often, instead of the sector magnets described above where the beam trajectory is perperpendicular to the face of the magnet, rectangular magnets are used since they are easier to construct and laminate. In this case, the pole faces are rotated with respect to the beam entrance, typically be $\theta/2$, where θ is the magnet's deflection angle. What distinguishes them from a magnetic dipole sector is the presence of the magnetic field entering and leaving the

magnet such that it has an angle $\delta = \phi/2$.

Quadrupole Magnet

When symmetrical solenoid coils are used, an effect of "magnetic lens" arises whereby the purely longitudinal magnetic field inside the coil has a radial component on the outside. A particle crossing perfectly the center of a solenoid magnet will not be affected by any force. On the other hand, any particle traveling off-axis will be stirred by an azimuthal acceleration inversely proportional to their momentum. The magnet thus shown in the

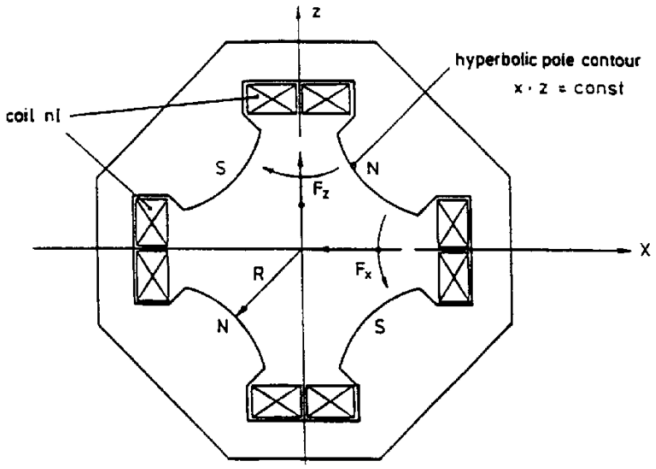

Figure 3.3: Generic quadrupole cross section[37].

figure represents a focusing on the horizontal axis and a vertical defocusing for a positively charged particle. It exerts a linear field along the axes:

$$B_z = -gx \qquad B_x = -gz \tag{3.22}$$

In the intervening space where there are no magnets or iron, maxwell's equation holds for which: $\nabla \times \mathbf{B} = 0$. Thus, the field can be written as the gradient of a potential:

$$\mathbf{B} = -\nabla V \text{ con: } V = gxz \text{ where: } g = \frac{2\mu_0 nI}{R^2} \tag{3.23}$$

As far as the dipole was concerned, the radius of curvature ρ was the main focus of discussion. By analogy, its optical properties are associated with the gradient of the quadrupole. The normalized quadrupole intensity at the particles' momenta is defined as:

$$k = \frac{eg}{p} \qquad k[m^{-2}] = 0.2998 \frac{g[T/m]}{p[GeV/c]} \tag{3.24}$$

If l represents the length of the quadrupole, then its focal length f is given by:

$$\frac{1}{f} = k \cdot l \tag{3.25}$$

If $f \gg l$, it's possible to use the"thin lenses" approximation, regardless of the absolute value of l. An important property of the quadrupole is that the horizontal and vertical components of the force depend only on the corresponding vertical and horizontal positions of the particle's trajectory.

$$F_x = evB_z(x,z) = -evgx \qquad F_z = -evB_x(x,z) = evgz \tag{3.26}$$

Consequently, in a linear machine, the horizontal and vertical betatron oscillations are **completely decoupled**.

As for the matrix representation for the coordinate translation of a particle passing from a point x_0 to a point x_1 through a quadrupole magnet: $\frac{1}{\rho} = 0$. $\phi = l\sqrt{|k|}$, per $k > 0$:

$$\begin{aligned} M_x &= \begin{pmatrix} \cosh\phi & \frac{1}{\sqrt{|k|}}\sinh\phi & 0 \\ \sqrt{|k|}\sinh\phi & \cosh\phi & 0 \\ 0 & 0 & 1 \end{pmatrix} \\ M_z &= \begin{pmatrix} \cos\phi & \frac{1}{\sqrt{|k|}}\sin\phi & 0 \\ -\sqrt{|k|}\sin\phi & \cos\phi & 0 \\ 0 & 0 & 1 \end{pmatrix} \end{aligned} \tag{3.27}$$

These matrices represent horizontal defocusing and vertical focusing. For $k < 0$ the opposite is obtained and the matrices are swapped.

All the elements described so far are defined as static elements since they operate at constant current or are pulsed for long periods ($O(s)$).

3.1.4 Quadrupole multiplets

A single quadrupole focuses the particles along one plane and defocuses them on the other: a net focusing effect in both transverse dimensions can be achieved with a combination of them (from two quadrupoles onward). Three quadrupoles in series (i.e. a quadrupole triplet) are a common choice as a focusing stage because they allow achieving similar focusing properties both in the vertical and horizontal plane.

In terms of describing the motion of a particle passing through a quadrupole multiplet, the composition of several dipoles or quadrupoles is obtained by

multiplying the respective transfer matrices in the correct order. For example, it is possible to consider a focusing quadrupole, drift space, and a defocusing quadripole. Assuming that the focal lengths are the same and that it can be approximated with a thin lens:

$$\begin{aligned} M_x &= \begin{pmatrix} 1 & 0 & 0 \\ \frac{1}{f} & 1 & 0 \\ 0 & 0 & 1 \end{pmatrix} \begin{pmatrix} 1 & l & 0 \\ 0 & 1 & 0 \\ 0 & 0 & 1 \end{pmatrix} \begin{pmatrix} 1 & 0 & 0 \\ -\frac{1}{f} & 1 & 0 \\ 0 & 0 & 1 \end{pmatrix} \\ &= \begin{pmatrix} 1 - \frac{l}{f} & l & 0 \\ -\frac{l}{f^2} & 1 + \frac{l}{f} & 0 \\ 0 & 0 & 1 \end{pmatrix} \end{aligned} \tag{3.28}$$

As for the vertical transfer matrix, just invert f into $-f$:

$$M_z = \begin{pmatrix} 1 + \frac{l}{f} & l & 0 \\ -\frac{l}{f^2} & 1 - \frac{l}{f} & 0 \\ 0 & 0 & 1 \end{pmatrix} \tag{3.29}$$

3.2 Hadron Beam Lines

This section covers more in details what defines a beamline and the different stages. As introduced above, the produced mesons at a target need to be focused, momentum selected and transported towards the decay volume. Generally, a secondary beamline is composed of three stages made up in turn of different elements. It is important that the beamline takes into account the decay length of the mesons it is designed for. Fig. 3.4 shows the survival rate of pions and kaons at different energies as a function of the distance traveled, and therefore of a hypothetical beamline length.

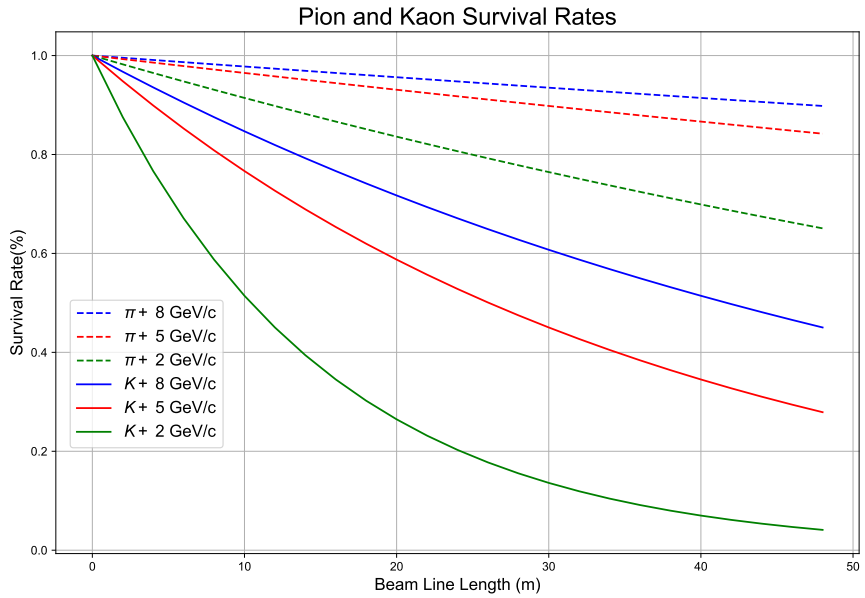

Figure 3.4: Survival probabilities for low momentum pions and kaons, assuming a beamline with a maximum length of 50 m.

3.2.1 Acceptance Stage

The production of secondary hadron or lepton beams via the interaction of a primary beam impinging on a target material is the most common technique worldwide for providing experiments or facilities with particle beams of different intensities, compositions and momenta. The study of the optimal targets for hadron production will be addressed in the next chapter. Primary particles not interacting with the target material continue undeflected through

the rest of the beamline, having too high an energy for the magnets' currents. On the contrary, the hadrons of interest are collected and transported through the first phase of "acceptance". The acceptance of the beam exiting the target is determined in first approximation by the geometric acceptance of the first element, i.e. a multiplet of quadrupoles or a magnetic horn. This is determined by the position relative to the target and the aperture of the magnet [38].

3.2.2 Momentum Selection & Final Focusing Stages

Downstream the acceptance stage, the mesons are selected by momentum and charged through the use of a magnetic spectrometer. The spectrometer function is generally performed by one or two dipoles. A central quadrupole can perform the function of the focusing lens, a point where it is possible to collimate the beam for greater momentum resolution. It is usually beneficial to recombine the dispersed rays of particles such that their trajectories are independent of the momentum. This function is performed by "field-lenses" or by correctly positioned dipoles. In the case of ENUBET Multi Momentum beam line, a quadrupole magnet is used to recombine the dispersive particles towards the center of the second dipole. Finally, a final quadrupole multiplet is employed to define the required beam shape before it reaches the detector. One of the requirements could be to make the beam parallel, as in the case of ENUBET to prevent it from contaminating the instrumented walls of the decay tunnel. In-between or downstream of these quadrupoles is where the particle identification instrumentation is placed.

Chapter 4

Target Studies

4.1 Particle Production

The study of secondary particles strictly depends on the choice of targets on which a primary beam of high-energy protons impinges. Depending on the energy, material, and geometry of the target, the secondary beam will have different characteristics. Neutrino beams are conventionally originated from the decay of charged mesons ($\pi^{\pm}$, $K^{\pm}$). It is therefore crucial to study the production of secondaries to obtain a beam that satisfies experiment's requirements. Experimental and empirical observations suggest that there is a direct correlation between the mass number of the material constituting the target, and the yield of secondary particles from the target. Experiments that require high-intensity neutrino beams often use low-Z targets [39] to compensate for reduced yield by exploiting greater primary beam power. The advantage of using materials such as beryllium, graphite, or other carbon-based compounds lies in their resistance to radiation damage [40], especially if the total number of protons exceeds 1×10^{19}/year, as is expected for ENUBET.

The neutrino flux is determined by the production of secondary hadrons emitted from the target, creating the greatest source of uncertainty. Although this can be extrapolated from models derived from experimental results[41], it remains above 10% [42, 43, 44]. The number of pions produced per proton hitting the targets is directly proportional to the energy of the primary protons [45]. In turn, the momentum of the secondary particles produced at the target, and consequently of the neutrinos, is also strictly dependent on the momentum of the primary protons. There are several accelerator driven systems capable of producing a wide momentum range of protons at high or low repetition. Facilities such as J-PARC MR [46] compensate for the low energy of primaries by operating at high repetition, while at the CERN

SPS, proton beams of 400 GeV/c can be either fastly (25ns) or slowly (4.8s) extracted. It is therefore important to determine which is the optimal target by tuning different parameters to obtain a neutrino beam that is suitable for the physical purpose of the experiment. Once the energy of the primaries to be used has been determined, it is essential to determine the material and geometry of the target. The size of the target is fundamental to determine the probability of re-interaction and absorption of particles within the material, consequently the production rate of secondary mesons. An optimal target does not depend only on the size, but also on the mechanical and thermodynamic limits that could compromise it during the operation, especially when using high intensity beams [47].

Depending on the beam structure, the deposited energy by the high intensity, high energy beams can be quite challenging. Even in the case of slowly extracted beams (pulse length $>$ 700 ms), heat dissipation needs to be seriously considered. The main parameters that determine a target's ability to resist heat are the heat capacity and tensile properties of the material. Once these parameters have been determined, it is possible to choose the most suitable thermal dissipation system. There are several thermal dissipation systems capable of lowering the target temperature during the operation. It is possible to dissipate heat through the container itself through conductive systems or by radiation. Conductive internal heat transfer is very effective in metal targets, while radiant heat transfer is better suited for high-emissivity refractory materials and inserts, such as graphite [48]. When considering an optimization study, it is necessary to consider all these aspects and reach a trade-off for a target that is more performing in terms of production and resistance, although often these requests are in contrast. A larger target can support a more powerful beam, but at the same time lose meson production due to internal resorption of the particles.

4.2 Extraction of primary protons

Before going into details about the target optimization study, it is good to deepen how the primary beam that impinges on the target itself is extracted.

Neutrino beams, in general, have always relied on primary proton sources derived from synchrotrons. For instance, the J-PARC Main Ring has been employed for T2K [49], the CERN Super Proton Synchrotron (SPS) for the West Area Neutrino Facility [50] and CNGS [51], while the Fermilab (FNAL) Main Injector and Booster for the NuMI beamline [52] and MiniBooNE [53], respectively.

There are two types of primary beam extraction: fast and slow extraction.

The main feature of fast extraction consists in the extraction of all primary protons inside the synchrotron in a time less than that of revolution, typically in the $\mathcal{O}$(1 - 10 µs) range. On the contrary, slow extraction is addressed when the beam is extracted in spills several seconds long. This latter scheme is characterized by an unstable motion of the particles in the transverse plane of the phase space.

Fast Extraction

Most conventional neutrino beams rely on the fast extraction method, so it is possible to use magnetic horns whose acceptance is higher than static beam focusing systems. This expedient allows to obtain a higher order of magnitude on the rate of mesons transported, and consequently of neutrinos detected by the detector. However, a fast extraction system causes a strong thermal stress on the target, which has to sustain a significant energy deposit due to the high rate. Furthermore, this system impacts the diagnostic system inside the beamline. The instrumentation must be able to sustain a high rate of protons and secondaries in a very short time.

Slow Extraction

In the case of experiments where it is necessary to tag particle by particle inside the detector, a fast extraction system is not usable due to the too high rate. The use of a slow extraction system, however, does not allow the use of magnetic horns, as the Joule heating due to the long current pulses would compromise its operation. Parallel studies are investigating the possibility of using a pulsed horn with this scheme. A notable example is the ESSνSB project [54, 55].

There are several examples of neutrino physics experiments that exploit the use of both extraction systems. Experiments located at J-PARC [56, 49] or Fermilab [52, 53] use a spill of protons of a few microseconds while the SPS-CERN machine can provide spills with an intensity of 4.5×10^{13} protons for both fast extraction cycles, as for the CNGS [57, 58, 59] experiment, which spills a few seconds long. This last modality allows for the distribution of the beam on multiple targets to serve different secondary lines to the North Area. An example of a slow extraction experiment operating at CERN is ProtoDUNE, a narrow band secondary beam commissioned for the NA Neutrino Platform [38, 60, 61, 62]. The low particle rate allows you to monitor beam parameters such as particle moment and beam composition (Sec. 3.2). Recent slow extraction studies have been performed at SPS for the ENUBET experiment. The particle-by-particle reconstruction inside the decay tunnel

places a stringent limit on the rate tolerance that the instrumentation can withstand. To limit the effects of pile-up it is necessary that the beam has an extraction over several seconds and therefore the so-called "slow". However, parallel studies are investigating the possible use of a "burst-mode" extraction scheme. This technique allows the extraction of the beam over an interval of 2-to-10 ms, repeated at 10 Hz for a complete extraction [63]. This technique would allow the use of a magnetic horn and would help in cosmic background reduction. An example of this new scheme, the *burst-mode slow extraction*, can be seen in Fig. 4.1.

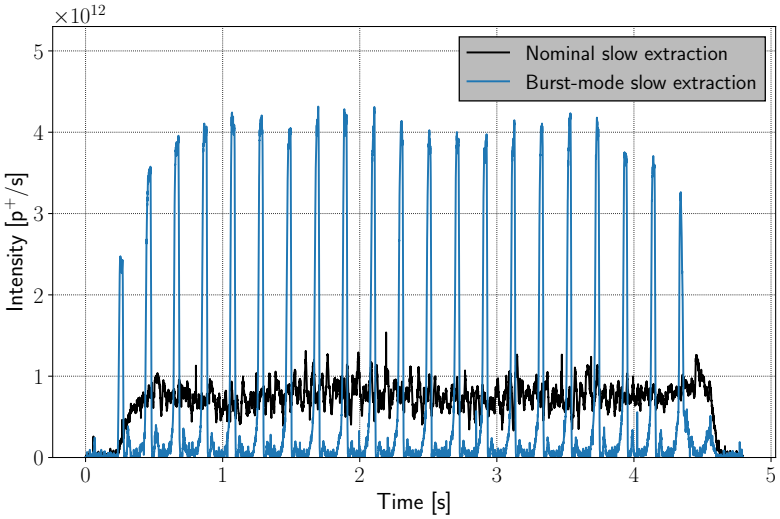

Figure 4.1: Comparison between a nominal slow extracted spill and a "burst-mode slow extraction" one. The spill profiles have been measured with a secondary emission monitor at the SPS, during dedicated machine tests. The same intensity is extracted in the two cases.

Experimental results obtained during CERN Long Shutdown 2 have demonstrated the possibility of implementing this technique at SPS. Further studies will be validated following CERN Long Shutdown 2 (LS2).

4.3 Multi-Momentum beamline target optimisation

A fundamental part of this thesis is the study of an optimal target for the ENUBET multi-momentum beamline. The study was preformed using the Monte-Carlo simulation codes FLUKA [64, 65] and G4beamline [66].

4.3.1 Optimal Primary Beam momentum

As mentioned above, the energy of the emitted secondary particles depends on the momentum of the primary beam impacting the target. It is therefore crucial to establish the optimal energy, based on those available at existing facilities, for the production of K and π mesons at the optimal momenta for neutrino beams in the range of DUNE, T2K and HyperK. Based on phenomenological calculations and measurements, the momenta where the Feynman-x, x_F is close to zero has a maximum production cross-section for hadronisation[67]. Specifically, this variable characterizes the fraction of moment that secondary particles receive from primary protons. It is a scale factor defined by the energy of the center of mass of collision. This parameter indicates the dependence on the cross section of the process, and the rate of particles produced as a function of the momentum of the primaries. The rate is maximized when the variable reaches zero. As can be seen from the Fig.4.2, a primary beam of 400 GeV/c maximizes the production of K mesons at 8.5 GeV/c. However, despite the fact that the production is maximized with this momentum, the effect could be compensated by increasing the beam power on the target.

This first estimation was verified with Monte-Carlo simulations in FLUKA testing primary energies of 50, 70, 150, and 400 GeV/c. These FLUKA results confirmed that the nominal energy of the SPS (400 GeV/c) is the best for ENUBET, especially for cross section studies in the region of interest for DUNE. This region requires a secondary mean momentum for kaons of about 8.5 GeV. The comparison of the geometry and material of the target followed.

4.3.2 Material and Dimensions

Extensive simulations using both FLUKA[64][65] and G4Beamline[66] have been carried out to determine the particle yields for various materials. FLUKA studies have shown heat increase in materials with high-Z that could make it challenging to cool down the target during the experimental runs. Therefore, in the present Ph.D. thesis, the chosen materials for charged kaon production in the momenta of interest proved to be graphite (2.23 g/cm^3 density), beryllium (1.85 g/cm^3), and Inconel-718 (8.19 g/cm^3). Each target prototype is modeled geometrically as a cylinder with various lengths and radii ranging from 10 to 30 mm. A summary of the simulated target materials and sizes is shown in Table 4.1.

The kaon yields for both graphite and beryllium are shown in Fig. 4.4 and Fig. 4.5.

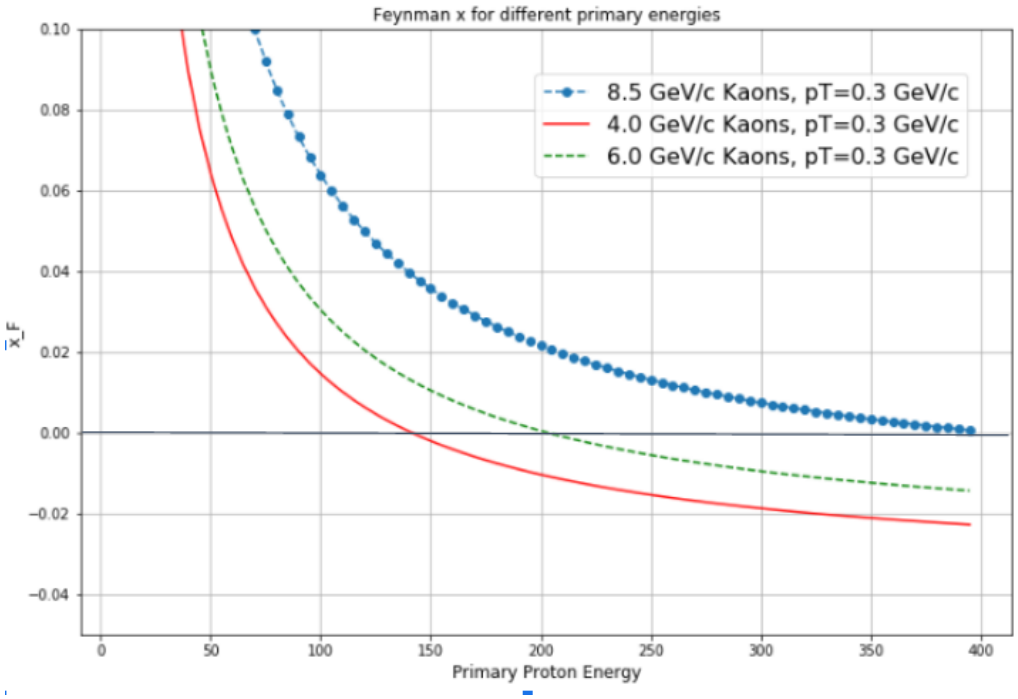

Figure 4.2: Feynman X in dependence of the primary beam momentum. It is shown that the production of 8.5 GeV/c Kaons is maximized for 400 GeV/c primary beam, while seems that for 4 GeV/c or 6 GeV/c, primary beams of lower momenta could be also sufficient.

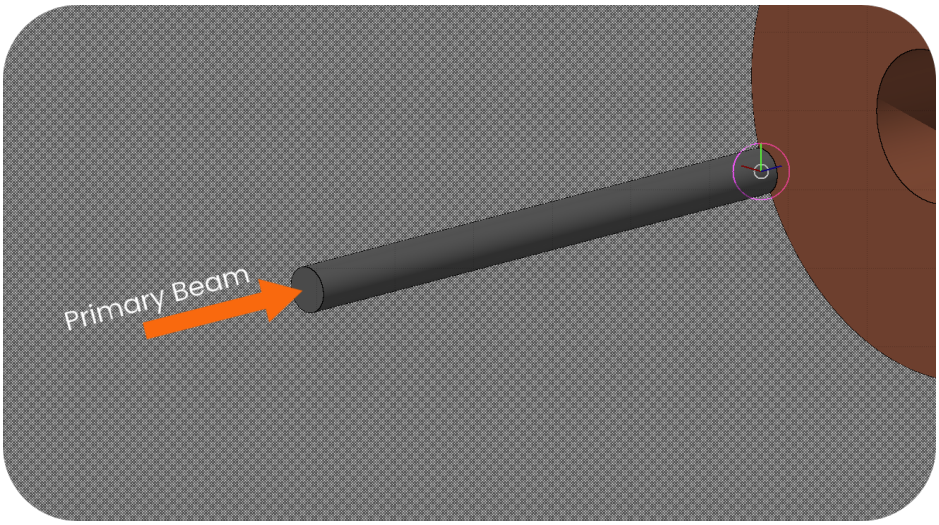

Figure 4.3: Visualization of the target modelled in FLUKA with the impinging primary beam schematics.

Table 4.1: Summary table of the different target material and lengths simulated with FLUKA. Each material has been iterated with the lengths listed.

Materials	**Lengths [cm]**		
Au	1	10	50
Carbon	3	20	80
Beryllium	5	30	110
Tungsten	8	35	140

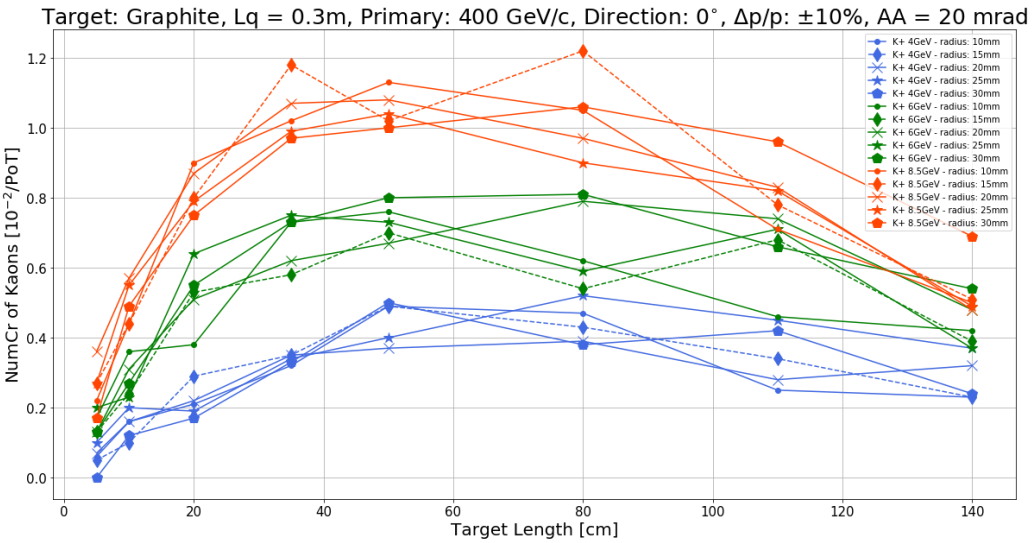

Figure 4.4: Kaon yields as a function of the graphite target length. The primary beam simulated is a 400 GeV/c proton beam. The figure of merit for this study is the number of kaons of given energy with 10% momentum bite that enters an ideal beamline with ±20 mrad angular acceptance in both planes, placed 30 cm after the target. The error bars are not plotted to ease the reading; statistical errors are negligible (1%), while the Monte-Carlo systematics amounts to $\sim$ 20%. Colors refer to different kaon's momenta while the marker style identifies the target radius.

Graphite is a well known material in the context of neutrino physics experiments. It is a material able to withstand strong thermodynamic stresses and has a good performance in terms of production of secondary mesons useful for the creation of neutrino beams. Another widely used material is Inconel, a compound already used in various applications at CERN, which however requires a complex cooling system and has not yet being analyzed in this studies.

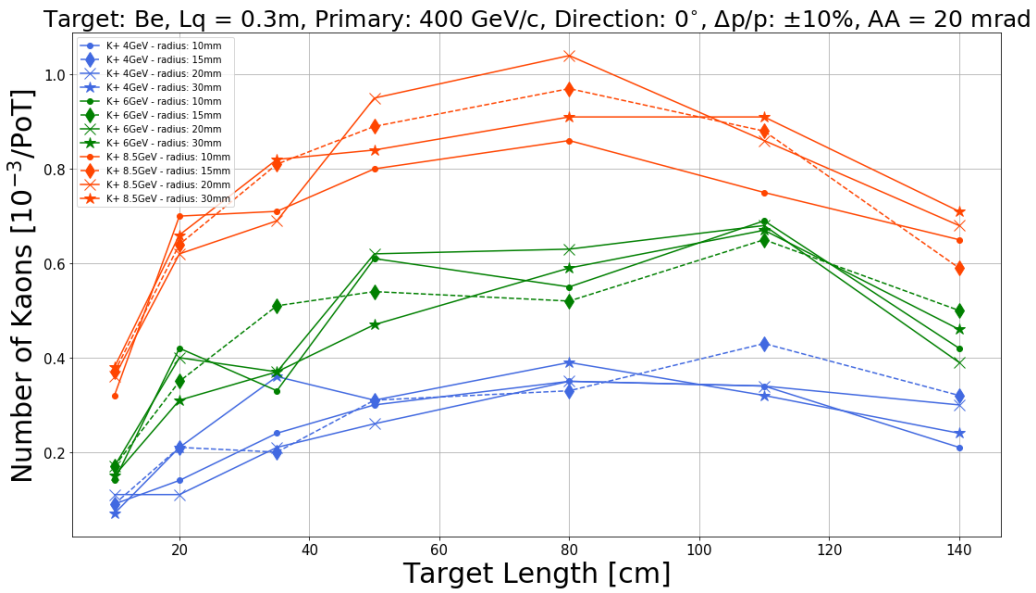

Figure 4.5: Same as Fig. 4.4, but for Beryllium targets.

4.3.3 Results

The results of the simulations are shown in Fig.4.4 and Fig.4.5. In summary, the graphite target seems to be the optimal choice, with a length of 70 mm. The radius does not seem to play a key role in the yield, therefore 30 mm is the final choice for the multi-momentum beamline application.

Chapter 5

The Multi-Momentum Beamline

In the framework of the present Ph.D. thesis, many different programs have been used to design and optimize the optics of the Multi-Momentum beamline. In this chapter, a brief description of these codes and their principle of operation is given. Finally, the final layout of the line is presented.

5.1 Software Used

This section is dedicated to a general description of the software used to design a beamline in all its stages.

5.1.1 Optics Software

There is multiple software designed for the realization of beamlines in terms of optics. The most used at CERN are described below.

TRANSPORT

Written for the first time in 1957, TRANSPORT is a program for first and second-order fitting capabilities for matrix multiplication intended for the design of static-magnetic beam transport systems.

The first version of TRANSPORT was written in the BALGOL language and later translated into FORTRAN. Within the program, a beamline is described as a sequence of elements that are not necessarily magnetic in addition to the beam parameters. The program crosses the beamline step by step, calculating the properties of the beam according to the matrix R

that describes the element crossed. TRANSPORT computes first or second-order matrices in a Taylor expansion around the central trajectory. For higher-order calculations that are ray-traced, the equations of motion must be directly integrated.

The main advantage of TRANSPORT is the ability to vary the physical parameters of the elements and impose constraints on the beam design. In this way, it is possible to make fits that optimize the parameters requested by the user.

5.1.2 Particle Tracking and Monte Carlo

Once a first beam line layout has been obtained, it is important to test its performance through a software capable of tracking particles emitted by a target passing through all the elements. In this way, it is possible to verify the possible interactions of the particles with the materials that make up the elements of the beamline and verify their validity.

Geant4

Geant4[68] is a toolkit designed to simulate the passage of particles in matter. Starting from the basic geometry provided, it is possible to build more complex structures that resemble real-life detectors. It can simulate complex hadronic processes and electromagnetic interactions thanks to the supplementary libraries that describe the physical processes. It was built and implemented in C ++ and has several applications in the world of physics, from particle physics, and aerospace engineering to medical applications.

G4Beamline

G4Beamline[66] is a simulation code based on the Geant4 toolkit. It was specifically developed for a matter-dominated beamline design. Thanks to the integrated physics libraries it can simulate decays and interactions with materials and trace the parameters of the particles at each position. The program provides elementary basic geometries to test the beamline composition. Subsequently, it is possible to define the elements that make up the beamline in detail and implement maps that describe the magnetic fields at fine elements through external files.

5.1.3 Radiation Studies

Once the rate of particles forming the signal of the experiment has been determined, it is essential to determine whether the elements used can withstand

the radiation load due to the non-interacting particles and the background halo. All elements of the beamline are subject to particle interaction, therefore background is generated by the interaction of secondary particles with the materials. It is also crucial to determine the radioactive activation of these elements to define safety parameters during the operation of the experiment.

FLUKA

FLUKA[69][64][65] is a simulation code designed for transport and interaction calculations with matter. As for the codes discussed previously, it finds numerous applications within the world of physics. It is capable of simulating electromagnetic particles up to thousands of TeV and hadrons up to 20 TeV. It is possible to realize complex geometries and various physical processes. The code is developed in Fortran 77 but does not require special programming skills thanks to the graphic interface created by CERN.

5.2 Multi-Momentum Beamline

ENUBET wants to extend the secondary energy studied from 8.5 GeV/c to 6 and 4 GeV/c. This range would allow serving other experiments besides DUNE, such as T2K and HyperK. Like the H4-VLE low-energy secondary beamline at the CERN Neutrino Platform [38], it imposes specific and stringent requirements to the geometry, global acceptance, collimation, and background reduction. As mentioned in the previous chapters, this beamline design is completely static. The decay tunnel imposes a stringent requirement on the rate of particles that reach the instrumentation. The pile-up problem requires that the particles have slow type extraction, hence the static design. This scheme allows having a shorter beamline thanks to the reduced size of the quadrupoles while preserving a satisfactory rate of the kaons, given their short decay length in the GeV/c scale. The following sections show the main layouts proposed for the line design together with their requirements.

5.2.1 Production Angle

The ENUBET signal is composed of the leptons emitted by the decay of the three-body $Ke3$ channel, as well as the two-body decays of the K^+ and π^+. It is important to mitigate the background as much as possible at the beamline level so that this does not subsequently contaminate the instrumentation and compromise the reconstruction of the events. A technique used to overcome

this problem is that of the production angle. The target is positioned at an angle to the opening of the first quadrupole. The positrons are emitted mostly in the forward direction and their production diminishes fast as a function of the production angle5.2. At the same time, the kaon rate at the momenta of interest also drops with the production angle, but not so fast as the positrons.

The primary beam, being very high energy (400 GeV/c), will not be affected by the field of quadrupoles and dipoles, therefore the production angle imposes a limit on the minimum length of the section that precedes the bending as well as a maximum possible angle. It is also necessary to respect a maximum length so that the primary beam does not hit the opening of one of the acceptance magnets of the beam. Part of the optimization studies of the Multi-Momentum beamline concerned the combination of these parameters to fix the acceptance stage and the production angle. This defined the overall length of the acceptance stage as well as the elements types, length, and drift spaces. A visualization with G4BeamLine is shown in Fig5.4 and Fig.5.5.

As can be seen from the diagram in Fig.5.1, even a tilt of 2.3° will cause an impact on the primary beam with the opening of the magnet.

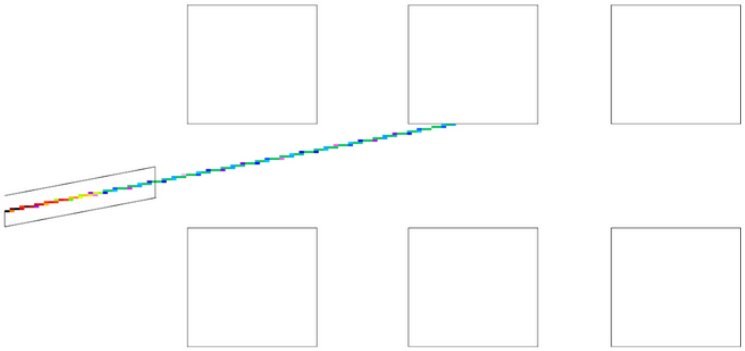

Figure 5.1: Scheme of the Target as tilted of 2.3° to the first quadrupole triplet.

Once the maximum angle for which the beam can be tilted has been identified, it is necessary to identify the angle for which the kaons/positron ratio is maximized. The advantage of a production angle lies not only in being able to easily eliminate the beam of primary protons. It allows for the suppression of a possible background source coming from the target itself caused by positrons with central momentum equal to that of the secondaries that compose the signal, which would therefore be transported up to the entrance to the decay tunnel. This relationship is represented in Fig.5.2.

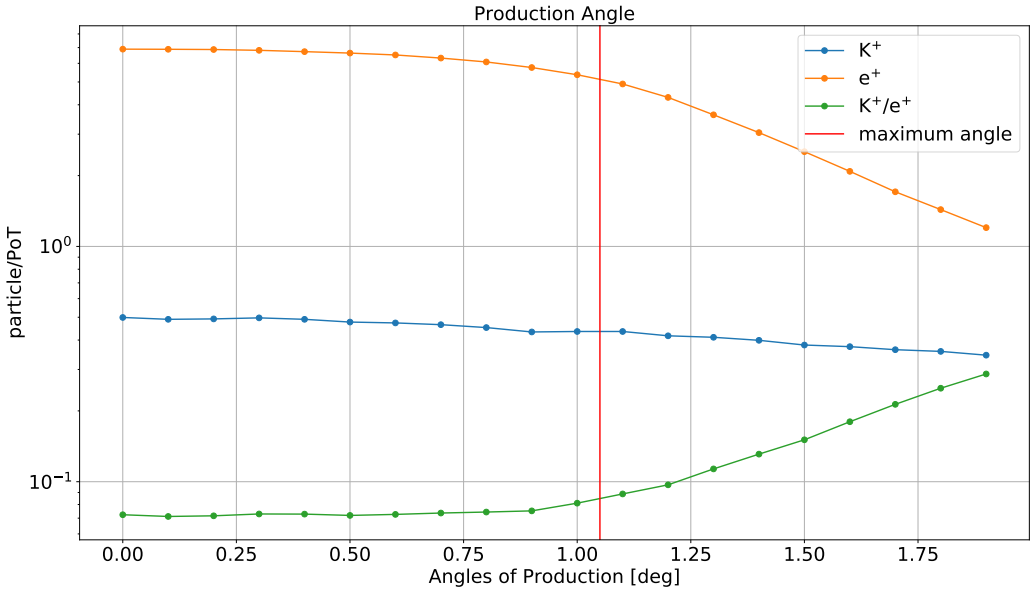

Figure 5.2: Number of particles after the first beam-line triplet ("acceptance stage"). It can be seen that the 1° production angle selected does not have a large impact on the produced kaons but a significant one on the electrons that constitute the background. The results are shown for 8.5±10% Gev/c.

Although a more substantial difference would be visible at greater angles, the geometric opening of the quadrupoles imposes a maximum production angle of $\sim 1°$, visible in the graphical representation in Fig. 5.3.

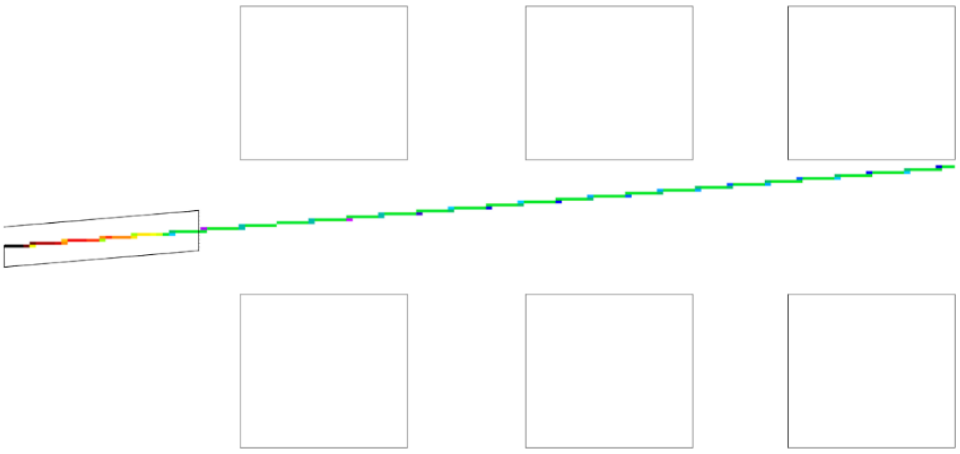

Figure 5.3: A FLUKA simulation showing the trajectory of the primary beam, when the production angle of 1 degree is implemented.

Using this production angle, it is possible to obtain a first skimming of the background formed by the positrons emitted by the target and to allow the primary beam of protons to escape without interacting with the magnets. However, as observed in Fig.5.3, the primary beam will be approaching very close to the aperture of the third quadrupole of the acceptance stage (QC of table5.1). This may imply higher temperatures or unacceptable losses. More studies are necessary to address this issue. A first solution to adopt could be the use of magnets with larger openings. However, magnets of this type are not currently available at CERN. For this reason, it will be necessary to investigate more in-depth concrete solutions that do not compromise the correct functioning of the magnets themselves due to the strong heat sustained during the run.

This matter will be further dealt with briefly in Sec.5.4 and future studies when approaching in-depth heat loads and radiation studies performed on the first triplet. As of now, The multi-momentum beam line plans to introduce a production angle of 8.72665 mrad (0.5°).

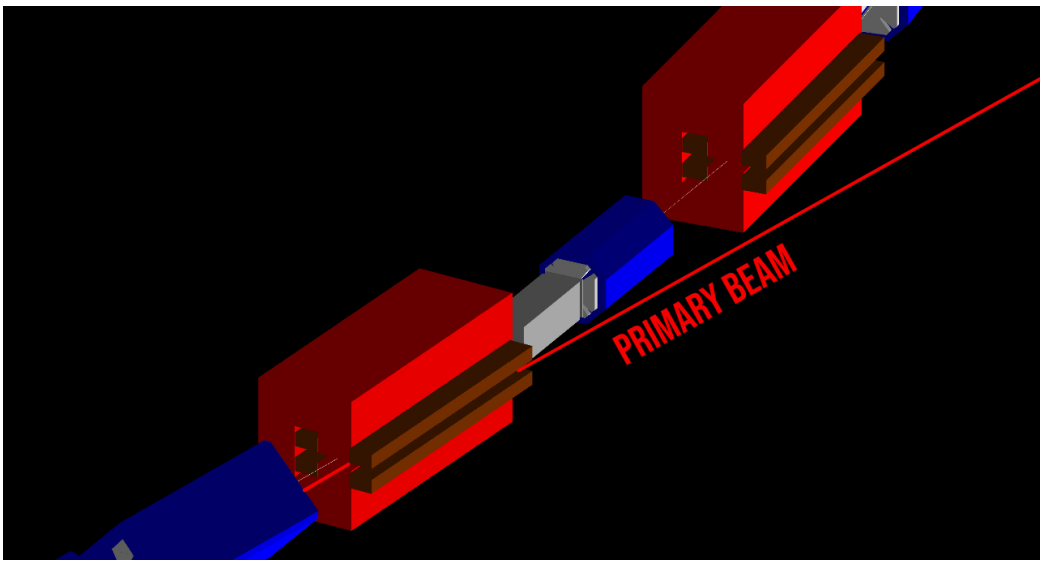

Figure 5.4: Visual G4BeamLine model of the Multi-Momentum line. The bending section of the newly designed line shows the escape of the primary beam through the lateral slit of the first bending magnet.

5.2.2 Optics Layouts

As described in Chapter3, the first step in designing a beamline is to identify the overall line requirements. In the case analyzed in this thesis, it is neces-

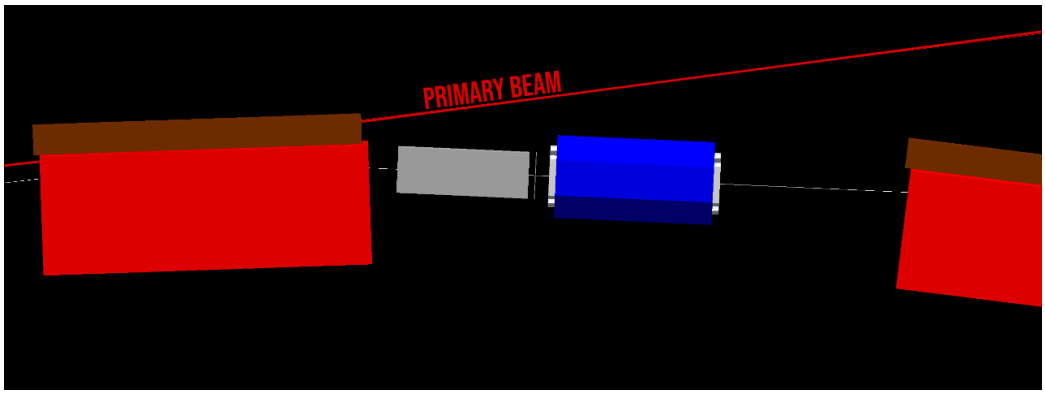

Figure 5.5: Detail of the bending section showing the primary beam avoids the collimator (the grey box) and the focusing quadrupole.

sary to create a beam of positively charged secondary mesons (K^+ and π^+) at 4, 6, and 8.5 GeV/c. This means that the beamline must be contained within a certain length to prevent the majority of kaons to decay before reaching the detector.

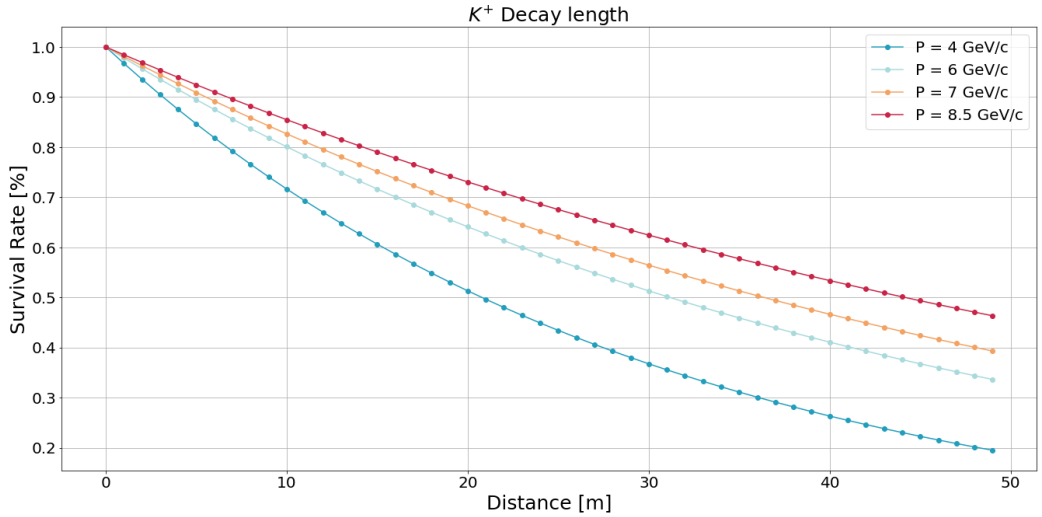

Figure 5.6: Kaons survival rate as a function of distance.

As shown in Fig. 5.6, any length within 30 m would allow for a survival rate above 50% to be maintained. Next, the beam needs to be focused at the center of the momentum selection section where the collimation takes place. Finally, it is required to be parallel so that the secondary beam does not hit the walls of the decay tunnel, but only the leptons that make up the signal are detected. The multi-momentum beam line constitutes three

optical 'stages': the acceptance section, the momentum selection stage, and the focusing section.

Acceptance Stage

When designing the acceptance section, it is necessary to identify the optimal number of magnets needed to meet the beamline requirements.

For simpler designs, it may be sufficient to use a quadrupole doublet to define the acceptance of the line from the target. However, concerning this design, it is necessary to have a minimum distance between the quadrupole and the central bending section so that the primary beam does not hit the opening of the focusing quadrupole. This minimum distance is imposed by the production angle.

Momentum Selection

In the middle of the momentum selection section, the beam is focused. At this point, it is possible to refine the selection of momentum of the secondary particles using a collimator. The opening of the jaws and the separation in units of momentum by milliradians allow us to define the momentum resolution of the secondary beam.

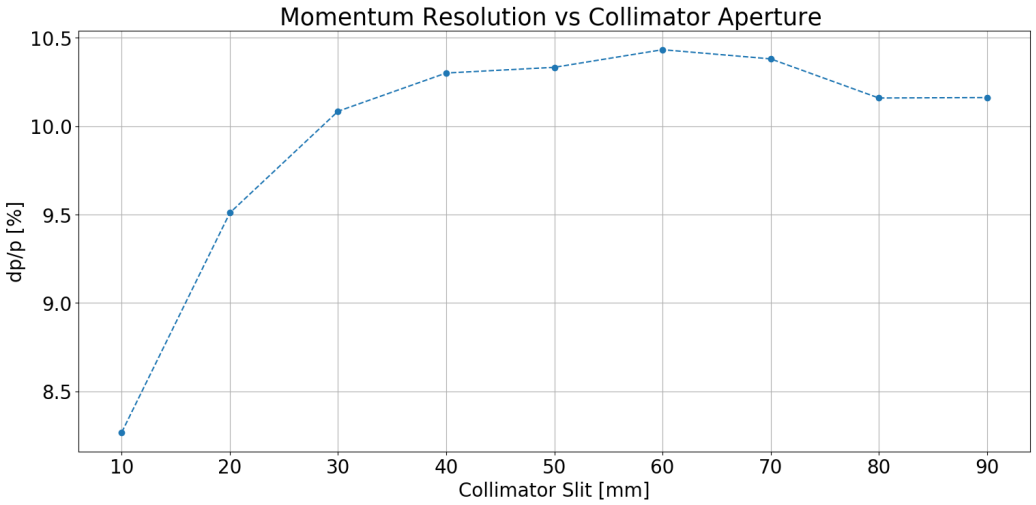

Figure 5.7: Momentum resolution of the desired beam as a function of the collimator aperture. As the selection is already performed in part from the previous magnetic elements, it's possible to observe a maximum in the resolution around 10%.

At this point, it is also possible to carry out the first step of the background reduction by placing a filter. To remove a large majority of positrons being created at the target, an absorber is placed in the middle of the momentum selection section. The beam at this position is brought at a double focus to minimize the multiple scattering. The absorber has a length equal to 1.43 radiation lengths but only 0.052 nuclear interaction lengths, thus being transparent to the hadronic component of the beam.

Final Focusing

Finally, the last stage treats the final beam shaping before reaching the detector. The beam is brought parallel in this last stage. In terms of optical conditions, the R22 and R44 terms are brought to zero. The R11 and R33 terms naturally grow (corresponding to the increasing transverse dimensions of the beam) but the overall beam size remains within the tunnel walls down. With the beam being parallel, only the decay products emitted at a wide angle (as the positrons by the Ke3 channel) reach the instrumented wall of the tunnel, While the hadrons and other particles such as positrons produced at the target and traveling along with the kaons continue straight and therefore do not interact with the instrumented walls of the tunnel. In general, the parallelity of the beam is ensured with a triplet or a quadruplet of quadrupole magnets. In this design the quadruplet option was chosen since the overall length of the beamline remains below 30m (5.1 and allows for a better result given the maximum field strengths provided by the magnets.

5.2.3 Magnets

As already introduced in section 5.1, G4Beamline provides the user with basic geometries with which it is possible to assemble and make the first analysis of their beamline. This tool allows to set the main design parameters and have a first estimate of the transported particle rate. The “generic” bends or quadrupoles of G4BL are a very good approximation for simulating the good field region of the magnets, however, the field shape is idealized and fully homogeneous. At the same time, the iron yoke is not magnetized and therefore the charged particles like muons that do not stop inside the iron yoke of the elements, are following straight trajectories. A fundamental part of the work of this thesis concerned the implementation of a more realistic geometry along with dedicated field maps that best represent the magnet models chosen for the beamline layout.

The magnetic elements used are currently already in use at other beamlines at CERN, with known dimensions and properties.

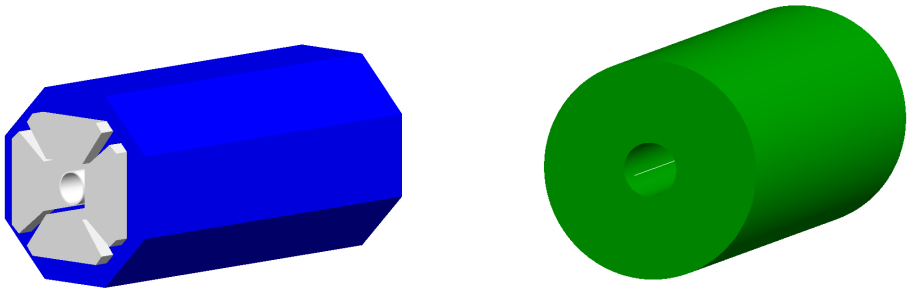

(a) detailed QPL geometry (b) standard quadrupole

Figure 5.8: Different G4BeamLine models of quadrupole magnets. The first one, (a) represents the detailed geometry implementation of a QPL magnet, while (b) shows the simple geometry given by G4Beamline to simulate any quadrupole magnet with variable length and aperture.

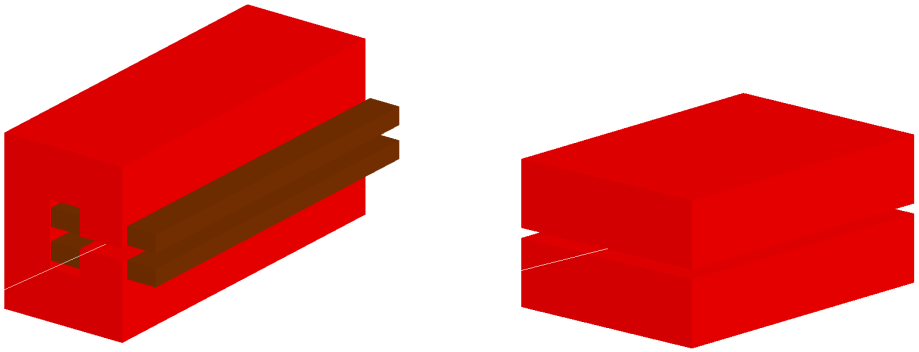

(a) detailed MCB geometry (b) standard dipole magnet

Figure 5.9: As per the quadrupoles, side-by-side dipole magnets. The first one, (a) represents the detailed geometry implementation of an MCB magnet, while (b) shows the generic bending magnet with an infinite horizontal slit and variable aperture.

5.2.4 Field maps

After building the detailed models of the magnets, a field map needs to be calculated and mapped correctly on the corresponding geometry. G4Beamline accepts input files that accurately describe the components of the magnetic field B_x, B_y, and B_z. This is a complex operation, since the more points where the finite element field is calculated, the more precise the interpolation and recreation of the field lines acting on the particle passing through

the magnet will be. However, it is necessary to take into account the granularity of the calculated points also in terms of the computational time that the program takes in the calculation of each simulation. For this reason, several "maps" has been created which describe the intensity of the magnetic field at the points x, y, and z for every single magnet.

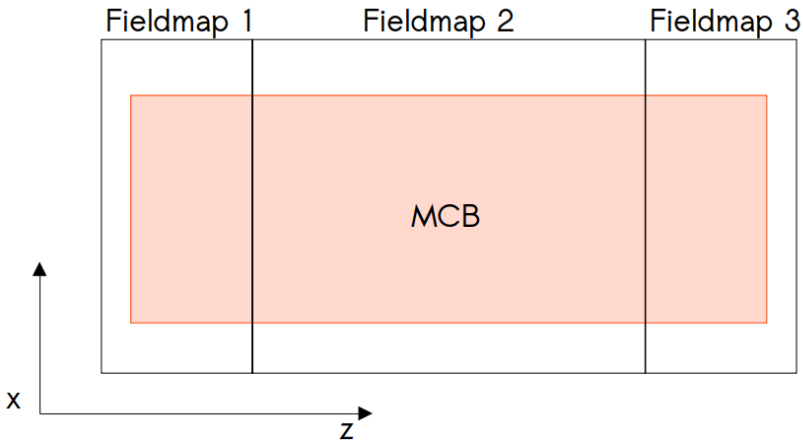

Figure 5.10: Profile along z of the MCB magnet with the separate field maps scheme.

In particular, after several studies, a significant effect has emerged from the edges of the magnets at both the entrance and exit. The shape of the coils and the iron that makes up the core of the magnet exerts a field kick on the particles entering and leaving the magnet, as shown in Fig.5.11

Adopting multiple input files as field maps for each magnet allows to use of different granularity along the z direction and investigates edge effects. Using a higher granularity it is possible to localize and minimize the edge effects that would be interpolated with the adjacent points.

Once all the field maps have been correctly implemented, it is important to compare the behavior of the beam using the standard 'generic' magnets and the detailed ones with the field maps. For this reason, a standard-type magnet has been implemented, with a magnetic field of G4Beamline but with an infinite horizontal opening to allow the primary beam to escape. Next, the main beam parameters are compared between the realistic magnet MCB, the infinite aperture magnet just described, called MCB-std, and the simple magnet of G4Beamline MBPL.

As seen from Fig. 5.12, the realistic magnet, with the aforementioned calculated field maps, presents substantial differences in the vertical plane. These distribution tail substructures may be due to the edge effects discussed

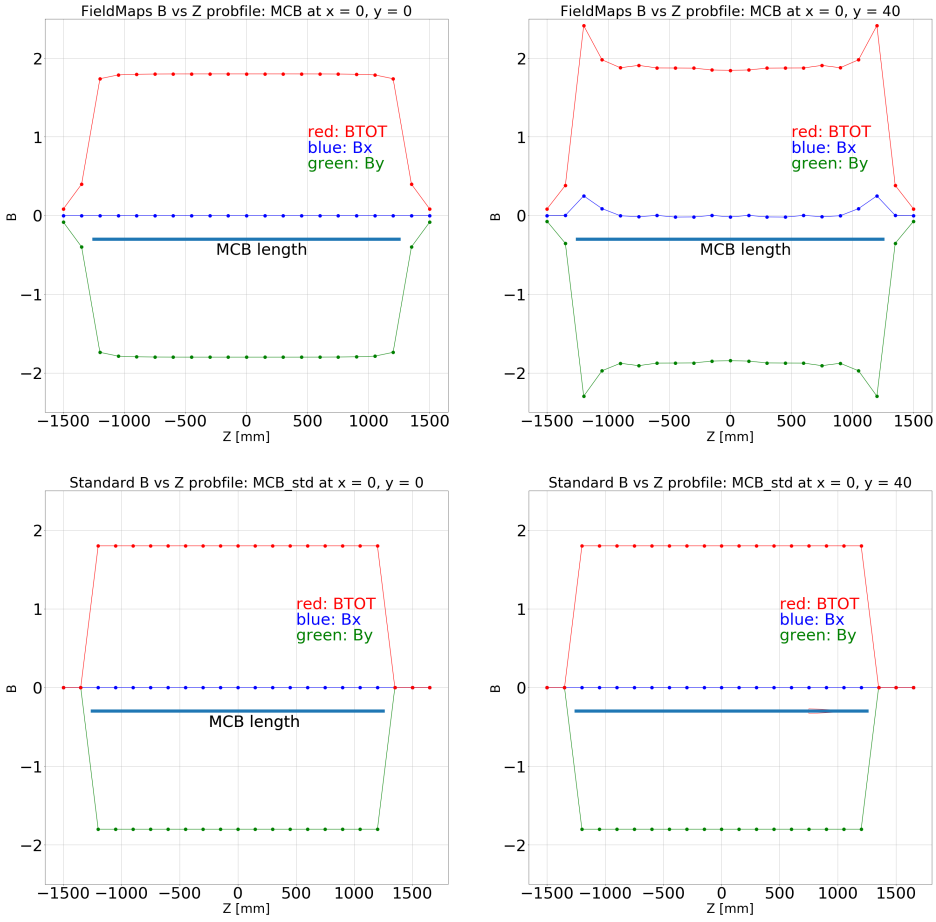

Figure 5.11: Profile along z of the MCB magnet in both the standard and the detailed versions. The first two plots show the field calculated at the center and the aperture of the magnet for the standard version. The third and fourth show the same for the detailed version. The kick that emerges at the aperture of the magnet is in correspondence with the edges.

earlier and particles escaping, it could also be given by the in-homogeneity of the field at the aperture or simply differences in the field values present in the magnet yokes. However, it does not seem to affect the momentum selection of particles. Finally, to verify the effect of the realistic geometries and the implemented field maps, the results obtained for the transport of a secondary beam in the three momenta (4, 6, and 8.5 GeV/c) of interest need to be compared. In Fig.5.13, it is shown that the differences in the shape of the beam throughout the line due to the different geometries and field maps, do not have a significant effect on the momenta of Kaons reaching the tagger.

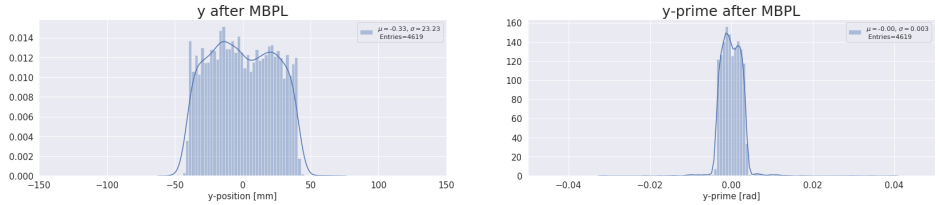

(a) MBPL

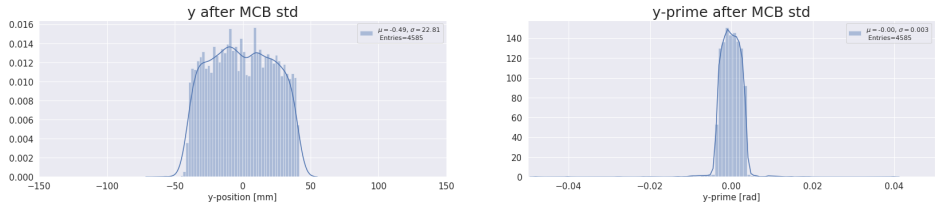

(b) MCB-std

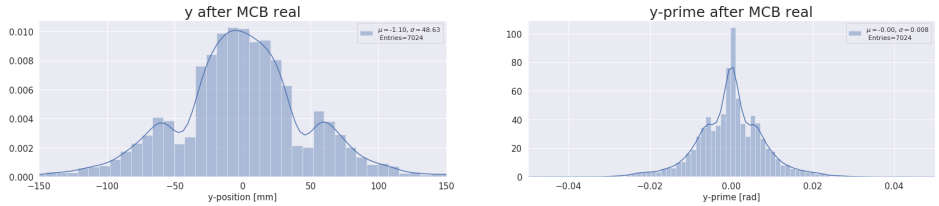

(c) MCB

Figure 5.12: Beam profiles showing x, y, x-prime, y-prime, and total momentum distribution of particles exiting the bending magnets.

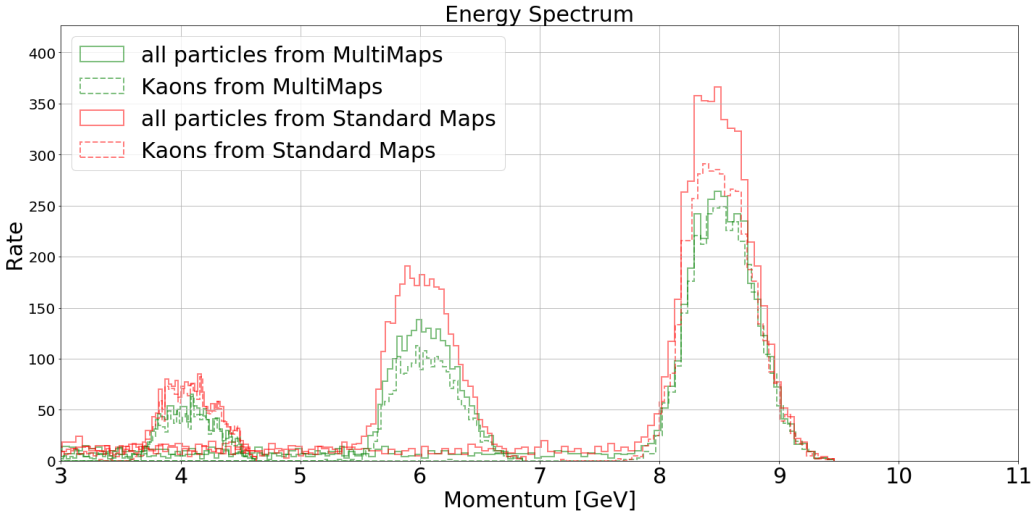

Figure 5.13: "Multi-Momentum" beamline layout in G4Beamline.

5.3 Chosen Layout of the proposed beamline

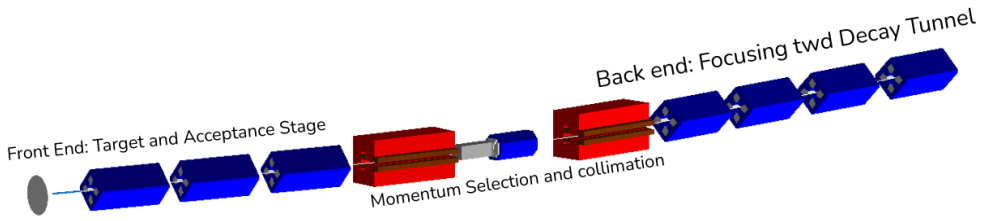

Figure 5.14: Final beamline layout implemented in G4Beamline.

Here is summarized the general final layout of the "Multi-Momentum Beamline" as seen in Fig.5.14. A triplet of QPL-type quadrupoles with a radius of 100 mm, defines the acceptance of the line. Subsequently, the momentum selection sector is composed of two MCB-type magnets characterized by a lateral opening that allows the non-interacting 400 GeV/c primary beams to come out without creating secondary targets with a total deflection of 18.18°. In between these, a field lens is placed to allow proper dispersion recombination. Finally, a quadruplet of quadrupoles carries the parallel beam inside the decay tunnel. The field lens plays an interesting role in phase space acceptance. Two line designs are proposed with each a different field lens: one with a QFL-type quadrupole, the other with a QPL-type magnet. The first one allows for a more parallel beam, as seen in Fig.5.15 and Fig.5.16, while the second has a greater acceptance in the horizontal plane as shown in Fig.5.17 and Fig.5.18.

The beam is fully contained inside the decay tunnel for both options, the first layout scheme is the chosen candidate, offering a more parallel beam.

The following table 5.1 shows the main values of the magnets used with values based on the CERN's handout[70].

Once established the basic layout, optimization studies were performed involving computational algorithms to maximize the performance of the line and the overall particle acceptance. An example of this study showing the comparison of the triplet of the designated line and the optimized version is shown in Tab.5.2.

The results obtained from this study show a compatible phase space acceptance. However, although the optimized version has greater acceptance, these parameters would not allow some ulterior physical constraints such as the production angle imposed at the target level to minimize the positron contamination. The reduced drifts of the optimized version (see Tab.5.2) would

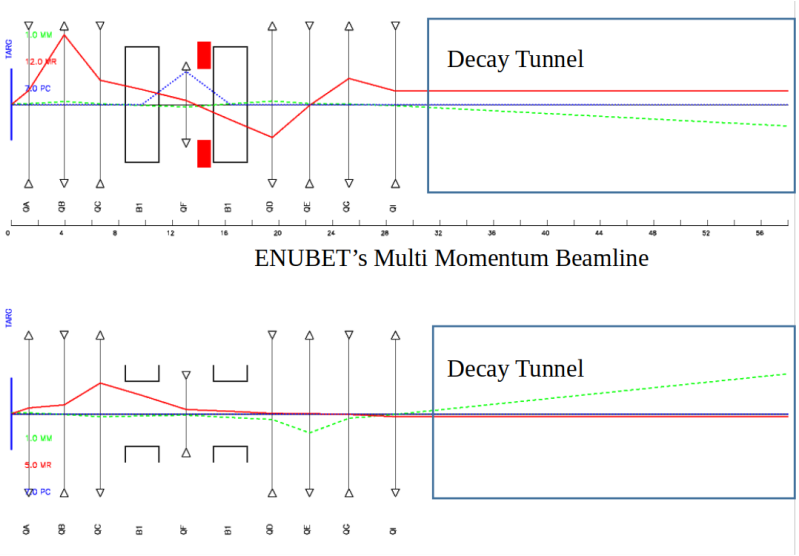

Figure 5.15: First Multi-Momentum Beamline optics showing horizontal (top) and vertical (bottom) planes. Each line is a graphic representation of the R-matrix parameters: the green lines represent the cosine-like rays, the red line the angular rays and the blue line corresponds to the dispersive rays. The beam is tuned to be parallel to the decay tunnel in both planes.

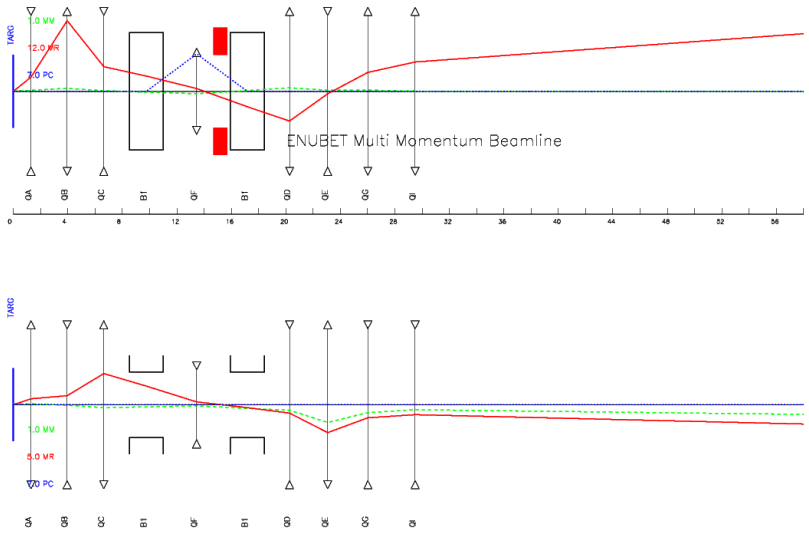

Figure 5.16: Second Multi-Momentum Beamline optics. Each line is a graphic representation of the R-matrix parameters for the first layout.

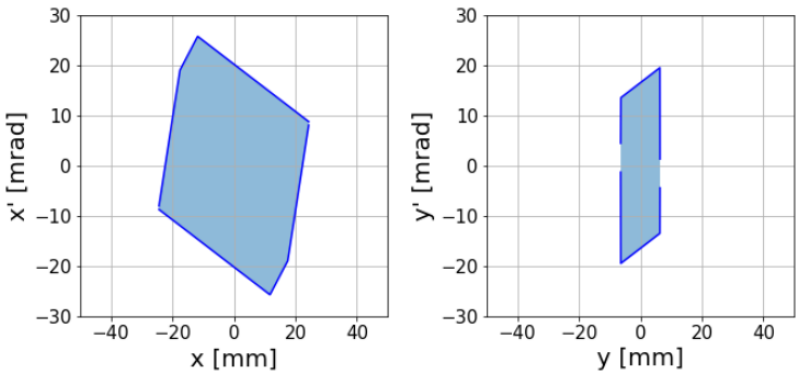

Figure 5.17: Total Acceptance Phase Space of the first line in both horizontal and vertical planes. Every particle emitted by the target that falls within these areas will be accepted and transported at the end of the line.

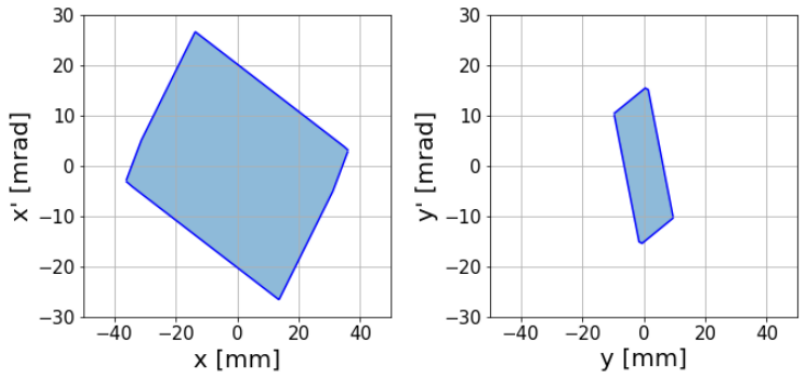

Figure 5.18: Total Acceptance Phase Space of the line in both horizontal and vertical planes.

not let the primary beam escape from the line without interfering with the focusing magnet placed in the center of the bending section. Therefore, the final optics parameters follow the first version's results.

Finally, the advantages of this line are the reduced length and the use of pre-existing magnets, allowing a low cost in its construction and limiting the technological difficulties that a newly manufactured magnet could face. The adoption of a production angle limits the acceptance of mesons emitted forward by the target, the total rate that reaches the decay tunnel is then also limited and consequently so is the rate of neutrinos at the far detector. However, this expedient allows us to have a cleaner signal and to easily separate the primary beam from the secondary beam.

Table 5.1: Summary table of the magnets used in the newly proposed Multi Momentum beamline.

Name	**Type**	**Length** [m]	**Maximum field strength**[T,Tm^{-1}]	**Aperture** radius [mm]	**Distance Target** [m]
QA	QPL	2.0	10.5	100	2.300
QB	QPL	2.0	10.5	100	4.950
QC	QPL	2.0	10.5	100	7.635
MCB1	MCB	2.5	1.8	80	11.005
QF	QFL	1.2	18.9	50	14.460
MCB2	MCB	2.5	1.8	80	18.415
QD	QPL	2.0	10.5	100	21.285
QE	QPL	2.0	10.5	100	24.070
QG	QPL	2.0	10.5	100	27.020
QI	QPL	2.0	10.5	100	30.490

Table 5.2: Comparison of the first triplet parameters calculated first with TRANSPORT and then through an optimization algorithm.

Parameters	**Version 1**	**Optimized**
Strengths		
k1	-0.358	-0.2559
k2	0.346	0.347
k3	-0.234	-0.233
Drifts [m]		
d1	0.300	0.300
d2	0.650	0.640
d3	0.870	0.870
Acceptance Area [mm*mrad]	1612	1625

5.4 FLUKA Studies

This section briefly addresses the subject of maintenance and the possible sources of deterioration of the magnets. The beam-induced heating can be a source of degradation of the magnets and can even hamper significantly the operation. The magnets taken into consideration, as already mentioned, are of the QPL type. The conductors are made of electrolytic copper, with a resistivity of less than 1.76×10^{-8} ohm ·m at 20°C [71]. The magnet winding consists of four solid block molded coils, one for each pole. Even without any

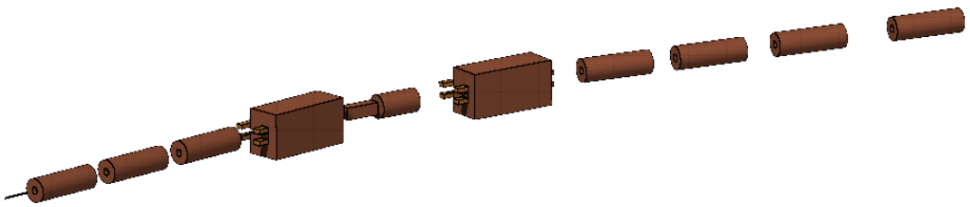

Figure 5.19: Multi Momentum Beamline model implemented in FLUKA

beam, the temperature gradients generated by water-cooling and magnetic forces impose mechanical stress on the coils. For this reason, the coils can reach a maximum temperature of 40°, in this way the thermal expansion between the conductors that make up the coil would be between 1 and 2 mm if they could move freely. The temperature at which the water is maintained is around 10°C. This underlines the importance of water isolation of the magnets to avoid short circuits caused by condensation. Next, it is necessary to take into account the beam-induced heating caused by the primary and secondary beams during the operation.

The materials used for insulation must be resistant to damage from nuclear radiation. For this reason, the permitted materials are based on fiberglass.

In the framework of this thesis, a first analysis was done concerning the adiabatic temperature increase that a 400 GeV/c, slowly extracted proton beam would have on the target and the various magnetic elements of the line.

Fig.5.19 presents the beamline layout as implemented in FLUKA.

More specifically, this thesis it's presented the heat increase in the first triplet, as this is where the primary beam interacts the most with the beamline's elements. From these plots, it is possible to see how the greatest impact occurs at the entrance of the magnet.

Respectively, Fig.5.20, 5.21, and 5.22 shows the maximum temperature increase with the "Central CUT" FLUKA representation on the right, and the averaged temperature increase over the Y axis on the left for all three quadrupoles individually. The temperature increase is of the order of 1-5K per primary spill on target. However, these estimates were made in a completely adiabatic environment, without therefore considering the thermal dissipation and the cooling systems required by the operation of the magnets. Future studies will be conducted to investigate how water-cooling and dissipation affect the magnets' materials.

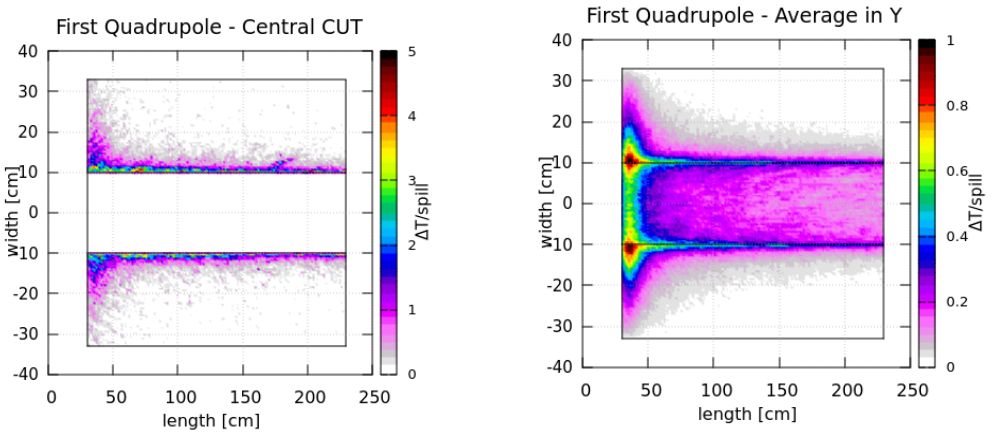

(a) Central cut (b) Average in Y

Figure 5.20

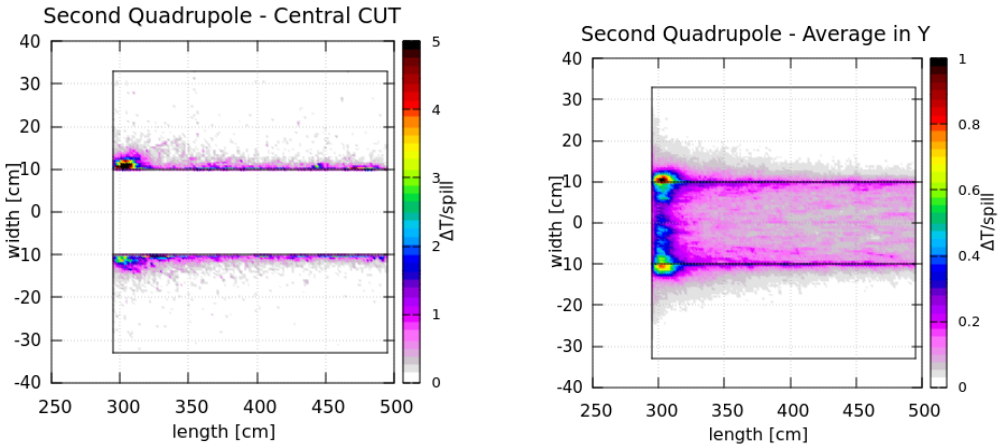

(a) Central cut (b) Average in Y

Figure 5.21

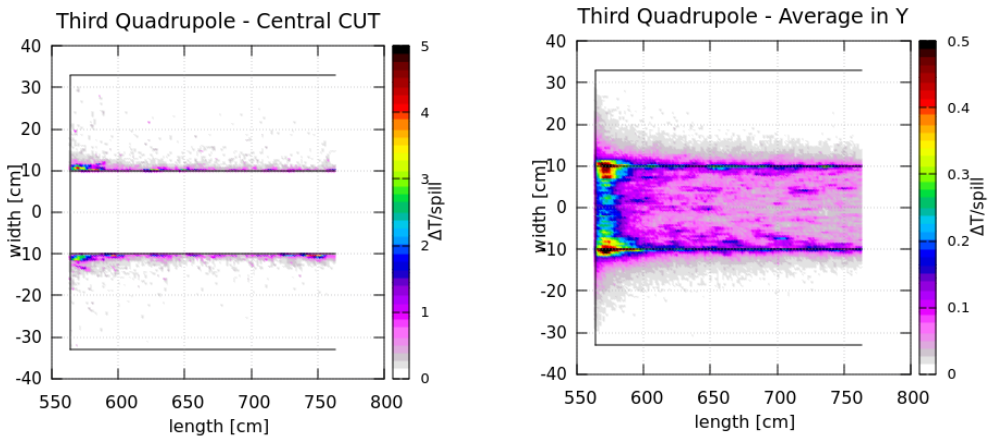

(a) Central cut (b) Average in Y

Figure 5.22: Heat increase at the acceptance triplet of the line as expressed in terms of Kelvin per primary spill (4×10^{13} protons over 2 s) with a central cut in X and averaged over Y along all Z for all three quadrupoles.

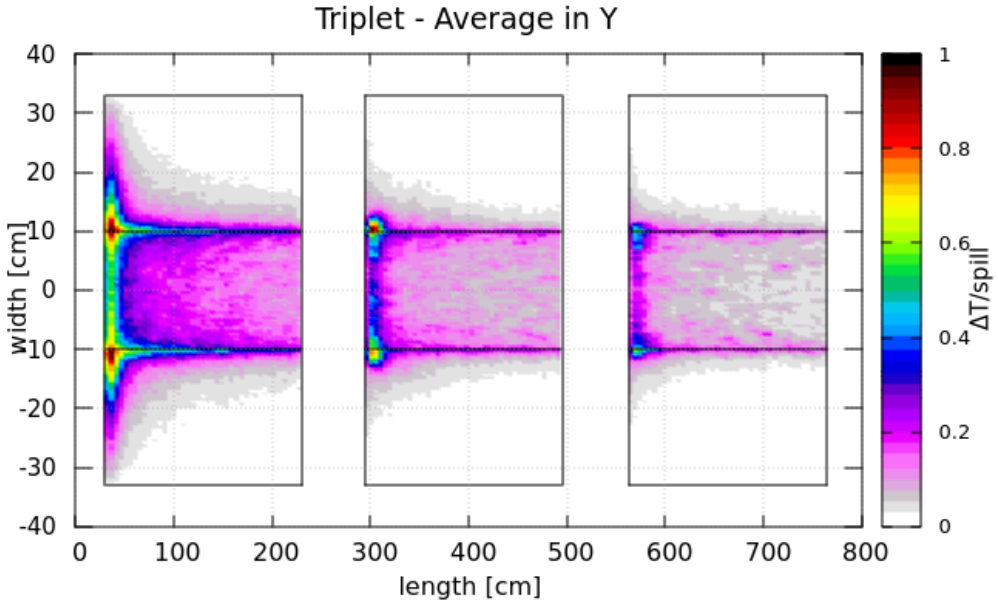

Figure 5.23: Schematic representation of the first triplet as implemented in FLUKA. It is here represented the heat increase in terms of Kelvin per proton spill.

Chapter 6

Expected Performance of the MMB

In this chapter, it's discussed the expected rates and the overall performances of the Multi-Momentum beamline. One of the biggest challenges for the study and validity of this model undoubtedly concerns the computational time taken by the simulations. The interactions of a high intensity proton beam with heavy materials, is computationally quite intense. Transporting all these secondaries with enough statistics downstream is by far the most "computationally expensive" task. To evaluate more realistically the performance of the line, it is advisable to build a shielding system that protects the surrounding environment and the detector entrance from all particles that escape or interact with the magnets.

6.1 Shielding

As previously mentioned, the interaction of the primary and secondary beams with the elements of the beamline can be a source of background for the final signal. Even the decay of the main beam particles can affect the quality of the signal and of the secondary beam that is carried by the beam line. While the latter cannot be mechanically limited and stopped, it is nevertheless possible to limit the particles produced by decays and interactions. Just as the users within an experimental area are protected from the radiation produced by the interactions of the beam with the instrumentation through the use of high-density material (high Z), so too the beam and the magnetic elements themselves are shielded to limit the background transported to the detector.

The shielding studies were carried out through the use of G4Beamline to study the effect of positioning on the rate of particles reaching the tagger.

The background figure of merit is made up of any particle outside the central energy range (8.5, 6, and 4 GeV/c ±10%).

One of the main sources of background particles is the interaction of the beam with the third quadrupole, caused by the angle of production. The sigma in x and y is such that interactions of the beam with the magnet edges are non-negligible even if the core of the beam does not touch the walls of the magnet. Two other important background sources are composed of the interaction of the beam with the focusing lens (quadrupoles) placed between the two dipole magnets and unwanted secondary particles produced in the target itself. These particles can be transported along the beamline and reach the detectors inside the decay tunnel.

The location of the shieldings in the beamline layout is shown in Fig. 6.1.

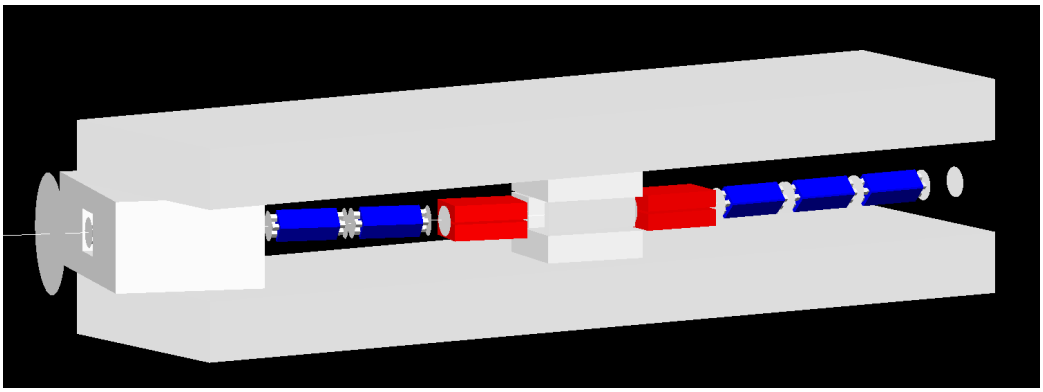

Figure 6.1: Schematics of the beamline layout with the shielding surrounding the key elements that produce the largest source of background at the tagger entrance.

This configuration has been optimized in the 8.5 GeV/c set-up where there is a low energy peak of off-momentum transported particles around 4 GeV/c. Without appropriate shielding, this background originating from the target would be transported down to the tagger. The discrimination effect of this peak can be seen in Fig. 6.2, in which it's possible to observe a zoom-in around that energy with and without shielding. This study has been carried out using pions as the main signal to reduce the computational time.

6.2 Transmission Studies

The efficiency check of a beamline takes place in several steps. It is essential to verify that there are no substantial losses of the central beam at any point

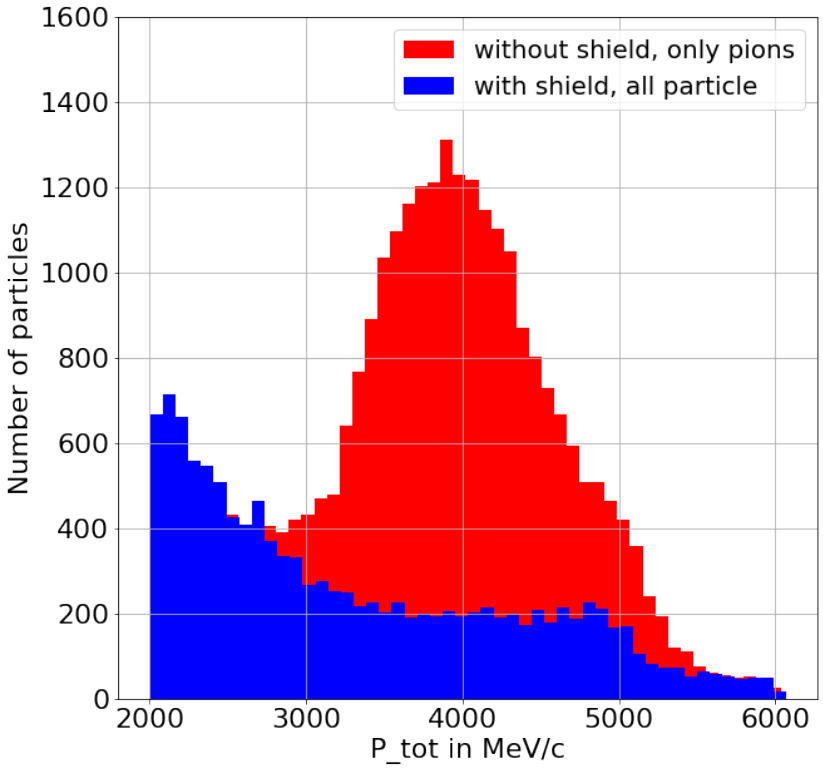

Figure 6.2: Zoom-in of the largest background contribution to the momentum spectrum: the 4 GeV/c peak generated at the target and at the focusing lens.

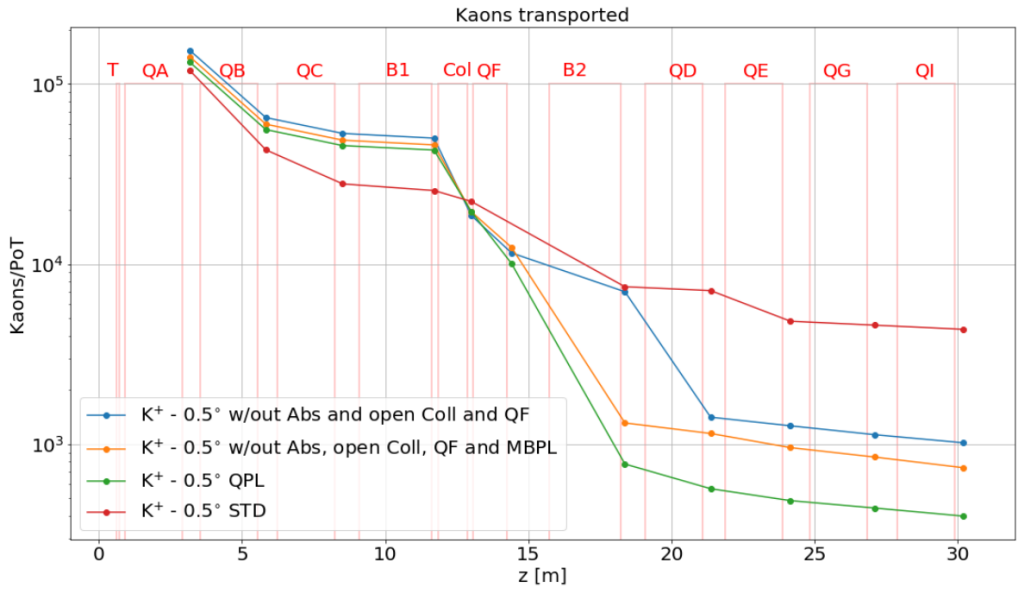

Figure 6.3: Transport of kaons through the line at each element. Every color represents a different layout of the line where either the absorber is removed, the collimator is open, or the field maps are used.

of the line. It is also important to determine which is the best positioning of the so-called "passive" elements of the line so that the signal is maximized.

Fig.6.3 describes the impact on the signal of the use of absorbers, the opening of collimators, and the use of field maps. More specifically, it is shown the transport efficiency of the central beam at all points of the beam-line: the acceptance triplet, the momentum selection section composed of the dipoles and the focusing lens, and finally the quadruplet for the final focusing. The largest effects are visible after the removal of the absorber, the opening of the collimators, and the use (or not) of field maps. While the field maps perform very efficiently in the triplet, it is possible to see a marked loss in the transport of particles from the focusing lens to the second dipole. Observing the size of the beam at the exit of this magnet, it is possible to notice an evident deformation of the beam in the vertical plane which does not allow the entrance of the particles within the geometric acceptance of the dipole.

The dipole has an opening of 80 mm in the vertical plane. Even if it were possible to increase it, there would remain a defocusing problem in the y-axis that would also propagate in the quadruplet, which has a maximum aperture of 200 mm immediately after the dipole. The issue due to the field maps seen in Fig.6.4(a) is not present in Fig.6.4(b). Therefore, an anomaly might be

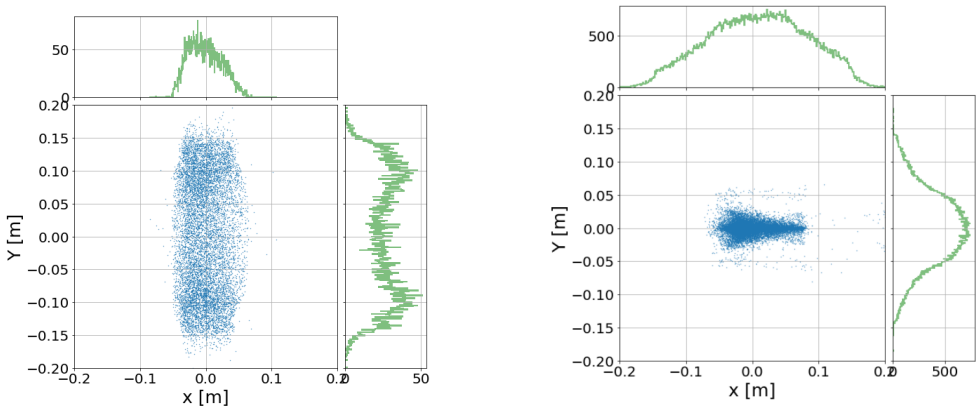

(a) QF with field map (b) standard QF

Figure 6.4: Beam profile in X-Y after the QF field lens placed between the dipoles.

present inside the code of the simulation of the quadruple field maps. For this reason, the performance studies carried out on the number of total particles transported by the beamline were made with standard magnets, while the field map implementation will be completed in a further study.

6.3 The entrance of the decay tunnel

To evaluate the performance of the beamline, the particles that reach the entrance of the instrumented decay tunnel (the lepton tagger), are counted. It is important to ensure that the beam is completely contained inside the tunnel down to its end and that the beam envelope does not cross the walls instrumented with the calorimeter and the $t0$ layer. The contamination of the walls would compromise the reconstruction of the signal produced by the decay of pions and kaons. As already mentioned in the instrumentation chapter, the tagger is a 40 m-long tunnel with a 1 m radius. To simulate the rate of particles entering the tunnel, a "Virtual Detector" has been positioned, i.e. a disk of zero thickness and empty material, with a radius of 1 m. The Virtual Detector records the spectrum of particles that reach the tunnel instrumentation.

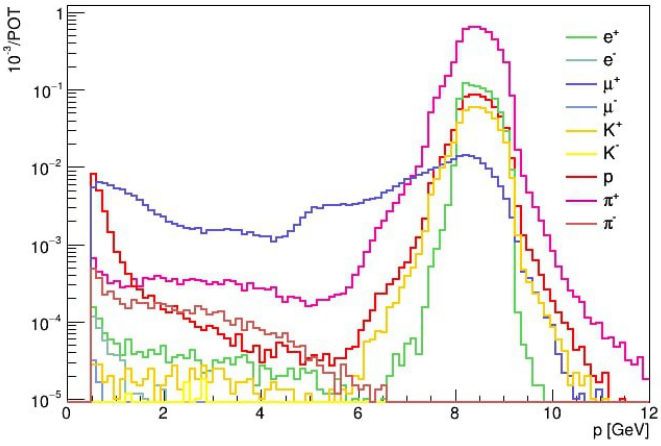

Figure 6.5: Logaritmic momentum spectrum at the tagger entrance from the 8.5 GeV/c baseline beamline

6.4 Neutrino Detector

As already mentioned, ENUBET monitors the decay of the K and π mesons, which produce muon and electron neutrinos with forward emission. While the decay-charged leptons are detected within the decay tunnel, the neutrinos interact within a large mass neutrino detector located approximately 50 m from the end of the tagger. The detailed response of the neutrino detector is outside the scope of this work but studies performed by the ENUBET Collaboration have mostly focused on liquid argon TPCs like ProtoDUNE-SP. To study the performance of the multi-momentum beamline, it is not enough to stop at the study of the momentum spectra of secondary particles arriving at the tagger. Downstream of the tagger, a block of concrete and iron was positioned to simulate a "hadron dump", followed by ground and finally a "Virtual Detector" that simulates the neutrino detector. This Virtual Detector is, again, a void disc of zero thickness with a radius of 6 m. Furthermore, a simplified version of the proton dump was simulated. This component is on-axis with the primary beam and absorbs it completely. The spectra of the particles reaching the neutrino detector for all three beamline configurations (central momentum at 8.5, 6, and 4 GeV/c) are shown in Fig.6.11.

The plots shown in Fig.6.10 and Fig.6.11 show the spectrum of neutrinos weighted by the cross-section together with other particles reaching the neutrino detector. The spectra are normalized by the number of protons impinging on the target. The first spectrum is obtained through the MMB, while the second is originated by the ENUBET baseline beamline. The sim-

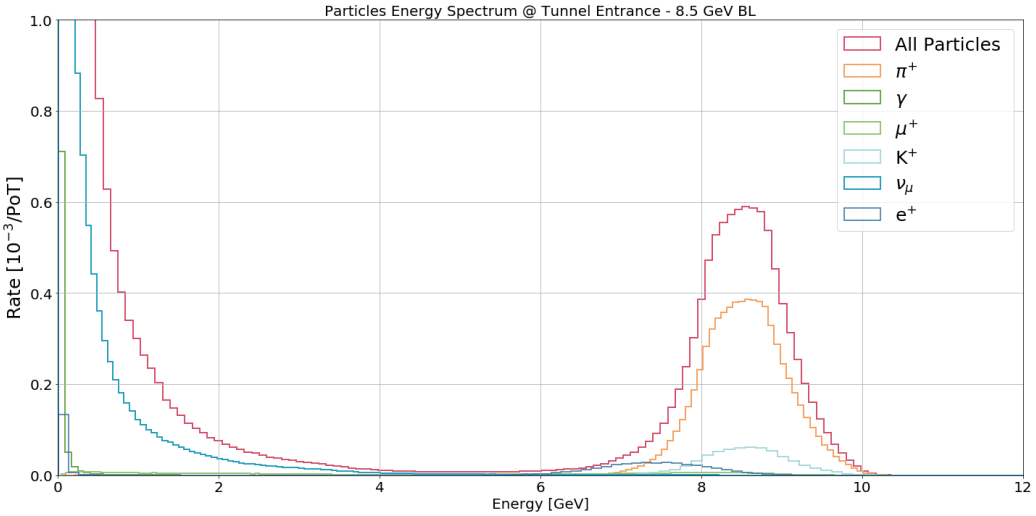

Figure 6.6: Linear momentum spectrum at the tagger entrance from the 8.5 GeV/c beamline

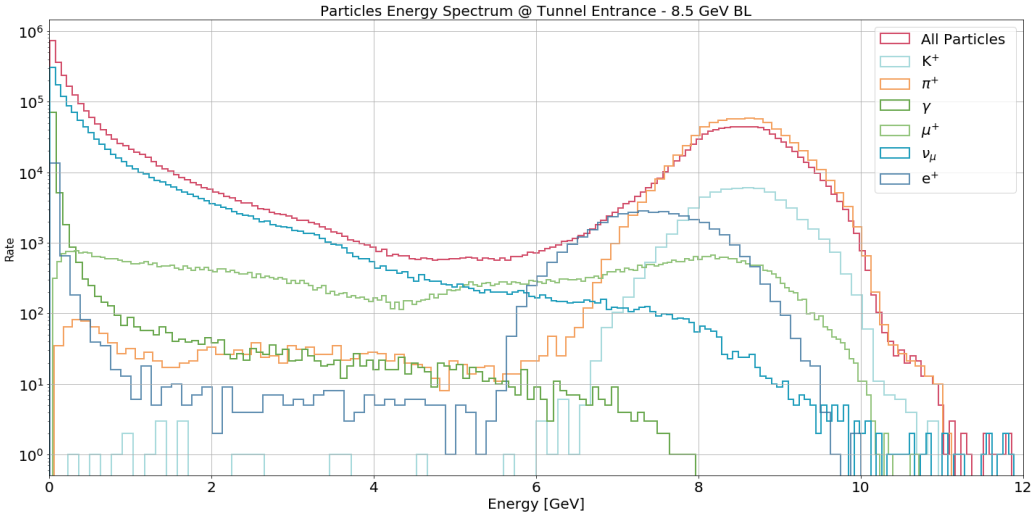

Figure 6.7: Logaritmic momentum spectrum at the tagger entrance from the 8.5 GeV/c beamline

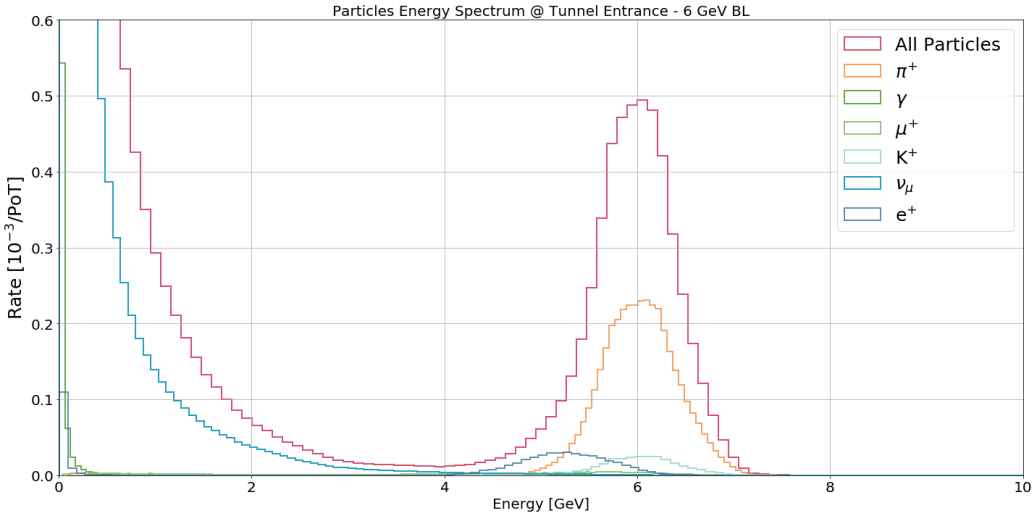

Figure 6.8: Linear momentum spectrum at the tagger entrance from the 6 GeV/c beamline

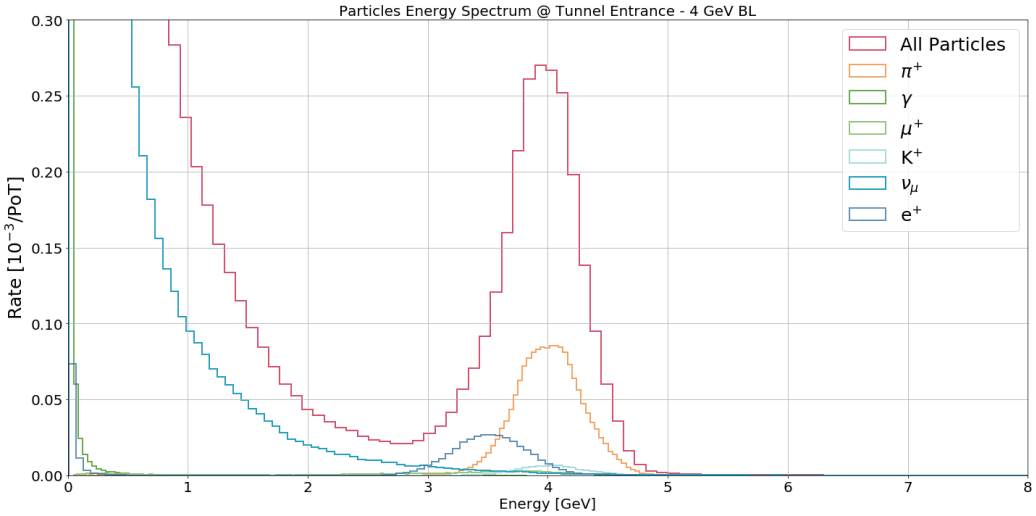

Figure 6.9: Linear momentum spectrum at the tagger entrance from the 4 GeV/c beamline

Table 6.1: Particle rates at tagger entrance for 8.5 for both beamline proposals, and 6 and 4 GeV/c for the MMB configurations.

Particles [10^{-3}] PoT	**8.5 GeV/c**	**6 GeV/c**	**4 GeV/c**
MMB			
$\mathbf{K^+}$	0.68	0.28	0.08
π^+	7.9	4.1	1.7
Baseline Beamline			
$\mathbf{K^+}$	0.36	/	/
π^+	3.97	/	/

ulation of the baseline design was carried out with an energy cut at 500 MeV/c. The cross-section weighted flux is thus proportional to the events observed by the neutrino detector at the end of the ENUBET data taking.

In the case of the baseline design, the muon neutrino spectrum has a sharper separation between the neutrino peaks produced by K and π. Conversely, the electron neutrino spectrum is more prominent in the 8.5 GeV/c Multi-Momentum Beamline configuration. The corresponding plots produced for the MMB configuration at 6 and 4 GeV/c are shown in Fig.6.12 and Fig.6.13.

As a result of the narrow band beam, the contributions of ν_μ coming from K^+ decays and from π^+ are well separated. The first is placed in the high-energy region of the spectrum up to 8 GeV, while the second spans the lower-energy region. In conclusion, the MMB shows a kaon and pion yield at the entrance of the tagger that is about twice the baseline ENUBET beamline. By employing the runs at 4 and 6 GeV/c, the MMB provides the degree of tunability needed to enhance the number of observed neutrino interactions at the detector in the 1 GeV region both for ν_e and ν_μ.

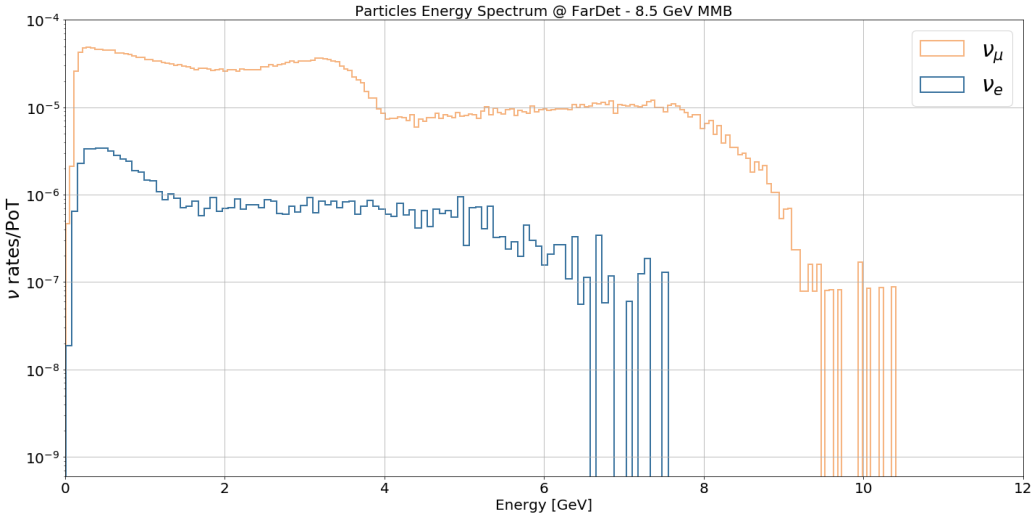

Figure 6.10: Logaritmic momentum spectrum of the neutrino reaching the neutrino detector for the 8.5 GeV/c multi momentum beamline. The spectra are weighted by the cross section and energy.

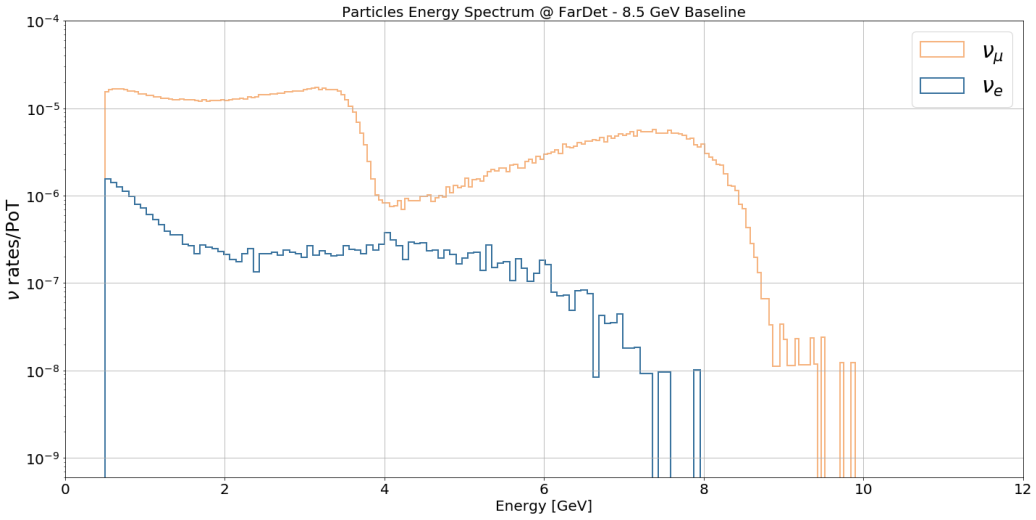

Figure 6.11: Logaritmic momentum spectrum of the neutrinos reaching the neutrino detector for the 8.5 GeV/c baseline option. The spectra are weighted by the cross section and energy.

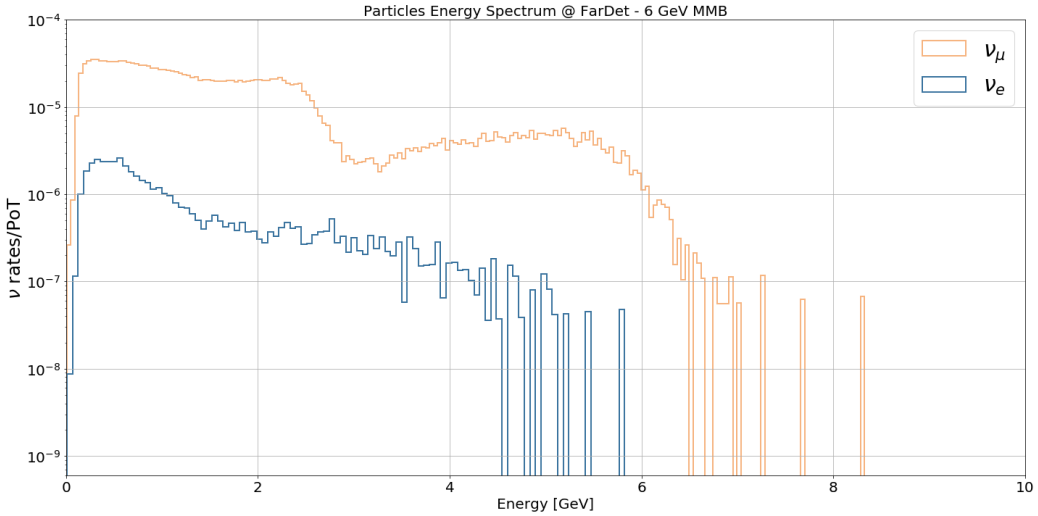

Figure 6.12: Logaritmic momentum spectrum of the neutrinos reaching the detector for the 6 GeV/c beamline

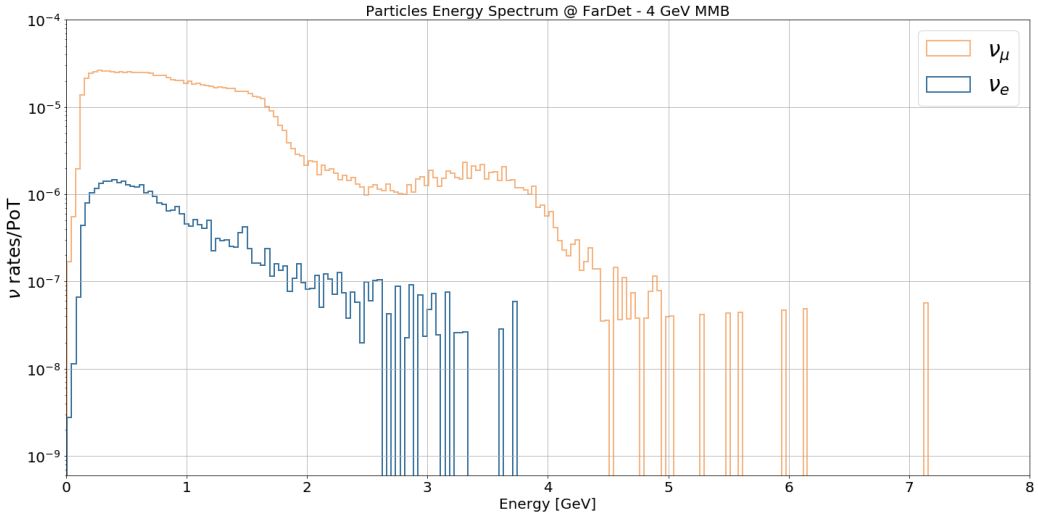

Figure 6.13: Logaritmic momentum spectrum of the neutrinos reaching the detector for the 4 GeV/c beamline

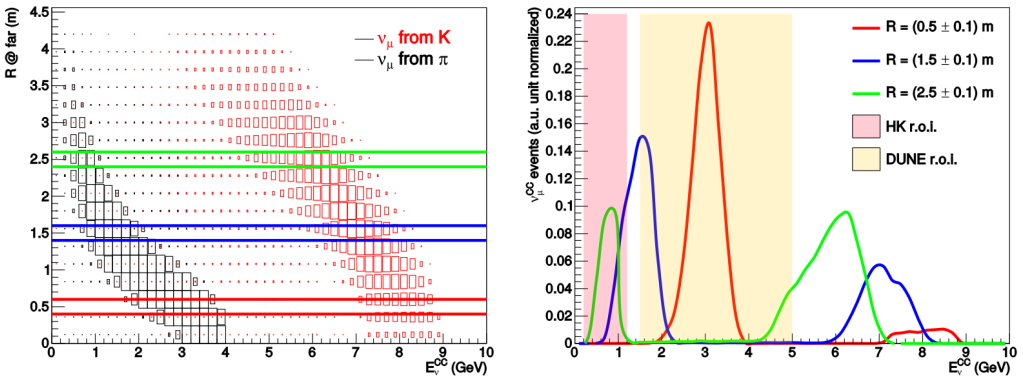

Figure 6.14: Left plot: correlation between the energy of ν_μCC events at the neutrino detector (horizontal axis) and the radial distance from the beam axis (vertical axis) in the baseline ENUBET beamline. Right plot: momentum spectrum of the neutrinos at different radial ranges.

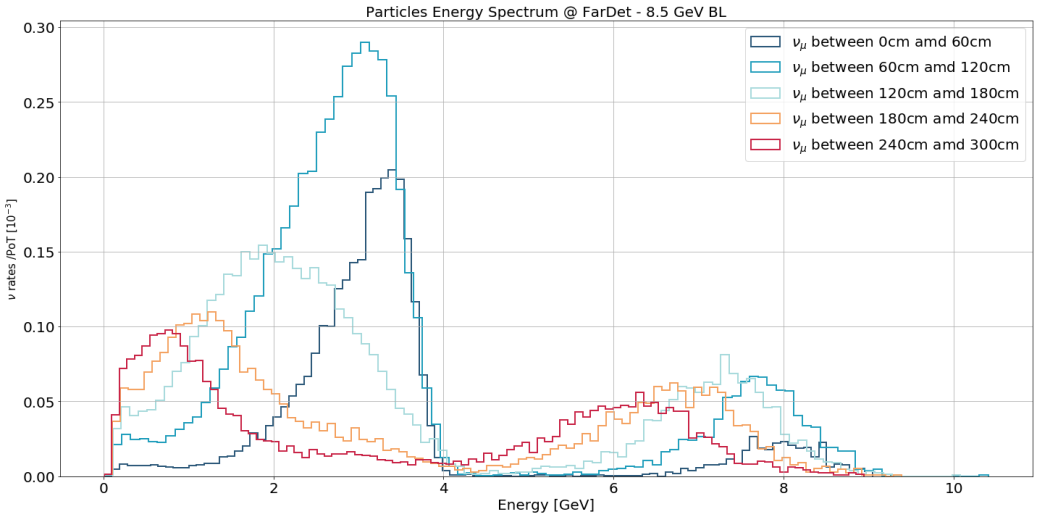

Figure 6.15: Linear momentum spectrum of the ν_μ reaching the neutrino detector for the 8.5 GeV/c beamline at different radial ranges in the MMB.

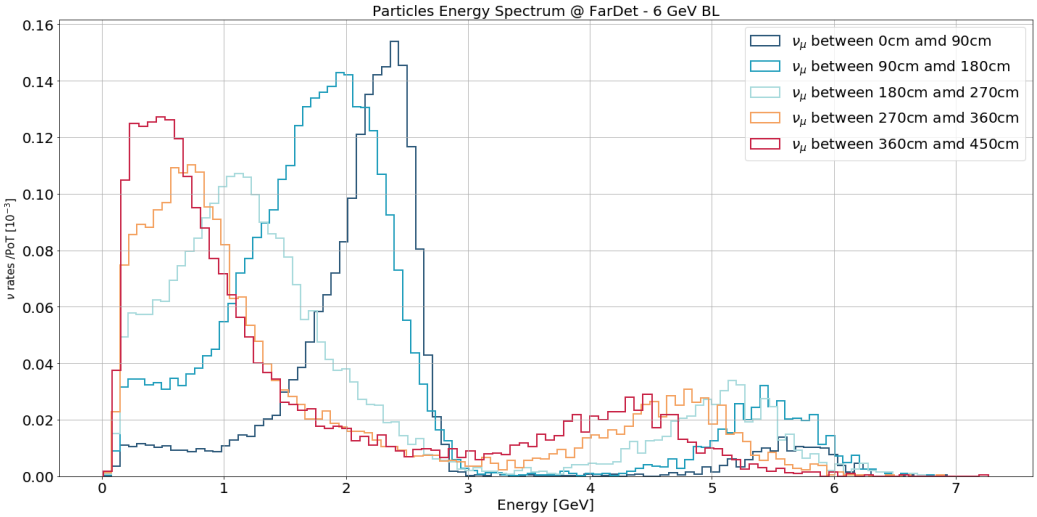

Figure 6.16: Linear momentum spectrum of the ν_μCC events (i.e. cross-section weighted flux) reaching the neutrino detector for the 6 GeV/c beamline at different radial ranges.

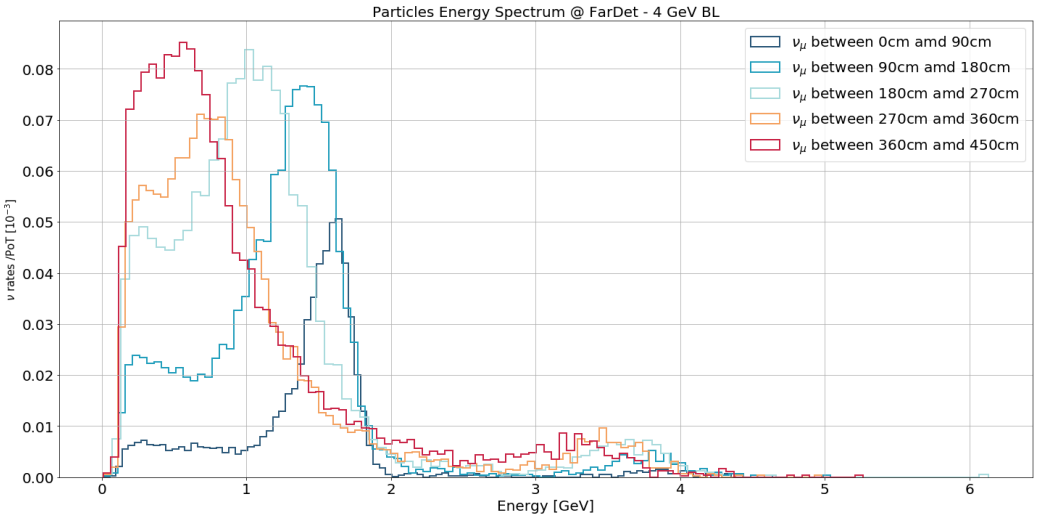

Figure 6.17: Linear momentum spectrum of the ν_μCC events (i.e. cross-section weighted flux) reaching the neutrino detector for the 4 GeV/c beamline at different radial ranges.

Chapter 7

Instrumentation

When it comes to instrumentation for monitored neutrino beams, it is important to distinguish between beam monitoring with conventional advanced diagnostics and the choice of the detectors for the decay tunnel. In this chapter, both aspects are introduced. First, the preliminary considerations made so far for the monitoring instrumentation of the beamline itself and possible future studies are elaborated. Then, the instrumentation of the decay volume needed for the experiment to tag the positrons emitted by the decays of the kaons is described.

7.1 Beamline Instrumentation

When designing a beamline, it is necessary to monitor the production of secondaries emitted from the target, as well as the primaries impinging on the target. Having a precise knowledge of the flux also impacts the precision of measurement of the neutrinos arriving at the far detector. Particle accelerators provide several diagnostic systems to monitor the beam based on the beam intensity, extraction pattern, and particle energy. The main detector systems for beam diagnostics can be found in the extensive review on monitored neutrino beams [72] and [73].

Regarding the ENUBET Multi Momentum Beamline, it is necessary to take into account the beam characteristics in order to consider the appropriate instrumentation for the beamline. These considerations are important both for the commissioning period in which it is necessary to monitor the primary beam and for the run phase in which it is necessary to keep the beam of transported secondaries under control. Magnetic spectrometers based on tracking detectors around bending magnets can provide a direct measurement of particle momentum[74], and other detectors can provide particle identifi-

cation using Time Of Flight measurements to identify heavy particles on an event-by-event basis. The detectors chosen for this project should sustain an expected rate of $\sim 10^{11}$ kaons for a few s spills. The possibility of tracking is thus directly linked to the possibility of performing a slow extraction because a faster extraction would increase the rate to a level that cannot be accomplished by current and near-future technologies.

The transverse dimension of potential trackers must take into account the dimensions of the beam, measured to be $\sim 5 \times 5\,\mathrm{cm}^2$. A future study will thoroughly investigate which are the best candidates for detectors that can go to instrument the beam line. At the moment, the "Giga-Trackers"[75], silicon-detectors already used within the NA62 collaboration[76], are under consideration. Considering that the material budget must be kept to a minimum, Giga trackers have 0.5% of X_0, which makes them a good candidate.

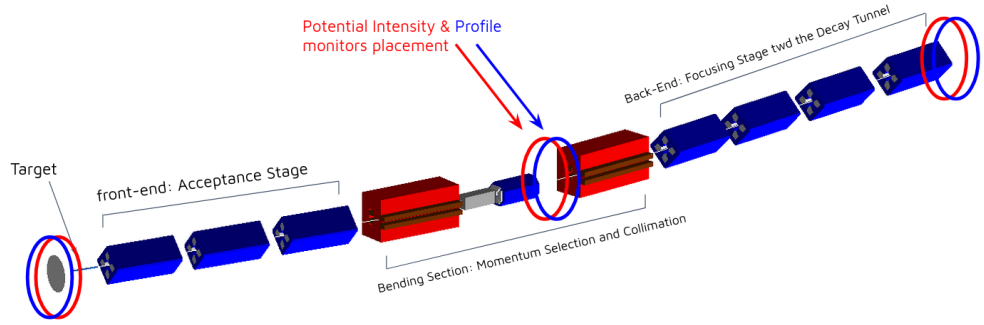

Figure 7.1: Beamline Layout with possible instrumentation placements. Potential intensity (in red) and profile (blue) monitors

.

As a byproduct of this thesis work on the multi-momentum beamline, tracking at single-particle level is currently pursued by ENUBET in the framework of the NuTech project funded by the Italian Ministry of Research and by the NuTAG initiative.

7.2 The ENUBET Decay Tunnel

This section presents the general design of the detector instrumenting the decay tunnel as well as the "ENUBINO" prototype tested in November 2021 at the CERN East Area.

7.2.1 The ENUBET Calorimeter

ENUBET's proposed detector is a longitudinally segmented calorimeter, whose aim is to tag few-GeV positrons produced in the K_{e3} decay. The granularity of the calorimeter was optimized in 2017 by the ENUBET collaboration. As discussed in Chap. 2, each module (UCM) is paired with an additional inner low-density detector needed for further e/π^0 separation and timing: the t_0-layer. Particle identification is achieved by taking into consideration the development of electromagnetic and hadronic showers and the energy deposition inside the calorimeter. Monte Carlo simulations show evidence that the optimal longitudinal segmentation for e^+/π^+ separation in ENUBET is ~ 10 cm ($4X_0$ - radiation lengths), which reduces the charged pions misidentification probability to less than 3%. The baseline option uses plastic scintillators that offer an energy resolution appropriate for the needs of ENUBET, short recovery time ($\sim$10 ns), and reduced costs[77].

In the original ENUBET design, the basic elements of the segmented calorimeter are the Ultra Compact Module (UCM), consisting of a stack of steel tiles (1.5 cm thick) interleaved with plastic scintillator tiles (0.5 cm thick), both having a 3×3 cm^2 cross-section. Positron-initiated electromagnetic showers are fully contained inside ~ 2 UCM, unlike the more penetrating pion-induced showers.

The UCM axis is placed parallel to the beam so that particles impinging on the calorimeter with an angle below 100 mrad can be detected. The modules of the calorimeter are placed inside the decay pipe and assembled in cylindrical layers. Between 2017 and 2021, the ENUBET groups performed a comprehensive R&D to identify the optimal detector technology. Iron-plastic scintillator detectors, whose light is read by wavelength shifter fibers have been proven to be cost-effective and suitable for the needs of ENUBET. The most cost-effective solution for light readout after transport in the WLS fiber is the use of Silicon Photomultipliers (SiPMs). SiPMs, however, are sensitive to non-ionizing radiation doses. ENUBET performed both irradiation tests and a FLUKA-based assessment of ionizing and non-ionizing doses. These studies finally brought to the "lateral readout design", which is described in the next session.

Lateral scintillation light readout calorimeter (LRP)

Shashlik calorimeters have been widely used in collider and fixed-target experiments. As a consequence of the increasing development of silicon-based photosensors, the shashlik technology evolved toward a new readout scheme that combines the classical shashlik readout with the new photosensors. This

Figure 7.2: Lateral scintillation light readout prototype

technique was pioneered in 2015-2016 by the SCENTT R&D at INFN. The ENUBET collaboration was firstly considered in 2016 segmented shashlik modules embedding silicon photomultipliers in the bulk of the calorimeter. The design was safe even accounting for the neutron irradiation for the entire duration of the ENUBET data taking (10^{11} 1-MeV-eq neutrons/cm^2) but sensitivity to single photoelectron was lost and the safety margin for retaining sensitivity to mips after irradiation was less than a factor of two. As a consequence, ENUBET decided to drop this solution and move the SiPMs far from the calorimeter to improve the irradiation safety margin by a factor of 20 and ensure detector reliability for a much longer duration of the data-taking. In 2018, ENUBET designed the prototype tested in this thesis, which is less compact than the shashlik solution but provides a safer read-out after neutron irradiation.

This type of compact module employs a lateral light readout so that the SiPMs are not embedded in the calorimeter bulk, thus not exposed to radiation. Light is collected from both sides of each scintillator tile by gluing the WLS fiber to the scintillator inside a suitable groove machined on the plastic. Then, fibers from the same UCM are bundled into a single SiPM reading in groups of 10 at a distance of about 30 cm from the bulk of the calorimeter. This scheme allows easier access for maintenance or replacement purposes. Furthermore, the lateral scheme is mechanically simpler both for the machining of the calorimeter component and for the fiber-to-SiPM coupling. The prototype was successfully tested in May 2018 at the CERN T9 beamline. The final design, however, needed to be engineered to be scalable to the entire tunnel. This engineering phase was carried out in 2021-22 and brought to the realization of a small-scale prototype (ENUBINO) and the

ENUBET Demonstrator.

7.2.2 ENUBINO

Figure 7.3: Latest prototype "ENUBINO" tested in Nov. 2021

ENUBINO played a fundamental role in view of the construction of the Demonstrator because it validated the light efficiency and readout employing the same mechanical solutions (fiber routing, scintillator machining, SiPM coupling to the fibers, etc.) used at large scale.

The main differences reside in the geometry of the elements that make up the individual UCMs, simplifying their assembly and limiting possible cracking of the optical fibers. The absorbers were replaced with iron blocks, which run vertically crossing the UCM. The scintillators are divided into three columns housing two optical fibers per tile. The interior of the grooves of the scintillator tiles was painted with a TiO_2 based varnish to prevent the fibers from collecting light from adjacent tiles (optical crosstalk).

Simulated response of the Calorimeter

In order to understand and eventually improve the performance of the calorimeter, a detailed Monte-Carlo simulation was developed in the framework of this thesis using the Geant 4.10.0.4 software[68]. The Geant4 simulated calorimeter geometry consists of a single UCM placed in the vacuum with different beam positions to replicate the test beam displacements. Each scintillator tile is built as a rectangular solid volume that measures 5.2 mm along the beam direction (x) and has a 30×30 cross-section in the transverse plane (y,z), and is composed of a generic plastic material of density 1.03 g/cm^3 (C_7H_8OSi), whose nuclear properties are identical to the ENUBINO scintil-

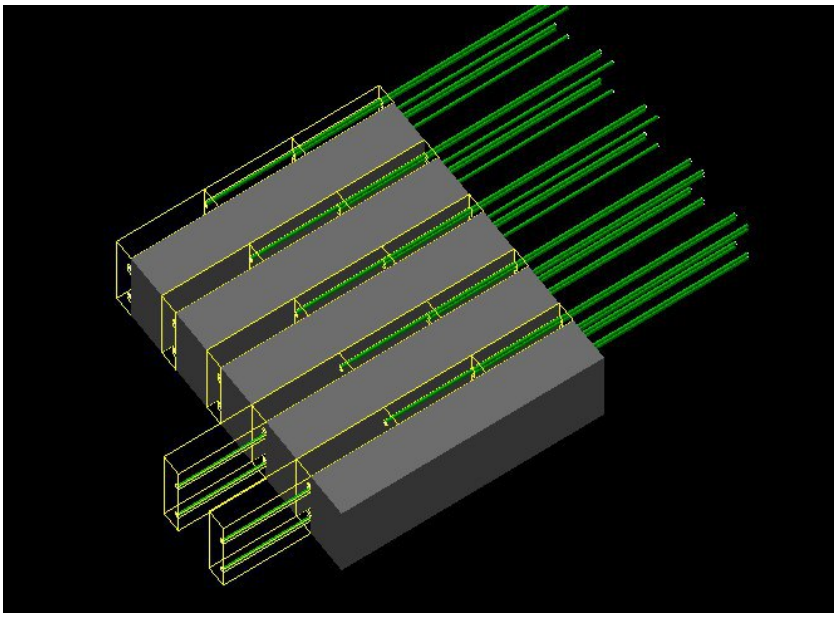

Figure 7.4: Latest prototype "ENUBINO" tested in Nov. 2021. The beam impinges on the calorimeter hitting face-front the first absorber tile.

lator. Each tile box is grooved on the face front with hollow tubs to host the fibers that will be placed inside to avoid overlaps.

Each UCM is composed of three different types of tiles depending on the radial position. The absorbers are instead modeled by a simple parallelepiped. The simulation was thus aimed at providing a realistic estimate of shower development inside the prototype and, then, the relative response among tiles.

Experimental validation

ENUBINO was tested with a dedicated beam in November 2021. During the data collection campaign, the prototype was tested with a secondary beam (mainly protons at 15 GeV/c). ENUBINO was positioned at different points transversely to the beam, to test the response of the modules. The simulated version of the calorimeter was tested with three types of beams at 15 GeV/c: electrons, muons, and protons. Each bundle is elliptical with a distribution such that $\sigma_x = 1$ cm and $\sigma_y = 3\,\text{cm}$, and the angular distribution has $\sigma_{xang} = 0.018611\,\text{rad}$ and $\sigma_{yang} = 0.02333\,\text{rad}$. The envelope used in the simulation reproduces the beam envelope in the proximity of the prototype. Each simulation run had a number of events equal to the particles collected in each experimental run. In the simulation, a uniform momentum distribution

was assumed since the momentum bite at T9 is negligible compared with the sensitivity of the prototype.

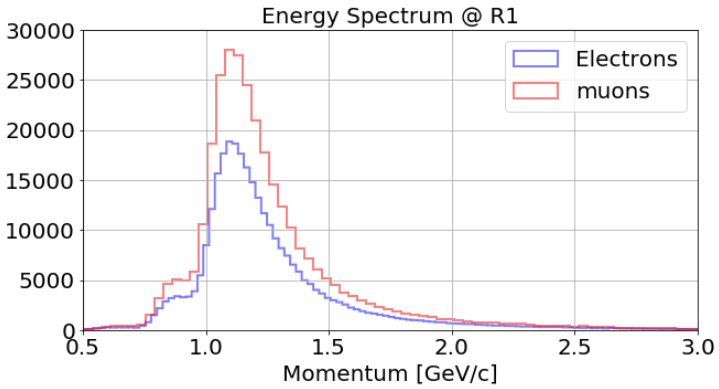

Figure 7.5: Energy deposition from a muon (red) and electron (blue) beam at 15 GeV/c simulated on Geant4. The beam impinges on the center of the prototype.

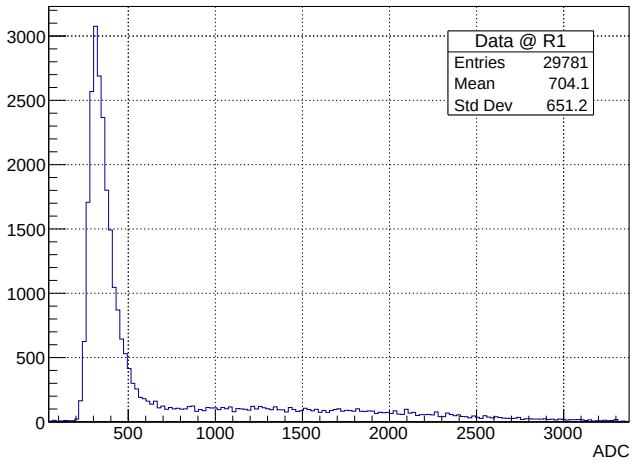

Figure 7.6: Energy deposition data from a run with geometrical cut on the center of the calorimeter.

Taking into account the total thickness of the prototype and the length of radiation, the test performed in T9 was equivalent to a uniform exposure of the detector to mips. It was then not possible to compare the absolute mip response of ENUBINO with the previous generation lateral prototypes, but it showed that the mechanical solutions employed for large-scale production

Figure 7.7: Caption

did not compromise the excellent light yield. This result provided the final validation of the demonstrator, which was completed in September 2022 and tested in T9 in October 2022 as shown in Fig.7.7.

Chapter 8

Conclusions

This thesis aims to study and develop a secondary beamline for the ENUBET experiment that would capture, momentum-select and transfer the hadrons to produce ν_μ and ν_e inside an instrumented tunnel. The reconstruction of the decays of these secondary hadrons, and in particular, the monitoring of charged lepton production in the decay tunnel will provide valuable information on the neutrino cross-section that is plagued today by large systematic uncertainties. This thesis thus addresses a potential limitation of the baseline ENUBET design, i.e. the fact that the neutrino energy spectrum has been tuned to match the region of interest of DUNE and it lacks in flexibility to fully cover the energy region of HyperKamiokande. The main feature of this design is the tunability of the energy of secondaries ("Multi Momentum Beamlinw", MMB). This feature makes it possible to cover - in different runs performed at different pion/kaon momenta - the whole energy range relevant to long-baseline experiments. For this purpose, the designed beamline can transport particles in three different momenta: 4, 6, and 8.5 GeV/c. This range of momenta offers a large neutrino flux and kaon yield with the 400 GeV/c primary protons of the CERN SPS while enhancing the kinematic region accessible to ENUBET.

The newly developed Multi-Momentum Beamline has been the subject of three-year studies and brought to an end-to-end simulation covering target, optics, beam components, and particle transport down to the decay tunnel. The most important findings are summarized as follows:

- **Target:** The target optimization was carried out to maximize the secondary flux in the entire range of the MMB. The optimization was done by investigating several materials and target geometries, and computing the yields. The optimal material in terms of hadronic production is confirmed to be Carbon in the MMB power and momentum range.

The final shape is a cylinder of 20 mm of radius, and 70 mm of length.

The advantage of Carbon is that is a cheap, non-toxic material, that can be readily available. Its properties are well-known and studied, and its thermal properties are quite robust. This finding simplifies the engineering of the target station compared with target materials/parameters considered in high-power facilities.

- **Beamline Design Principles** The main purpose of this project is to be able to monitor the neutrino beam by detecting the leptons emitted by the decays of the secondary mesons impacting the walls of the tunnel. Lepton identification requires a clean beam, where the signal is not contaminated by un-decayed secondary particles impinging on the walls of the tagger. The optics of this beamline were thus aimed at obtaining a purely parallel beam at the entrance of the decay tunnel, still retaining a large acceptance. The design delivered fulfills this condition: the beam envelope is fully contained down to the hadron dump and the secondary fluxes significantly exceed the ones of the baseline design.

- **Beamline components** An important asset of the MMB is the use of CERN beam components. The magnets employed for this design are all pre-existing and currently in use at CERN. This is key to the implementation of ENUBET in a particle physics laboratory: the use of existing large-aperture magnets simplifies the beamline engineering design because the electromagnetic, thermal, and mechanical properties of the components are well-assessed. Since beam components are one of the main cost-driver of a short-baseline neutrino beam like ENUBET, this feature of MMB impacts remarkably the overall cost of the facility.

Employing the design obtained from these studies, a beamline composed of pre-existing magnets is proposed that can provide a variable range of secondary energy to cover the area of interest of both HyperK and DUNE. Assuming a neutrino detector of about 500 tons (the size, for instance, of ProtoDUNE-SP) and employing the CERN-SPS as a driver (400 GeV/c protons) and 4.5×10^{19} PoT/y, this beamline would yield 10^4 ν_eCC in less than 2 years. Furthermore, the 4 GeV momentum run enhances the ν_e flux in a region where the $\sigma_{\nu_e}/\sigma_{\nu_\mu}$ ratio is poorly known. The ENUBET MMB is thus instrumental to the systematic reduction program of HyperK.

The present Ph.D. thesis constitutes the first step in the development of the "Multi-momentum" beam line for ENUBET. More detailed studies need to be carried out in the future to validate this design. The first item to be

addressed concerns detailed radiation protection and energy deposition studies about the effects that a 400 GeV/c beam has on the magnetic elements and the target. When discussing the rate and number of usable neutrinos integrated over time, it is necessary to take into account the effective operational time that the beamline and target can sustain under the beam power, which is important for the proposed implementation at CERN. Aiming for a site-dependent implementation, it is mandatory to analyze what effects the radiation damages have on the surrounding environment: beam components, instrumentation, and the experimental area. These studies, complemented by a full assessment of the physics reach, will ground the proposal for a new short-baseline experiment at CERN and the construction of the first monitored neutrino beam.

Bibliography

[1] Michelangelo Pari et al. "SISSA: Development and optimization of the ENUBET beamline". In: *PoS* (2022), p. 028.

[2] E. G. Parozzi et al. "The ENUBET Multi Momentum Secondary Beamline Design". In: *presented at the 12th Int. Particle Accelerator Conf. (IPAC'21)* (Campinas, Brazil). JACoW Publishing, 2021.

[3] R Acciarri et al. "Long-Baseline Neutrino Facility (LBNF) and Deep Underground Neutrino Experiment (DUNE) Conceptual Design Report Volume 1: The LBNF and DUNE Projects. arXiv 2016". In: *arXiv preprint arXiv:1601.05471* ().

[4] C.L. Cowan et al. "Detection of the free neutrino: a confirmation". In: *Science* 124.3212 (1956), pp. 103–104.

[5] F. Reines and C.L. Cowan. "The neutrino". In: *Nature* 178 (1956), pp. 446–449. DOI: 10.1038/178446a0.

[6] G. Danby et al. "Observation of High-Energy Neutrino Reactions and the Existence of Two Kinds of Neutrinos". In: *Phys. Rev. Lett.* 9 (1962), pp. 36–44. DOI: 10.1103/PhysRevLett.9.36.

[7] S. Bilenky. *Introduction to the physics of massive and mixed neutrinos*. Vol. 947. Springer, 2018.

[8] John N Bahcall. "Solar neutrinos. i. theoretical". In: *Physical Review Letters* 12.11 (1964), p. 300.

[9] Richard D. Ball et al. "Precision determination of electroweak parameters and the strange content of the proton from neutrino deep-inelastic scattering". In: *Nuclear Physics B* 823.1 (2009), pp. 195–233. ISSN: 0550-3213. DOI: https://doi.org/10.1016/j.nuclphysb.2009.08.003. URL: https://www.sciencedirect.com/science/article/pii/S0550321309004052.

[10] J.A. Formaggio and G.P. Zeller. "From eV to EeV: Neutrino cross sections across energy scales". In: *Reviews of Modern Physics* 84.3 (2012), p. 1307.

[11] C. Giunti and Chung W Kim. *Fundamentals of neutrino physics and astrophysics*. Oxford university press, 2007.

[12] Ziro Maki, Masami Nakagawa, and Shoichi Sakata. "Remarks on the Unified Model of Elementary Particles". In: *Progress of Theoretical Physics* 28.5 (1962), pp. 870–880. ISSN: 0033-068X. DOI: 10.1143/PTP.28.870. eprint: https://academic.oup.com/ptp/article-pdf/28/5/870/5258750/28-5-870.pdf. URL: https://doi.org/10.1143/PTP.28.870.

[13] Silvia Adrián-Martinez et al. "Letter of intent for KM3NeT 2.0". In: *Journal of Physics G: Nuclear and Particle Physics* 43.8 (2016), p. 084001.

[14] M. Tanabashi et al. "Review of Particle Physics". In: *Phys. Rev.* D98.3 (2018), p. 030001. DOI: 10.1103/PhysRevD.98.030001.

[15] *NuFIT 4.0*. 2018. URL: http://www.nu-fit.org/.

[16] Ivan Esteban et al. "Global analysis of three-flavour neutrino oscillations: synergies and tensions in the determination of θ 23, δ CP, and the mass ordering". In: *Journal of High Energy Physics* 2019.1 (2019), p. 106.

[17] M. G. Aartsen et al. "PINGU: A Vision for Neutrino and Particle Physics at the South Pole". In: *J. Phys.* G44.5 (2017), p. 054006. DOI: 10.1088/1361-6471/44/5/054006. arXiv: 1607.02671 [hep-ex].

[18] R. L. Workman et al. "Review of Particle Physics". In: *PTEP* 2022 (2022), p. 083C01. DOI: 10.1093/ptep/ptac097.

[19] L Alvarez-Ruso et al. "NuSTEC White Paper: Status and challenges of neutrino–nucleus scattering". In: *Progress in Particle and Nuclear Physics* 100 (2018), pp. 1–68.

[20] Artur M Ankowski and Camillo Mariani. "Systematic uncertainties in long-baseline neutrino-oscillation experiments". In: *Journal of Physics G: Nuclear and Particle Physics* 44.5 (2017), p. 054001.

[21] Teppei Katori and Marco Martini. "Neutrino–nucleus cross sections for oscillation experiments". In: *Journal of Physics G: Nuclear and Particle Physics* 45.1 (2017), p. 013001.

[22] *MINERVA website*. URL: https://minerva.fnal.gov..

[23] *T2K website*. URL: http://t2k-experiment.org/t2k/..

[24] *NOVA website*. URL: https://novaexperiment.fnal.gov/..

[25] *MicroBooNE website*. URL: https://microboone.fnal.gov/..

[26] J Blietschau et al. "Total cross sections for ve and ve interactions and search for neutrino oscillations and decay". In: *Nuclear Physics B* 133.2 (1978), pp. 205–219.

[27] K Abe et al. "Measurement of the inclusive electron neutrino charged current cross section on carbon with the t2k near detector". In: *Physical review letters* 113.24 (2014), p. 241803.

[28] J Wolcott et al. "Measurement of Electron Neutrino Quasielastic and Quasielastic like Scattering on Hydrocarbon at$<$ E $\nu>=$ 3.6 GeV". In: *Physical review letters* 116.8 (2016), p. 081802.

[29] F Acerbi et al. "A high precision neutrino beam for a new generation of short baseline experiments". In: *arXiv preprint arXiv:1901.04768* (2019).

[30] L. A. Ahrens et al. "Comparison of narrow-band and wide-band neutrino beams in the search for $\nu_\mu \to \nu_e$ oscillations". In: *Phys. Rev. D* 36 (3 1987), pp. 702–706. DOI: 10.1103/PhysRevD.36.702. URL: https://link.aps.org/doi/10.1103/PhysRevD.36.702.

[31] P Zucchelli. "A novel concept for a νe/νe neutrino factory: the beta-beam". In: *Physics Letters B* 532.3-4 (2002), pp. 166–172.

[32] A Longhin, L Ludovici, and F Terranova. "A novel technique for the measurement of the electron neutrino cross section". In: *The European Physical Journal C* 75.4 (2015), p. 155.

[33] Andrea Longhin et al. "High precision measurements of neutrino fluxes with ENUBET". In: *PoS* (2017), p. 050.

[34] F Acerbi et al. *The ENUBET project*. Tech. rep. 2018.

[35] M. Pari. "A monitored beam for precise neutrino flux determination: The ENUBET project". In: *Nuovo Cim. C* 41.3 (2018), p. 110. DOI: 10.1393/ncc/i2018-18110-0.

[36] A. Branca. "ENUBET: the first monitored neutrino beam". In: Presented at the ICHEP 2022 Conference in Bologna, Italy, 2022.

[37] J Rossbach and Peter Schmueser. *Basic course on accelerator optics*. Tech. rep. P00011673, 1993.

[38] N. Charitonidis and I. Efthymiopoulos. "Low energy tertiary beam line design for the CERN neutrino platform project". In: *Phys. Rev. Accel. Beams* 20 (11 2017), p. 111001. DOI: 10.1103/PhysRevAccelBeams.20.111001. URL: %5C%5Chttps://link.aps.org/doi/10.1103/PhysRevAccelBeams.20.111001.

[39] N. Simos, M. Bishai, and N.V. Mokhov. "Low-Z High Power Targets for Neutrino Beams: Performance under Intense Proton Flux". In: *Nuclear Physics B - Proceedings Supplements* 229-232 (2012). Neutrino 2010, p. 506. ISSN: 0920-5632. DOI: https://doi.org/10.1016/j.nuclphysbps.2012.09.143. URL: http://www.sciencedirect.com/science/article/pii/S092056321200360X.

[40] N. Simos et al. "200 MeV proton irradiation of the oxide dispersion strengthened copper alloy (GlidCop-Al15)". In: *Journal of Nuclear Materials* 516 (2019), pp. 360–372. ISSN: 0022-3115. DOI: https://doi.org/10.1016/j.jnucmat.2019.01.026. URL: http://www.sciencedirect.com/science/article/pii/S0022311518313357.

[41] M Bonesini et al. "On particle production for high energy neutrino beams". In: *Eur. Phys. J. C* 20.1 (2001), pp. 13–27.

[42] I Chemakin et al. "Pion production by protons on a thin beryllium target at 6.4, 12.3, and 17.5 GeV/c incident proton momenta". In: *Phys. Rev. C* 77.1 (2008), p. 015209.

[43] Nicolas Abgrall et al. "Measurements of $\pi^{\pm}$, $K^{\pm}$, K^0_S , Λ and proton production in proton–carbon interactions at 31 GeV/c with the NA61/SHINE spectrometer at the CERN SPS". In: *Eur. Phys. J. C* 76.2 (2016), p. 84. DOI: 10.1140/epjc/s10052-016-3898-y.

[44] Maria Gabriella Catanesi et al. "Large-angle production of charged pions by 3 GeV/c–12 GeV/c protons on carbon, copper and tin targets". In: *Eur. Phys. J. C* 53.2 (2008), pp. 177–204.

[45] Richard P. Feynman. "Very High-Energy Collisions of Hadrons". In: *Phys. Rev. Lett.* 23 (24 1969), pp. 1415–1417. DOI: 10.1103/PhysRevLett.23.1415.

[46] *JPARC-MR website: http://j-parc.jp/c/en/facilities/accelerators/mr.html*. URL: http://j-parc.jp/c/en/facilities/accelerators/mr.html.

[47] L Bruno and I. Efthymiopoulos. *The CNGS Target Explained*. Tech. rep. OPERA public note n.138, 2011. URL: http://operaweb.lngs.infn.it/Opera/phpmyedit/notes-pub.php.

[48] Lucia Popescu, Donald Houngbo, and Marc Dierckx. "High-power target development for the next-generation ISOL facilities". In: *Nucl. Instrum. Meth. B* 463 (2020), pp. 262–268. ISSN: 0168-583X. DOI: https://doi.org/10.1016/j.nimb.2019.05.023. URL: http://www.sciencedirect.com/science/article/pii/S0168583X19303283.

[49] K. Abe et al. "The T2K experiment". In: *Nucl. Instrum. Meth. A* 659.1 (2011), pp. 106–135. ISSN: 0168-9002. DOI: https://doi.org/10.1016/j.nima.2011.06.067. URL: http://www.sciencedirect.com/science/article/pii/S0168900211011910.

[50] P. Astier et al. "Search for $\nu_\mu \to \nu_e$ oscillations in the NOMAD experiment". In: *Phys. Lett. B* 570 (2003), pp. 19–31. DOI: 10.1016/j.physletb.2003.07.029. arXiv: hep-ex/0306037.

[51] R. Acquafredda et al. "The OPERA experiment in the CERN to Gran Sasso neutrino beam". In: *J. of Instrumentation* 4 (2009), P04018.

[52] P. Adamson et al. "The NuMI neutrino beam". In: *Nucl. Instrum. Meth. A* 806 (2016), pp. 279–306. ISSN: 0168-9002. DOI: https://doi.org/10.1016/j.nima.2015.08.063. URL: http://www.sciencedirect.com/science/article/pii/S016890021501027X.

[53] A. A. Aguilar-Arevalo et al. "Neutrino flux prediction at MiniBooNE". In: *Phys. Rev. D* 79 (7 2009), p. 072002. DOI: 10.1103/PhysRevD.79.072002. URL: https://link.aps.org/doi/10.1103/PhysRevD.79.072002.

[54] E. Baussan et al. "A very intense neutrino super beam experiment for leptonic CP violation discovery based on the European spallation source linac". In: *Nuclear Physics B* 885 (2014), pp. 127–149. ISSN: 0550-3213. DOI: https://doi.org/10.1016/j.nuclphysb.2014.05.016. URL: http://www.sciencedirect.com/science/article/pii/S0550321314001588.

[55] Maja Olvegård et al. "Overview of the ESSnuSB accumulator ring". In: *57th ICFA Advanced Beam Dynamics Workshop on High-Intensity and High-Brightness Hadron Beams*. 2016, MOPR021. DOI: 10.18429/JACoW-HB2016-MOPR021.

[56] Tadashi Koseki et al. "Beam commissioning and operation of the J-PARC main ring synchrotron". In: *Progress of Theoretical and Experimental Physics* 2012.1 (2012). 02B004. ISSN: 2050-3911. DOI: 10.1093/ptep/pts071.

[57] B Goddard et al. *The New SPS Extraction Channel for LHC and CNGS*. Tech. rep. CERN-SL-2000-036-BT. 2000, p. 4. URL: https://cds.cern.ch/record/448333.

[58] V. Kain et al. "High intensity commissioning of SPS LSS4 extraction for CNGS". In: *2007 IEEE Particle Accelerator Conference (PAC)*. 2007, pp. 1604–1606. DOI: 10.1109/PAC.2007.4440837.

[59] E. Gschwendtner. "CERN Neutrinos to Gran Sasso (CNGS): First Beam". In: *2006 IEEE Nuclear Science Symposium Conference Record*. Vol. 3. 2006, pp. 1489–1492. DOI: 10.1109/NSSMIC.2006.354181.

[60] A. Booth et al. "Commissioning Results of the Tertiary Beam Lines for the CERN Neutrino Platform Project". In: *Journal of Physics: Conference Series* 1350 (2019), p. 012094. DOI: 10.1088/1742-6596/1350/1/012094. URL: https://doi.org/10.1088%5C%2F1742-6596%5C%2F1350%5C%2F1%5C%2F012094.

[61] B. Abi et al. *The Single-Phase ProtoDUNE Technical Design Report*. Tech. rep. FERMILAB-DESIGN-2017-02. 2017. URL: http://cds.cern.ch/record/2271524.

[62] B. Abi et al. "First results on ProtoDUNE-SP liquid argon time projection chamber performance from a beam test at the CERN Neutrino Platform". In: *J. of Instrumentation* 15.12 (2020), P12004–P12004. DOI: 10.1088/1748-0221/15/12/p12004. URL: https://doi.org/10.1088/1748-0221/15/12/p12004.

[63] Michelangelo Pari. "Study and development of SPS slow extraction schemes and focusing of secondary particles for the ENUBET monitored neutrino beam". PhD thesis. Universitá degli Studi Di Padova, Dipartimento di Fisica e Astronomia G ..., 2021.

[64] Giuseppe Battistoni et al. "Overview of the FLUKA code". In: *Annals of Nuclear Energy* 82 (2015), pp. 10–18.

[65] TT Böhlen et al. "The FLUKA code: developments and challenges for high energy and medical applications". In: *Nuclear data sheets* 120 (2014), pp. 211–214.

[66] Thomas J Roberts et al. "G4Beamline particle tracking in matter dominated beam lines". In: *Proc. PAC*. Vol. 2013. 2011, pp. 373–375.

[67] Richard P. Feynman. "Very High-Energy Collisions of Hadrons". In: *Phys. Rev. Lett.* 23 (24 1969), pp. 1415–1417. DOI: 10.1103/PhysRevLett.23.1415. URL: https://link.aps.org/doi/10.1103/PhysRevLett.23.1415.

[68] GEANT Collaboration, S Agostinelli, et al. "GEANT4–a simulation toolkit". In: *Nucl. Instrum. Meth. A* 506.25 (2003).

[69] A Ferrari et al. *FLUKA: A multi-particle transport code*. CERN Yellow Reports: Monographs. Geneva: CERN, 2005. DOI: 10.5170/CERN-2005-010. URL: http://cds.cern.ch/record/898301.

[70] L Gatignon. *Magnets Kit for the Experimental Areas of the CERN PS/SPS complex*. Tech. rep. Geneva: CERN, 1991. URL: https://cds.cern.ch/record/711814.

[71] Division MPS et SI. *Specification for MPS standard quadrupole magnets*. Tech. rep. Geneva: CERN, 1970. URL: http://cds.cern.ch/record/2304683.

[72] Nikolaos Charitonidis et al. "Design and Diagnostics of High-Precision Accelerator Neutrino Beams". In: *Applied Sciences* 11.4 (2021). ISSN: 2076-3417. DOI: 10.3390/app11041644. URL: https://www.mdpi.com/2076-3417/11/4/1644.

[73] M. Gasior et al. "Introduction to Beam Instrumentation and Diagnostics". In: *CERN Accelerator School: Advanced Accelerator Physics Course*. 2014, pp. 23–60. DOI: 10.5170/CERN-2014-009.23. arXiv: 1601.04907 [physics.acc-ph].

[74] AC Booth et al. "Particle production, transport, and identification in the regime of 1- 7 GeV/c". In: *Physical Review Accelerators and Beams* 22.6 (2019), p. 061003.

[75] G. Aglieri Rinella et al. "The NA62 GigaTracKer: a low mass high intensity beam 4D tracker with 65 ps time resolution on tracks". In: *Journal of Instrumentation* 14.07 (2019), P07010–P07010. DOI: 10.1088/1748-0221/14/07/p07010. URL: https://doi.org/10.10882F1748-0221%2F14%2F07%2Fp07010.

[76] Collaboration NA62. *2020 NA62 Status Report to the CERN SPSC*. Tech. rep. 2020.

[77] F. Acerbi et al. "The ENUBET positron tagger prototype: construction and testbeam performance". In: *J. of Instrumentation* 15.08 (2020), P08001. DOI: 10.1088/1748-0221/15/08/P08001. arXiv: 2006.07269 [physics.ins-det].